Identifying Spatio-temporal Dynamics in Interacting Brain Networks

by

Daniel Muenzer Maruyama

A dissertation submitted in partial fulfillment
of the requirements for the degree of
Doctor of Philosophy
(Physics)
in The University of Michigan
2015

Doctoral Committee:

Professor Michal R. Zochowski, Chair
Assistant Professor Sara J. Aton
Associate Professor Victoria Booth
Emeritus Professor Leonard M. Sander
Professor Robert S. Savit

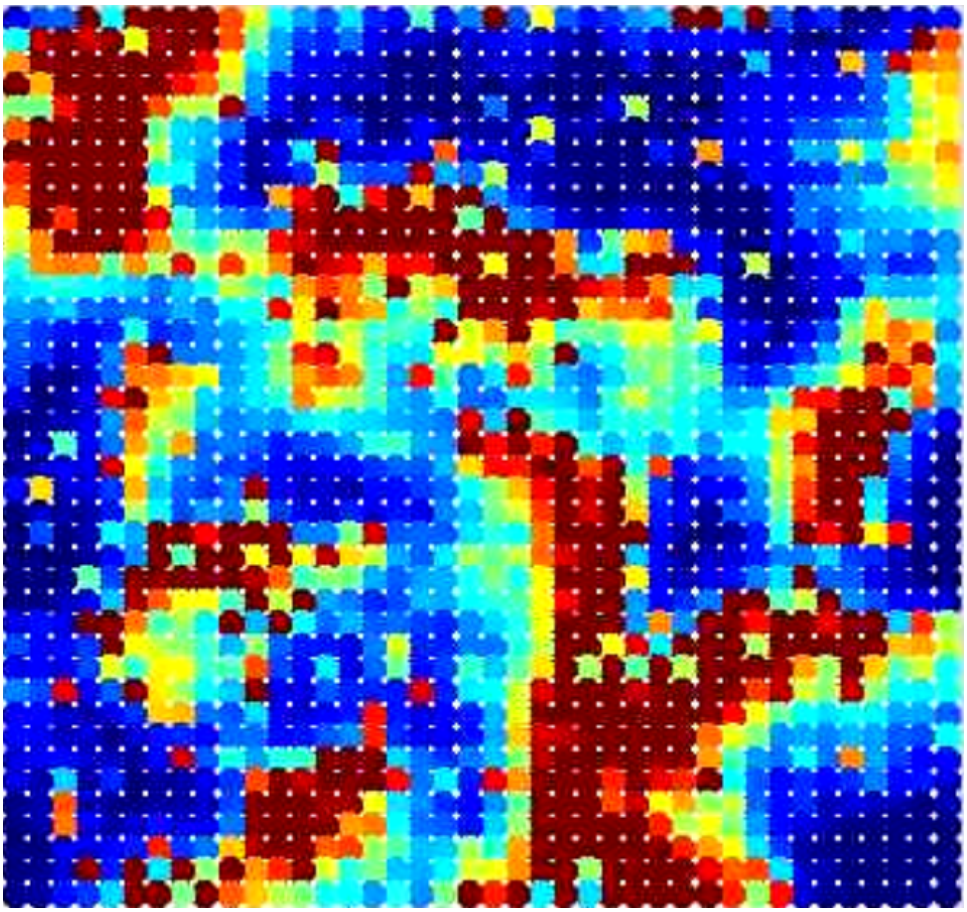

For everyone who supported me in this journey. Thank you.

ACKNOWLEDGEMENTS

My time spent in grad school (six years!) is something I will always remember fondly. Almost every day, as my lab mates can attest, I woke up with a feeling of joy that I was given the opportunity to delve deep into my thoughts and tackle questions that interest me deeply. I consider myself incredibly fortunate to have been able fully devote my time and efforts to grad school and occasionally to golf as well. I'm proud of my time spent within the ivory tower, and I say that with an understanding of the disparaging connotation aimed at isolated academics. I believe that only by taking time to slowly pick apart complex topics have I been able to push myself to comprehend new ideas. The most general concept that I have come to appreciate in grad school has been a much wider understanding about the process of science. The process whereby good ideas are often proven to work poorly and need to be slowly crafted into better ones. Grad school is not perfect, the realities and politics of the academic life are not fully broadcast to young undergrads eagerly applying to grad school, but I loved the time I spent working on my dissertation and would joyfully repeat the process.

I have many people to thank for aiding me in my journey to and through graduate school, but none more so than my family. Before I even completed kindergarten I had the idea set in my head that I wanted to get a Ph.D. some day and my family made sure to make that path available to me. I don't thank any of you nearly enough so let me say it clearly here, thank you. Thank you for supporting and encouraging me and thank you for everything you have done for me which I don't know about as well.

Mom and Dad, you guys did a great job of promoting a learning environment for me as a child. Whether it was encouraging me to tackle math and science questions, buying me all those ridiculous animal figures and fact sheets, reading the latest science news with me, or helping me probe concepts at a deeper level, all of these things have helped me in trying to tackle the endless stream of questions on how and why things work. Kristie, you also helped foster my scientific curiosity by reading to me, performing chemistry experiments with me in the basement, helping me with my summer homework, and of course leading me to neuroscience at the University of Michigan. Andrew, you always been happy to listen to me and I've never felt like I've been speaking you in a foreign language while discussing my work. Little George, you have only been around for 364 days at this point, but you've been pretty wonderful as well.

Of course I need to thank my research advisor Michal Zochowski. You have easily been the biggest influence on my development as a scientist. Thank you for taking the time to show me how to craft scientific papers out of rough ideas. Thank you for showing me how to ask good questions. Thank you for working around my sometimes unorthodox work hours. Lastly, thank you for being a kind advisor.

In my time at Michigan, my lab mates spent the most time with me. I owe a great deal to Liz Shtrahman, Chris Fink, Sima Mofakham, James Roach, Quinton Skilling, David Adams, Tony Smith and Sarah Feldt for guiding me, discussing science, and sharing ideas with me. In particular, I always loved: talking with Liz about grad school and her life woes, spending far too much time talking about Michigan sports with Chris, hearing new and engaging perspectives from Sima, and listening to honest, well thought out arguments from James. I also want to thank two of my collaborators who I spent a lot of time with, Nicolette Ognjanovski and Sara Aton. Working closely with you two has been a wonderful opportunity for me, and I really appreciate the way both of you approach science. Sara, the way you engage others in discussions

about your work is something I hope to learn eventually.

Lastly, I have to thank my friends who put up with me when I wasn't doing science. Peter D'Angelo, Alyssa Keimach, Ozzie Ozeewee Irwin, Merrybelle Guo, and Ibrahim Boulares all helped me get the most out of my time in Ann Arbor. They have all seen me at my worst and best, and I owe them thanks for sticking around. If it's true that you're only as good as the company you keep, then I'm doing pretty darn well.

TABLE OF CONTENTS

LIST OF FIGURES

Figure

LIST OF ABBREVIATIONS

ATP Adenosine Triphosphate

AMD Average Minimum Distance

BTW Bak-Tang-Wiesenfield

CA1 Cornu Ammonis area 1

CFC Contextual Fear Conditioning

DIV Days *In Vitro*

FCA Functional Clustering Algorithm

ER Endoplasmic Reticulum

IP3 Inositol Triphosphate

ISI Interspike Interval

MEA Multi-electrode Array

MPC Mean Phase Coherence

SWS Slow Wave Sleep

REM Rapid Eye Movement Sleep

RMSD Root Mean Square Difference

ABSTRACT

Identifying Spatio-temporal Dynamics in Interacting Brain Networks

by

Daniel Maruyama

Chair: Michal Zochowski

Complex activity patterns in the brain arise from underlying interactions between neurons and astrocytes in the brain. Recent data acquisition has made it possible to measure the activity from many cells at one time. Extracting information from these data sources requires systems analysis techniques capable of describing network dynamics. Here I examine two broad approaches to understand interactions in brain networks.

Astrocyte have recently been implicated in modulating neuron networks, but astrocyte signaling remains largely unknown. Astrocyte dynamics are examined by investigating the impact of distinct signaling pathways. We find that the interplay between the pathways is highly dependent upon the network topology, with cooperation being promoted by local networks and competition observed in random networks. Local networks are good approximations of biological astrocytes and are capable of reproducing the firing rate, shape, and spatial distribution of astrocyte network transients. This helps us to understand the way these networks develop and how they can be manipulated.

The second way we look at activity patterns is by addressing some challenges provided by high dimensional data. Starting from modern data sets, specifically time series data, we identify functional relationships in neurons by quantifying consistent firing behaviors. We find that using just the spike times of neurons we can create a reliable functional connectivity measure without the need to invoke slow Monte Carlo sampling methods. We also look to measure changes in functional relationships which are believed to store memories within brain networks. Here we find that changes in functional network structure reflect learned behavior in mice.

CHAPTER I

Introduction

As the source of thought, emotion, and creativity the brain has been the focus of intense study. Given its central role in our lives and how impressively it performs, many fields of thought have tried to understand inner workings of the brain. These include researchers and academics from fields including philosophy, psychology, cognitive science, biology, chemistry, physics, mathematics, electrical engineering, computer science, and statistics. Surprisingly and somewhat amusingly, in light of the numerous attempts to undress it, the neural code remains largely unknown.

In the pursuit to decode the workings of the brain, no significant discovery has proven to be the neuroscience equivalent of the Rosetta stone. However, the steady flow of science has been making consistent progress to unravel the mysteries of the brain. Over the last 150 years the shape of neuroscience research has solidified several cornerstones in neural theory, which now guide much of the work. Neuroscience in its modern form, specifically studying the role of these neuron components, is often claimed to have originated from the work of Ramón y Cajal, whose work on understanding humans brains led him to study the anatomy of neurons[1]. The neuron doctrine stemming from this work identifies neurons as the fundamental unit of the brain[2]. Paul Broca's work on damaged brains tied the impairment of macroscopic bodily function to problems within local areas of the brain, suggesting the compart-

mentalization of neural function within the brain[3]. Broca's work and the neuron doctrine are at the core of most ideas relating higher level function to the working of individual neurons.

The exact way in which function arises from neurons has been the focus of many scientists over the last 75 years. Here, work began by understanding the dynamics regulating individual neurons. The seminal work of Hodgkin and Huxley laid out a biologically accurate model of a neuron[4]. The Hodgkin-Huxley model is able to reproduce the activity of most types of neurons within the brain. Unfortunately, since neurons themselves do not individually define higher level function, a second step is necessary in order to make sense of neural function: understanding the interactions between neurons. Specifically, researchers want to understand how neurons work together to break down large tasks in order to process and store information.

It is here that the idyllic narrative of neuroscience erodes, at least for the time being, as the goals in neuroscience are much clearer than the paths to get there. The interactions between individual neurons can be understood to an extent, but not nearly well enough to extrapolate to the scope of the full brain[5]. A problem of scale quickly develops when one tries to start stacking the interactions between neurons in order to build up a larger picture. Synapses, the connections between neurons, are densely packed in the brain, $\sim 10^{11}$ neurons each with 10^3 connections, making it difficult to separate individual pathways within the brain. While it is known that neurons communicate through synapses[6], this vast connected structure makes tracking interactions from synapse to synapse experimentally challenging and conceptually ambiguous. In tracing individual signals through many layers of synapses, it quickly becomes unclear what represents the original signal and what represents some highly convolved component. Legitimate concerns can be raised about whether or not it makes sense to track a specific signal through such a densely interacting environment.

Closely related to the problem of scale is the problem of structure[7]. How does the structure of neurons within the brain promote interactions the brain uses to function? This phrasing is pretty generic, and this question might be easier to understand with an example: What does the robustness of signal propagation in the brain tell us about the way neurons are wired together? The brain is a highly structured organ, as modern microscopy or fMRI images show, and in order to clarify the inner workings of the brain, progress needs to be made to understand the role of that structure in signal propagation, storage, and learning.

The scale and structure of neuron interactions are serious questions in neuroscience that eventually have to be answered in order to understand the brain. Luckily, they do not represent non-starters in research, merely difficulties to overcome. In fact, the size of the brain signifies a good deal about how it works[8]. The vast number of connections suggests that while individual neurons are important, the connections between them are even more essential[9;10]. Additionally, the individual units experience a small amount of turnover, dying at a rate of ~ 10000 per day[11]. This implies that higher level function needs to be robust to small changes in neuronal connections as they are often changing. While tackling the whole question of how the brain distributes processes to utilizing all units is currently unfeasible, some approaches are showing promise.

In terms of the structure, several approaches have also been suggested to directly address the question of structure in the brain. Vernon Mountcastle has two important contributions regarding structure. He was the first researcher to discover columns within the cortex, thereby identifying a functional subunit of larger scale than the neuron[12]. His more prominent contribution was the suggestion of a common neural algorithm in the brain[13]. This is notable as it suggests that specialization is not required for distinct regions within the brain. This fits nicely with a prevailing theory within the field which suggests that the brain processes information by rapidly

filtering signals through its subunits, neurons[14;15]. The key concept being that the brain doesn't selectively drive individual neural circuits, but instead information is filtered through large regions with information being processed over a more distributed region[16].

Interestingly, the one of the most promising current lines of work regarding structure utilizes methods of statistical physics. Restricted Boltzman machines[17;18], an Ising model with a partition function describing the energy of interactions, can be layered to create deep belief networks[19;20]. These stacked layers of networks then attempt to represent the distributed processing power of the brain by letting information filter across the nodes. At the time of writing this, state of the art image and voice recognition, search, and compression systems all draw heavily upon this type of deep neural network architecture[21;22;23].

Building upon the foundation of the neuron doctrine, the modern research approach continues to tackle the question of neural interactions. Advances in computing have greatly aided experimental and computational work by opening up new frontiers to probing. Computing power and analysis of neuron data are ubiquitous to the point that nearly all computational approaches require a computer. Nowhere is this advance so clearly visible as in computational research, where modern simulations scale directly with computer power. The ways in which researchers choose to apply this power varies greatly, with some looking for highly exact models of a single cell and others looking to model the entire brain with simple neuron models. Yet even here these approaches are tied together by the neuron doctrine, with each using a single neuron as the basic unit of the brain.

1.1 A single neuron

Given the prominence of a single neuron to neuroscience and the range of questions be addressed by researchers there are a large number of neuron and spiking models

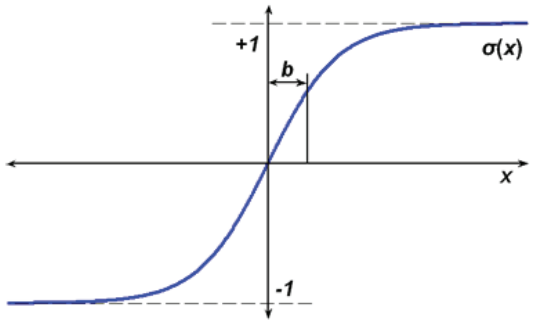

Figure 1.1: Sigmoid activation units - Neurons can be thought of as units with sigmoid activation probabilities. x is the input received by the neuron, b denotes the activation offset, and y is the probability of firing.

used to simulate neuronal activity. No model is fundamentally better than another, what matters most is fit and applicability to the question at hand. All models reflect a neuron's binary nature where given its current state a neuron takes its given input, in the form of noise, external drive, or interactions with other neurons, and using some means of measuring that input either spikes or stays silent. Figure 1.1 shows a generic form of this process, where the input over a time interval is represented on the x-axis, and the probability of spiking is depicted on the y-axis. The more excitatory input a unit receives, the more likely it is to spike in response to the input.

Depending on the degree of accuracy in the model, upon spiking a neuron can experience an action potential or simply send out information to other cells. Biologically realistic models will have action potentials in which the voltage inside the cell rapidly increases for a short burst before falling back to baseline (see Fig. 1.2). Physically, action potentials reflect the transmission of binary information from the soma down to the axon terminal. When an action potential reaches the end of an axon it spurs the release of neurotransmitters across the synaptic cleft to the post-synaptic neuron. The effect of a spike on post-synaptic neurons is dependent upon the type and efficacy of the synapse, and can be altered over time. Synaptic plasticity, the strengthening or weakening of synapses over time, allows for neurons to adjust to the

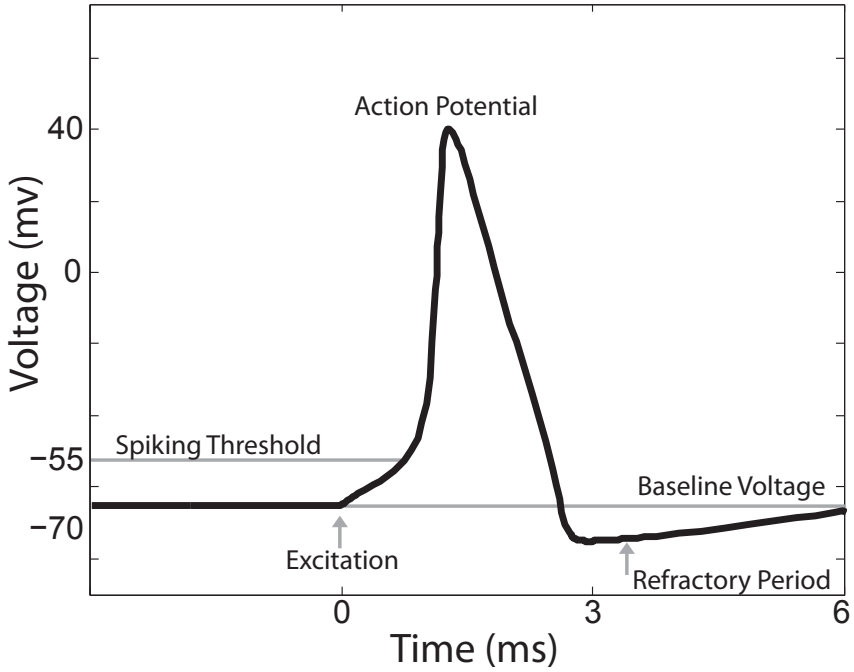

Figure 1.2: Action potential of a Hodgkin-Huxley neuron

behavior of the other neurons they interact with through synapses.

Simplified models may skip the action potential step, but retain the extracellular signaling component of spikes.

1.1.1 Hodgkin-Huxley model

In 1952, Hodgkin and Huxley unveiled a biological neuron model which accurately reproduced transmembrane ion concentrations of spiking neurons. Careful study of squid axons resulted in a model that combined transmembrane diffusion, ion-pumps, and voltage gated channels. The Hodgkin-Huxley model physically represents the voltage at the axon hillock, which is where action potentials originate.

$$C_m \frac{dV_m}{dt} = g_l(V_m - V_l) + g_{Na}(V_{Na} - V_m) + g_K(V_K - V_m) + I_{ext}(t) \qquad (1.1)$$

The left hand side represents the overall transmembrane current change in the

modeled region, with C_m and V_m denoting the membrane capacitance and voltage. The first term on the right hand side is called the leak current and denotes the passive diffusion of ions through the lipid bilayer. g_l and V_l respectively capture the conductance of the leak current and the leak current reversal potential. The term $(V_m - V_l)$ shows the cell's tendency to oscillate around the leak current reversal potential. The next two terms represent specific potassium and calcium ionic currents. Unlike the leak current, in which g_l is constant, the sodium and potassium channel conductances, g_{Na} and g_k, vary with the membrane voltage. During an action potential the sodium channel, g_{Na}, will be the first to open, allowing sodium to enter the cell and causing the cell to depolarize. During this depolarization the potassium channel will open allowing the internal potassium ions to leave hyperpolarizing the cell. Around this same time, the sodium channels close, allowing the internal sodium gradient to begin restoring. Finally, once the neurons internal voltage has dropped back towards baseline the potassium channels close, completing the action potential. After an action potential, neurons enter a refractory period where they are highly unlikely to spike. As mentioned above, Fig. 1.2 shows a resulting action potential after the voltage exceeds a spiking a threshold.

1.1.2 Leaky integrate-and-fire model

In many cases precise modeling of action potentials are unnecessary as the behavior can be summarized with a refractory period and intercellular signaling. One simple model often used to represent neurons is the leaky integrate-and-fire[24] (LIF) neuron model. Here the goal is to reproduce the summation of inputs to the cell and track when a charging threshold, $V = 1$, has been exceeded.

$$C_m \frac{dV_m}{dt} = -\alpha V_m + I_{ext}(t) + \sum_j A_{ij}\, I_{syn,j}(t) \tag{1.2}$$

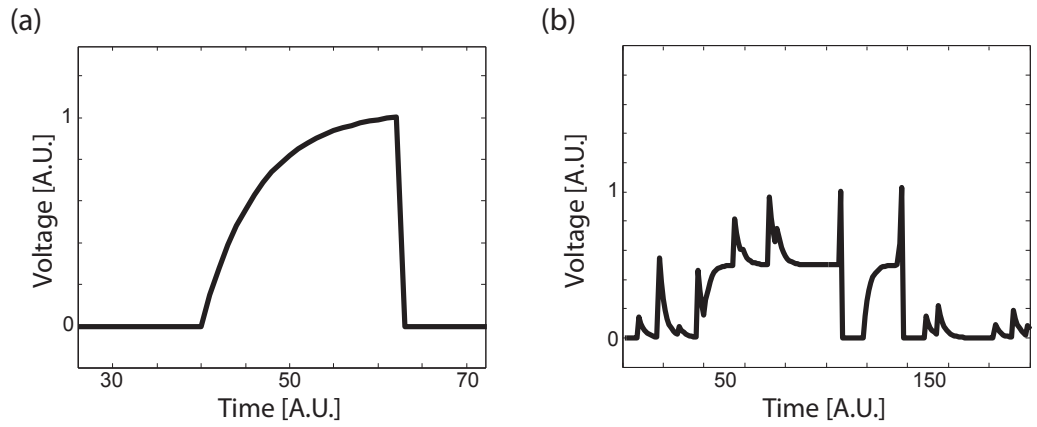

Figure 1.3: Leaky integrate-and-fire neuron dynamics - (a) Shows a LIF neuron charging under constant input. (b) Depicts a LIF neuron with stochastic noise receiving constant drive from time 50-150.

The left hand side denotes the current that crosses the membrane. The right hand side has a leak term, and external current term, and an interaction term reflecting inputs from other neurons. The last term on the right hand side accounts for the efficacy of connections from neuron j to neuron i, A_{ij}, as well as the synaptic current from neuron j, $I_{syn,j}(t)$ following neuron j spike. The name integrate-and-fire is clearly demonstrated by an uncoupled LIF neuron with constant drive, see Fig. 1.2(a). As dictated by the equation governing the neuron's voltage, a LIF neuron integrates input effectively charging up the subthreshold voltage. Upon firing, a refractory period is enforced before the voltage is allowed to vary. In the presence of external noise, variations in voltage exponentially decay back towards the resting potential.

1.2 Networks of neurons

After selecting a desired neuron model, the next step in simulations typically involves connecting neuron units to create a network of interacting units. As mentioned earlier, even relatively small numbers of interacting neurons are difficult to completely describe. This is due in part to the nonlinear activations of neurons and the density of synaptic connections. While complete characterization is difficult, many features

of interacting networks can be studied, and a lot of effort is currently being devoted to this endeavor. Individual neurons are limited in their expression, so some of the most interesting properties of neurons result from non-trivial interactions between neurons[25;26;27]. This emergence is not unique to neurons, but it strongly emphasizes that individual neurons alone are incapable of encapsulating certain features of the brain.

1.2.1 Network interactions

Neurons are undoubtedly the functional subunit of the brain, but ultimately interactions between these neurons may prove to be the source of the brain's power[28;29]]. Individual neurons are binary in nature and exhibit stereotypic firing behavior. The lack of customizability in an individual's firing response makes neurons ill suited to store information. Synapses, on the other hand, are rich in variability[30], more numerous than neurons, and ultimately control the interactions between neurons[31]. Neurons carry a consistent binary signal, but synapses control where and how strongly to send that signal.

Two classes of synaptic signals are present in the brain. Excitatory postsynaptic potentials (EPSPs) indicate that the synapse transmits excitatory information slightly depolarizing the post synaptic neuron. Inhibitory postsynaptic potentials (IPSPs) transmit inhibitory information. Signal propagation within neuron networks can be built up by combining multiple EPSPs and IPSPs, with the downstream neurons reacting to the net input of the upstream signals[32;33]. Figure 1.4 denotes a modern view of neuronal networks where highly dense connections filter signals through layers of neurons. The highly convolved output has been processed by the network to extract features and perform various neural functions.

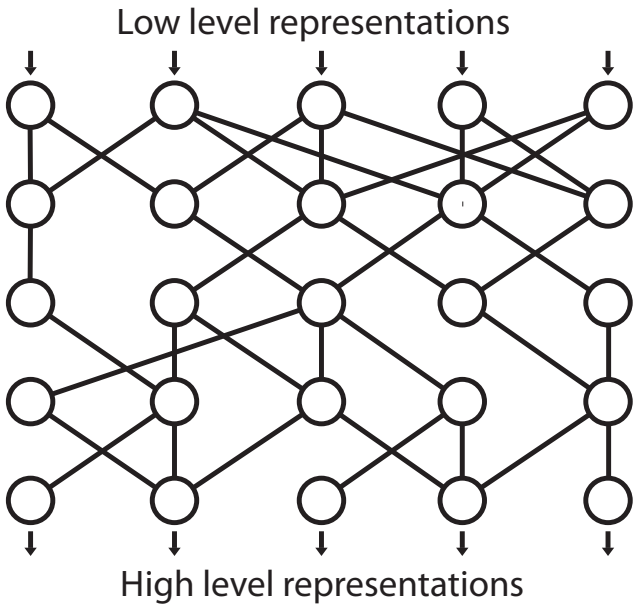

Figure 1.4: Layered view of neuronal computation - Neuron networks filter information through layers, recognizing lower dimensional structures in shallow layers and high dimensional structure in deeper layers.

1.2.2 Emergent dynamics

The patterns of activity in neuron networks represent a fundamental property of networks which is not present in individual neurons. Emergence is very common in biology where structures built out of smaller units are highly ordered and expresses a property incapable of being expressed within the subunits. Figure 1.5 shows two examples of emergence picked up on a stroll through the University of Michigan arboretum. The intricate patterning in each image is not present when looking at the microscopic components, but only becomes clear when expressed on the fully sized objects. In regards to the brain, patterns of activity and processing only become available once many neurons are hooked together.

1.2.3 Synchronization

One type of pattern that emerges in interacting brain networks is synchronization in spiking behavior. Synchronization refers to coherent activity patterns within

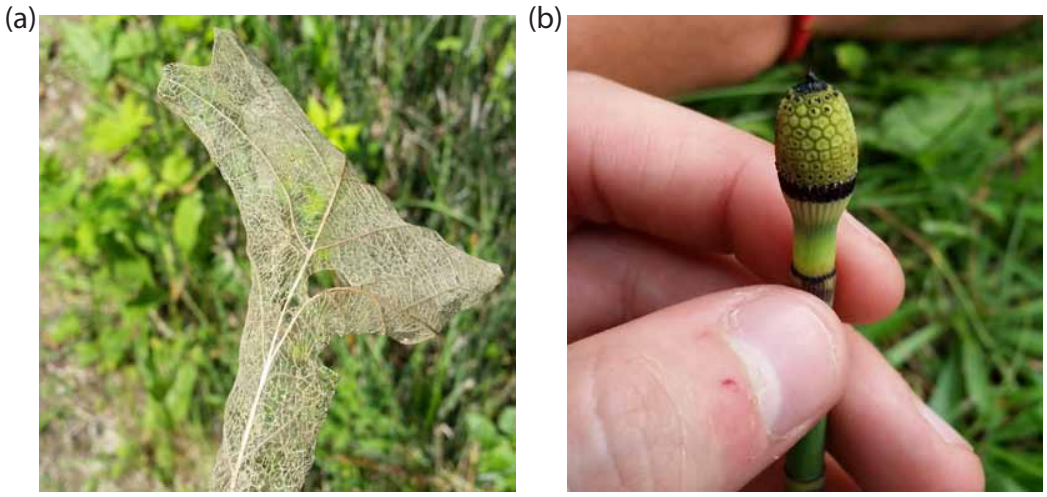

Figure 1.5: Emergence - Two everyday object exhibiting emergence of complex structures.

the brain. A wide range of spiking behaviors can be synchronized, with different properties being consistent across multiple neurons. The patterns of synchronization are highly dependent on the underlying anatomical connectivity of a network[34]. For instance, a one-dimensional ring of neurons can only express linear activity patterns; where as a two-dimensional network can exhibit spiral-like activity, which is not possible on a one-dimensional network.

One of the simplest types of synchronization is coincident firings, in which multiple neurons repeatedly spike around the same time. Temporal synchronization in neuronal networks can be demonstrated well by altering network topology. Take a two-dimensional network of neurons containing only local connections, and alter it by randomly rewiring each connection with a specified probability of rewiring. As the rewiring probability increases, network interactions transition from being locally dominated to being globally dominated. Figure 1.6 shows several types of activity patterns that arise from varying the network topology. Panel (a) shows concentric rings of synchronized activity which result from having no long range connections[35]. Panel (b) shows the highly disordered state where long and short range connections

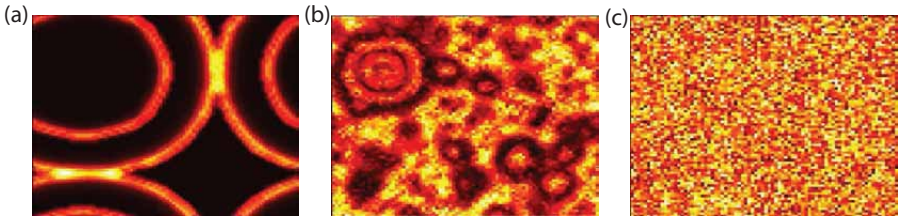

Figure 1.6: Topology dependent synchronization - Synchronization of neuron activity is highly dependent upon network structure. (a) Local networks display clear wave fronts of activity. (b) Mixed short-long range networks exhibit both local coherence and global synchrony. (c) Random networks show synchronous global activity.

are present[36]. Panel (c) shows an instance of a network with all random connections, which results in synchronized bursts of network activity. In transitioning from local to random, the synchronized activity in the network goes from rings surrounding the activation site to full network instances. This progression of order local firings to more chaotic activity to full network behavior is a standard synchronization property of network topology for excitatory neuronal networks.

Phase locking is another type of synchronization that appears in neurons. Instead of coincident firings, neurons synchronize to spike at a consistent phase lag.

1.3 Astrocytes

Understanding interactions between neurons is useful for deciphering dynamics within the brain; however, neurons are not the only cells in the brain. Glial cells are as common as neurons in the brain[37] and are thought to play a role in neuron maintenance. For a long time glial cells were thought to support and nourish neurons, but within the last few decades scientists have come to realize the astrocytes, a type glial cell, are capable of interacting with neurons[38;39;40].

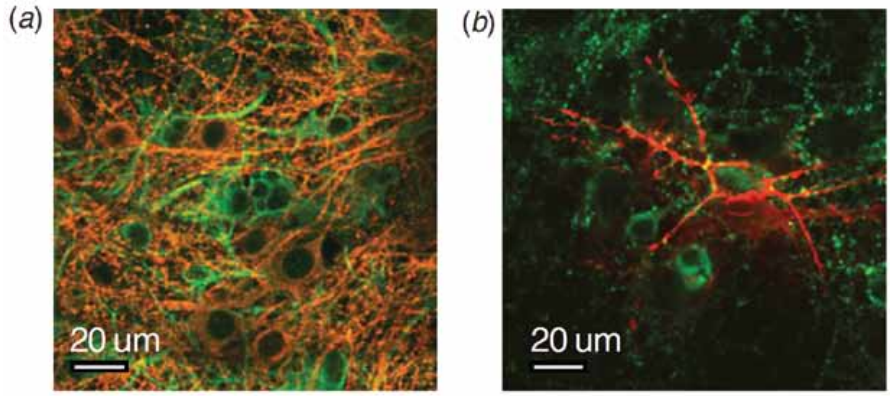

Figure 1.7: Examples of joint neuron-astrocyte networks - Neurons are stained red, while astrocytes are stained green. Images from *Feldt 2010* [41].

1.3.1 The tripartite synapse

Now astrocytes are thought to be an important part of synapses in the brain. Synapses with a nearby astrocyte are called tripartite synapses [42;43]. Tripartite synapses interact with neurons in a few ways [44]. First, neurotransmitters in the synaptic cleft can bond to receptors on the astrocyte eliciting a slow calcium response in the astrocyte [45]. Astrocytes also can release adenosine triphosphate (ATP) which can have excitatory or inhibitory influences on surrounding neurons depending on the metabolic path [46;47]. Lastly, Astrocytes are believed to synthesize and release gliotransmitters allowing them to mediate pre and post synaptic neurons [48;49]. Figure 1.8 depicts the signaling pathways of a tripartite synapse.

Astrocyte activity occurs on a vastly slower time scale than neuronal activity. The difference in speeds contributes to the relationship between the two types of cells. The slow speed of astrocyte transients($\sim$10s) means that they are not an essential aspect of fast brain computations. However, their speed of response does not rule out a modulatory effect on neurons. One such theory suggests that astrocytes respond to neuronal fatigue and help promote sleep [50]. In general, for interactions on different time scales, the slower time scale modulates the activity of the faster interaction.

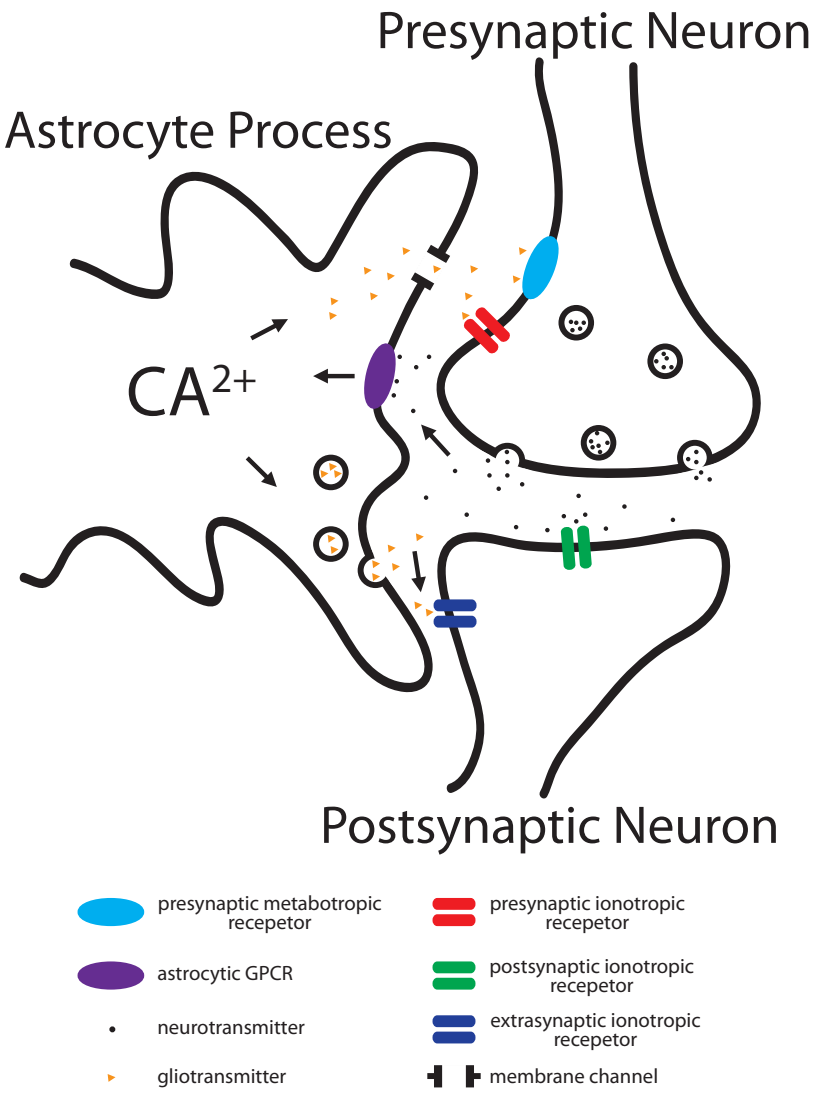

Figure 1.8: A drawing of a tripartite synapse - Neurotransmitters from the presynaptic neuron can influence activity in the postsynaptic neuron and nearby astrocytes. Likewise, gliotransmitters released after bouts of astrocyte activity can stimulate the pre and postsynaptic neurons. Image adapted from *Agulhon 2008* [45]

That could be the case here, unfortunately not much is known about the dynamics of astrocyte networks.

1.3.2 Astrocyte networks

Before studying how networks of astrocytes interact with networks of neurons, research on the interactions within astrocytes is needed. Unlike neurons, which interact primarily through synapses, astrocytes interact through two distinct pathways[51]. The glial equivalent to synapses is gap junctions, which are direct connections between astrocytes allowing diffusion of IP_3 ions. IP_3 is a signaling molecule, which after entering the endoplasmic reticulum causes the release of calcium ions. The other common interaction pathway is extracellular diffusion[52]. ATP is one of the components, but many others are secreted from the cytoplasm of the cell to the extracellular fluid. Concentrations decay rapidly in three-dimensional diffusion, making the secreted pathway short range in extent. Gap junctions allow for interaction between any touching astrocyte processes. Astrocytes are typically more local than neurons, but long range processes sometimes occur. Patterns in astrocyte networks are defined by the distinct signaling pathways, which interact on different characteristic length scales.

1.4 Measurements of network structure and evolution

Visually observing pair wise interactions in many neuron networks is an exercise in futility[53]. Measuring the neural interactions is required in order to help reduce the dimensionality of many neuron networks. Unfortunately, measurements in brain data present several unique challenges. Synapses themselves are currently impossible to measure directly, meaning the clearest signal that can be recorded is action potentials in neurons. Network level neuron data is difficult to come by, and what is available has been reduced to time stamps of firing of neurons. Correlations can be reconstructed

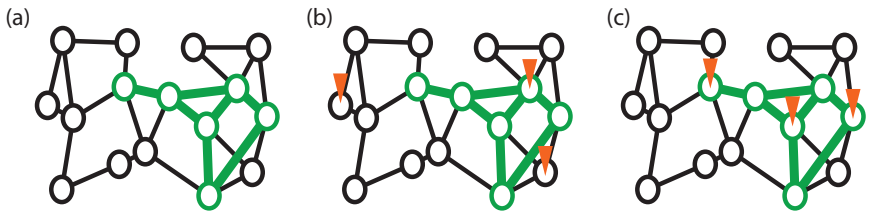

Figure 1.9: Measuring network heterogeneities - (a) Shows a network of interconnected neurons, with strengthened green connections identifying members of a structural heterogeneity. Depending on where measurements, orange triangles, are made, the identified structure will be quite different. (b) Does not detect any increased connections, and (c) measures strong connections everywhere.

from neuron firing times[54], but this ignores the state of each neuron for the majority of the recordings.

Many modern data acquisition setups provide data from random locations within a sample. This is problematic because it limits what can be said about the data. Imagine a collection of cell, Fig. 1.9(a), where a portion of them are bound together with strengthened connections, called a heterogeneity. Suppose this heterogeneity represents the color blue, so that when a person sees blue this group of cells activates. Now imagine that your measurement apparatus selects three random locations to measure from. Figure 1.9 (b,c) show two possibilities in which the measurement returns highly biased results. In (b) no strengthened correlation will be detected because only one measurement site is located with the heterogeneity. In (c) all of the measurement sites will be highly correlated masking the abnormality of the heterogeneity.

One way to bypass this random location problem is to use a measure that provides data from every cell within a region. Another potential solution would be to use analysis techniques which are sensitive to long range correlations. Brain network criticality, the idea that any given firing is likely to cause exactly one other cell to fire, defines the point between full network avalanches and excitations which quickly die out. At the critical point, interaction become long range, potentially offering a

means of sampling the entire state of the network from any location. A third possible solution would be to show that brain networks store information in a distributed manner so that unlike what is shown in Fig. 1.9, the heterogeneity would be lightly stored in all of the synapses.

1.4.1 Functional and anatomical structure

Measuring structure from the correlation between neurons raises several concerns. As mentioned earlier, information is believed to be stored within synapses between anatomically connected neurons[55;56]. Correlations in neuron firing behavior are not the same as the strength of the synapse between neurons. Having measurements only between neurons with synapses would be ideal, however this is currently unfeasible for most network scale measurements. Yet, since firing behavior is the direct result of underlying anatomical connections, the correlations still carry limited information about anatomical connectivity. Correlations in neuron firing behavior indicate a functional relationship between the neurons. Functional connectivity does not have the clean biological interpretation of anatomical connections, but it does represent observed patterns in spiking activity and it represents the extent to which neurons encode similar features.

A method of extracting functional connectivity from spiking times of neurons is discussed at length in Chapter IV. This method identifies neurons whose spike times are temporally closer together than would be expected. Effectively, this identifies neurons that encode similar functional features. Figure 1.10 shows an example of functional relationship that can be found in simple data sets.

1.4.2 A path towards network dynamics

Suppose you can measure the functional connectivity of neurons accurately, what is the next step? One logical solution is to track the trajectory of functional connectiv-

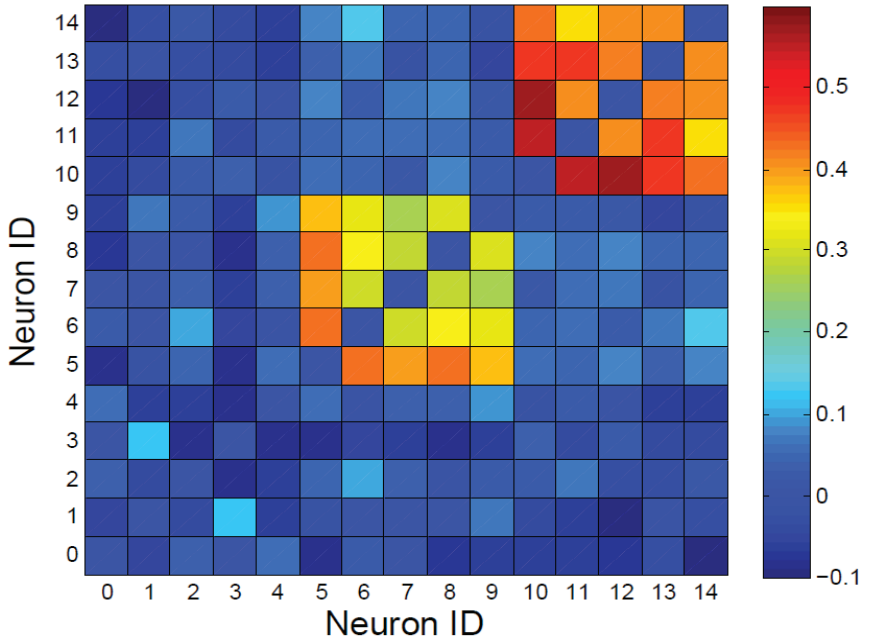

Figure 1.10: An example of network functional connectivity - The color of each box represent the functional strength between those neurons.

ity over time. If a single data set returns an image of the structure at a given moment, then a reasonable next step would be to combine images to create a movie of how the structure evolves in time. If one could implement this in practice, it would become possible to measure the change in individual and network level relationships. This would potentially make learning, or other distributed synaptic effects quantifiable.

Tracking all of the changes with a functional connectivity derivative is conceptually correct, but in practice is difficult to interpret given the high dimensionality of an n^2 matrix of relationships. It would be simpler to compress the complete matrix of network change into a single value denoting how much change has occurred between the two instances being compared. Compressing n^2 values down into a single value will mask smaller changes, meaning that a successful measure will rely on picking up changes in dominant or persistent changes across the network of functional relationships.

An example of a way to measure network evolution[57] is suggested in Fig. 1.11.

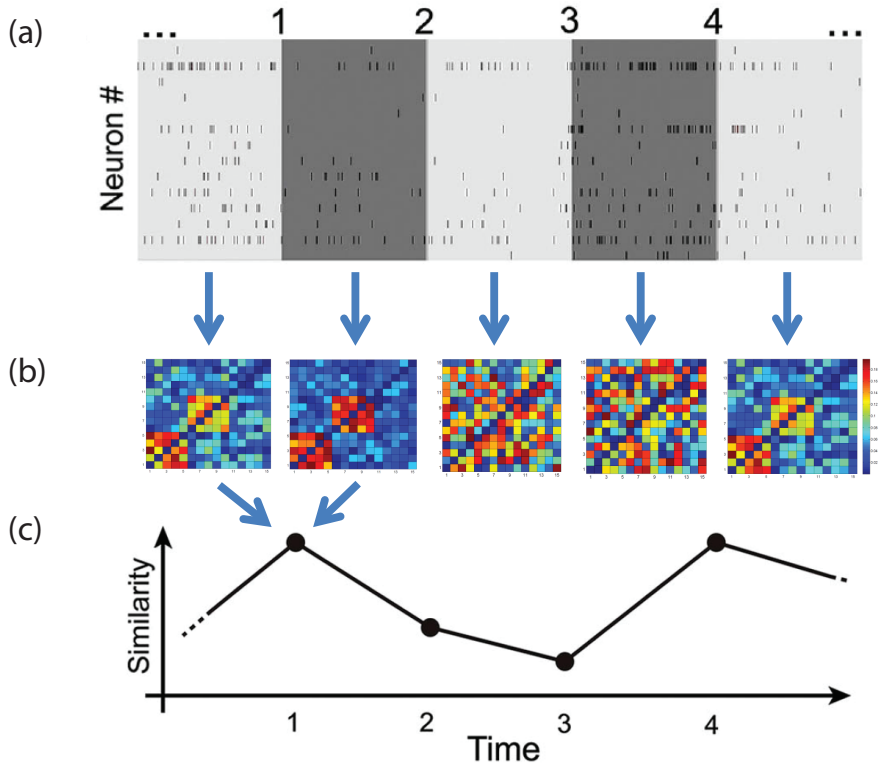

Figure 1.11: A simple way to measure network evolution - (a) Segment the data into consecutive time intervals. (b) Calculate the functional structure on each interval. (c) Compare the structure for adjacent windows to get a measure of how quickly the network is changing. Image adapted from *Ognjanovski 2014* [57]

Here network data is split into several segments. Each segment is analyzed and a functional connectivity representing the dynamics is created. Functional connectivity matrices from adjacent time periods are then compared, yielding a value which expresses how quickly the identified structure is evolving. Section 4.3 explains this process in more depth.

1.5 Outline

The aim of this dissertation is to characterize several types of interactions within the brain. Two broad classes of interactions will be expanded upon in the following chapters. The first class will be interactions between astrocyte like units. Here the

goal is to gain an understanding of how multiple transmission pathways influence activity patterns. Later, functional connections between neurons are used as the starting point for investigations into the evolution of network structure.

In Chapter II, interactions of a two process network are looked at in depth. A variant of the leaky integrate-and-fire model is used with active directed interactions and passive diffusive interaction. We demonstrate that, depending on the topology of the network, the two processes can either cooperate, and promote activity, or compete, and inhibit activity. We also show that the magnitude of the two process interactions is dependent upon the speed of the extracellular diffusion. This work[58] has been published in Nature Scientific Reports in 2014.

This two-process network model is applied to in vitro astrocyte networks in Chapter III. This chapter matches key simulation phenomena to activity of astrocyte transients. We show that the number, spatial characteristics, and temporal characteristics of astrocyte transients are reproducible with our two-process model. We are also able to match the shape of correlation vs. distance plots for networks with and without gap junctions. We use these findings to highlight the importance of gap junctions and extracellular diffusion for astrocyte signaling. This work[59] has been submitted for publication.

Attention is shifted to neuronal interactions in Chapter IV. The main emphasis in this chapter is to build up the tools needed to quantify network structure and changes in network structure. In the core component of this chapter we demonstrate a computationally fast method for extracting functional connectivity from time series. Later we discuss methods that can be used to compare functional structure and highlight stability as a particularly attractive approach. A methods paper explaining this worked is planned for future publication.

Finally, in Chapter V the framework of the previous chapter is used to look for indications of learning in the stability of functional network structure over time.

In simulations we show that the introduction of heterogeneity into the anatomical connectivity produces a measurable change in functional structure stability. This change is maximized in two biologically significant regions, network criticality and balanced excitation. We also apply stability to mice undergoing a learning task and show that changes in network functional connectivity align with the magnitude of learning in the mice. This work[60] has been submitted for publication.

CHAPTER II

Competition and cooperation between active network processes and passive ones defined in physical space

I introduce a reduced model of astrocyte interaction and show that the cooperation and competition arise for distinct topologies on networks with different types of local and directed connections. This chapter was published in Nature Scientific Reports in 2014(Vol. 4, Article Number 5269).

2.1 Introduction

Biological, social, and physical networks can be natural or man-made. Understanding the relationship between their structure and their dynamics is of great scientific interest[61;62;63]. Some of these networks can be studied in isolation because they interact very weakly with the space or the environment that they are embedded within. A citation network is one example of such a network - the physical location of the author does not affect the citation of their article. Other networks, however, are strongly affected by the physical space they sit in. These are usually referred to as spatial or geographical[64] networks. They are subject to constraints stemming from the interaction with the space. This interaction can take different forms, the most

common one is when constraints, which are dependent on the metric of the space, are imposed on the network topology. This could be a cost function which creates longer connections or a distance dependent probability of connecting to other network elements[54;65;66]. Another type of spatial interaction can be defined when the network topology is independent of spatial (environmental) constraints, but the dynamics within the network involves other processes that are linked to or defined within the embedding space. In these instances transport mechanisms on the network interact with those defined on the environment. Other examples come to mind: neuronal or astrocytic networks that are coupled through neurites/gap junctions/synapses, but also secrete chemicals into the extracellular space, or epidemiological networks where the disease spreads through personal contact and through diffusion of pathogens through the air[67].

In this chapter we study an example of such an interaction. We define a chemical agent which spreads actively through the network but is also secreted into the "environment" where it undergoes passive spread governed by diffusion. Thus the transport is composed of an active component which allows for (nearly) instantaneous spread of the agent through the network, with the macroscopic pattern of its spread being dependent upon the network connectivity, and the passive spatial spread outside the network, through "environmental" diffusion. The interaction of these two transport processes, as we will show below, may be highly nonlinear and result in complex spatio-temporal dynamics of the network nodes.

2.2 Methods

2.2.1 Model

The spread of the agent is governed by two mechanisms: active spread through network connectivity, e.g, gap junctions, and passive environmental diffusion. The

selected model describing the network nodes is very simple and is limited to charging and discharging elements that communicate through rapid equalization of the concentrations of the active agent. Such elements are relatively common in biology, and the model presented here roughly corresponds (to but is not limited) to astrocytic interactions. Passive diffusion is a natural choice for interactions through the environment as this is an extremely common mode of environmental transport that can be easily described and adjusted to represent topological details of the space. Selecting diffusion as the interaction mechanism in the network requires the addition of a release like mechanism, which is accomplished by having an agent flush which is assumed to originate from an internal storage (refer to Fig. 2.1).

The equation describing the nodal dynamics is a modified integrate-and-fire mod -el[24;68] :

$$\tau_E \frac{dX_i}{dt} = -\alpha X_i + I_{noise,i}(t) + I_{flush,i}(t) + \beta \sum_j A_{ij}(X_j - X_i) + \gamma \sum_j D_{ij}(r, t-\tau_j) \quad (2.1)$$

X_i is the amount of active agent within the i-th node. The element time constant is set to $\tau_E = 3$, while the nodal leak constant is set to $\alpha = 1$. The $I_{noise,i}$ is an instantaneous sub-threshold release defined as $I_{noise,i}(t) = \sum_{t_{n,i}} I_n[H(t - t_{n,i}) - H(t - t_{n,i} - \Delta T)]$. Here, H is the standard Heaviside function, noise amplitude $I_n = 2.1$; $t_{n,i}$ denotes a specific noise instance; $\Delta T = 1$ is the pulse duration. The noise arrives randomly at a given node with probability $p_n = 0.01$. $I_{flush,i}$ describes the internal auto-release current when the level of the agent reaches the threshold, $X_i = 1$:

$$I_{flush,i}(t) = I_{amp}(e^{\frac{-(t-\tau_i)}{C_1}} - e^{\frac{-(t-\tau_i)}{C_2}}), \quad (2.2)$$

where τ_i denotes the timing of the last threshold crossing in simulation steps. The size of the internal release is set to $I_{amp} = 1.5$. The wave form is modeled as the

difference between a slow, $C_1 = 300$, and a fast, $C_2 = 30$, exponential. Note that I_{flush} has a strong positive phase shortly after its activation which decays away over the duration of its refractory period. The refractory period, 1000 timesteps, prevents continuous activation of the system.

The final term on the RHS describes the effect of the external, or environmental, excitation arriving at each network element. γ is the coupling amplitude, and $D_{ij}(r, t - \tau_j)$ is the solution of the two dimensional diffusion equation at a distance r and time t in the space embedding the network.

$$D_{ij}(r, t - \tau_j) = \frac{N}{4\pi D^*(t - \tau_j)} e^{\frac{-r^2}{4D^*(t-\tau_j)}} e^{-\zeta(t-\tau_j)} \tag{2.3}$$

For most of the simulations (except Fig. 2.5) $N = 100$ is the amplitude of neurotransmitter release. The diffusion constant is $D^* = .1$, and the time decay constant of the agent in the external environment is $\zeta = .01$. For simplicity we assume that the element releases the agent into the physical space only when its value is suprathreshold. Equation 2.3 approximates the diffusion a release from a point in an open environment and should therefore be thought of as a rough approximation of the extracellular environment. The diffusion and time decay constants where chosen to provide reasonable firing rates.

We use a Small World paradigm[69;70] to vary the network connectivity; initially the connections are set locally within given radius and then randomly rewired with probability p. The nodes are coupled through diffusive coupling with efficacy β, with the connection from element j to element i denoted by A_{ij} taking the value 0 or 1. This paradigm allows for the range of network connectivity structures, from local to random connections, to be controlled by the rewiring parameter, p. The strength of the active transport ($\beta = 0.00 - .08$) is limited by the amount of excitatory agent that it is capable of sending out at any moment, as well as how much a given element

retains information of its past. The overall dynamics of the system strongly depends on the amount of the diffusive agent and its feedback interaction with the nodes. The parameters are chosen so that small network and environmental interactions result in a quiescent network while large environmental feedback results in hyperactivity of the nodes. The parameters near this transition were of interest ($\gamma = .08 - .14$).

2.2.2 Simulations

The model was simulated on a two dimensional network consisting of 1600 oscillators on a 40x40 grid with periodic boundary conditions. The active connections on the network are initially assigned a radius $R = 2$. The network was initialized with no activity or charge present and allowed to evolve for 50,000 timesteps using Euler's method. The initial 10,000 timesteps were removed from the analysis to allow the network to transition away from its (random) initial conditions. The figures displayed are analyzed over nine runs of the simulations for each set of parameters (β, γ, p).

2.2.3 Analysis

The mean nodal frequency is calculated as the number of times any oscillator surpasses the charging threshold divided by the product of the number of oscillators and the timesteps in the simulation and then normalized. A frequency of one corresponds to a maximal raw firing frequency which is limited by the refractory time, $f_{max} \sim \frac{1}{1000}$. The units thus are not tied to actual timescales due to the generality of the model.

The mean phase coherence[71] measures the degree of locking between nodal activations, and is calculated from the relative nodal activation times. The pairwise mean phase coherence is defined by:

$$R_{ij} = |\frac{1}{N}\sum_{k=1}^{N} e^{-i\phi_i(t_{j,k})}| \tag{2.4}$$

Where $\phi_i(t_{j,k})$ is the instantaneous phase of the j-th node relative to the i-th node at j's activation at time, $t_{j,k}$, and is given by, $\phi_i(t_{j,k}) = 2\pi \frac{t_{i,k,2} - t_{j,k}}{t_{i,k,2} - t_{i,k,1}}$. Here $t_{j,k}$ is the k-th activation time of node j and $t_{i,k,1}, t_{i,k,2}$ are bracketing activation times of i-th node such that $t_{i,k,1} \leq t_{j,k} \leq t_{i,k,2}$. The network wide mean phase coherence is the arithmetic average of the pairwise mean phase coherence.

2.3 Results

We define a network composed of simple excitable integrate-and-fire elements (see Methods and Fig. 2.1 for a detailed description). When the level (or concentration) of an agent in the element exceeds a threshold, the element rapidly releases the agent from its internal stores (Fig. 2.1(b) into the network and the surrounding physical space (Fig. 2.1(a). The transport on the network is an active process - the signal spreads instantaneously to other nodes connected with the activated node through standard diffusive coupling. At the same time, the signal spreads passively via a purely spatial diffusion process, the nature of which is determined by the spatial extent and properties of the physical space, Fig. 2.1(a). For simplicity, we consider that both these mechanisms only have positive signs - i.e they both spread excitation.

This system loosely corresponds, for example, to astrocytic networks in the brain. Astrocytes, in simple terms, release calcium stored in the endoplasmic reticulum into the cytosol, which increases free calcium levels in the cell[72]. This calcium spreads through gap junctions to other astrocytes, but at the same time activates complex chemical cascades responsible for the release of glio-transmitters into the extracellular space. Glio-transmitters in turn can stimulate other cells (neurons or astrocytes) in the spatial vicinity[73;51].

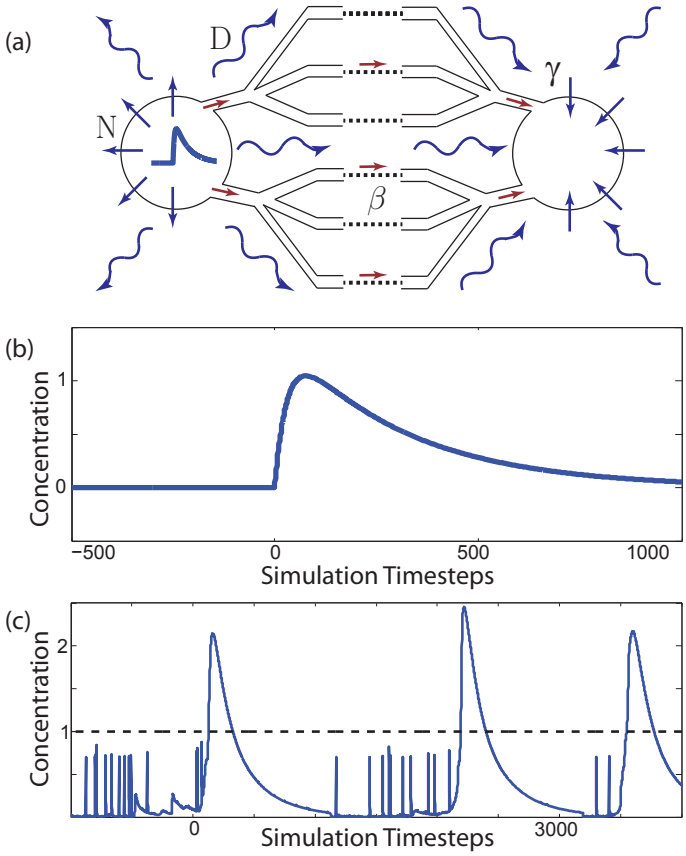

Figure 2.1: Description of the two process model - (a) Graphical depiction of the model highlighting bimodal interactions from the active element (left) to the charging element (right). The processes underlying this interaction are 1) the active pathway through the network, defined by connectivity parameters (connectivity radius R, rewiring parameter p) and diffusive network coupling constant β, and, 2) the passive environmental diffusion, where N amount of the agent is emitted into the embedding space, diffuses subsequently with speed determined by the diffusion constant D over to the charging element, which absorbs it with proportionality constant γ. (b) The time dependence of the release of the agent from internal nodal stores occurring after the node reaches the concentration threshold. (c) An example of the time evolution of agent levels within a single node; the small short spikes represent instantaneous changes in agent concentration due to noise, after the threshold (dashed line) is reached the node releases large amounts of agent into the network and its immediate environment.

2.3.1 Cooperation and competition are functions of network topology

While the specific dynamics of network elements can take different forms, we show that, depending on the connectivity of the network, the active network transport and the passive environmental transport sometimes cooperate in spreading the excitation throughout the network and at other times compete, effectively inhibiting propagation through the system.

We investigate the spatio-temporal pattern formation within the network as a function of the network topology, the strength of network connections, and the feedback amplitude between the environment and the network nodes. It is well established that if the magnitude of either network coupling or environmental feedback amplitude is large enough then that process alone can drive the formation of sustained large-scale spatio-temporal patterns[74;75;76]. However, we observe that for intermediate coupling values of both processes a strong dependence on network topology emerges.

For local network topologies the two transport mechanisms cooperate, forming globally propagating waves, while for random topologies the processes compete, impeding signal propagation throughout the system. This effect is shown on Fig. 2.2 which shows the mean nodal frequency and mean pairwise phase coherence (MPC) between network nodes as a function of the magnitude of the feedback between the environment and the nodes (γ), and efficacy of network connectivity (β) for four different network topologies. When the network is effectively disconnected ($\beta \to 0$) and $\gamma \leq 0.11$ the mean frequency of nodal activity is low as it is driven only by external noise. When a certain amplitude ($\gamma = 0.11$) of nodal interaction with the environmental agent is reached the network enters a high activity global activation state (Fig. 2.2). However, if the amplitude of network coupling is increased for local network topologies ($p = 0$) the transition to sustained global activation of the network takes place for lower values of γ (Figs. 2.2(a), 2.2(c) - the two transport processes cooperate. In contrast, for global network topologies ($p = 1$) sustained net-

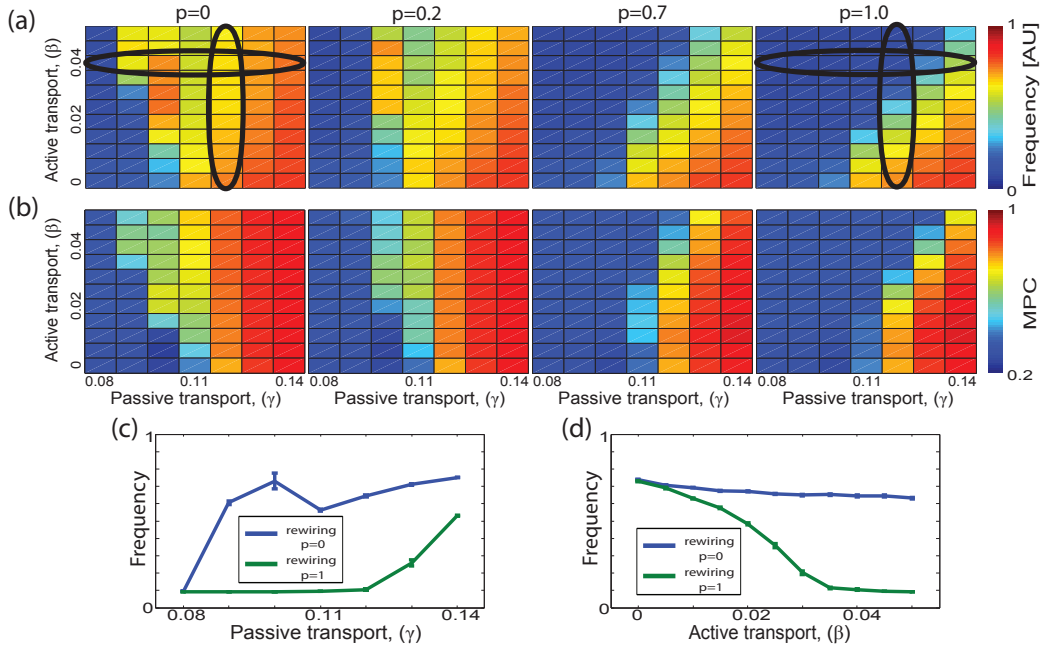

Figure 2.2: Frequency and MPC as functions of transport strength of topology - Changes in mean nodal frequency (a) and mean phase coherence (b) as a function of relative strength (amplitude) of both transport processes (x-axis - strength of interaction of the nodes with the physical space γ, y-axis - efficacy of network connectivity β) and network topology. Every location represents results averaged over 9 simulation runs. c) Changes of nodal mean frequency for local (blue) and random (green) network topologies as a function of passive transport amplitude (γ) ; $\beta = 0.04$. d) Changes of mean frequency as a function of the active transport amplitude (β) for local (blue) and random (green) network topologies; $\gamma = 0.12$.

work activation is significantly delayed as γ increases (Figs. 2.2(a), 2.2(c) - the two transport processes compete, impeding each other. Figures 2(c) and 2(d) summarize the difference in network activation for the two topologies as a function of both the magnitude of network transport and the environmental feedback. The increase of network coupling can play reverse roles in affecting the global network activation depending on the network topology.

2.3.2 Local networks cooperate

For local network topologies the cooperation of the two processes is due to the fact that both processes support local signal propagation from a recently activated node to its neighbors. Active network transport is faster (it is instantaneous) than environmental diffusion. However, on short spatial scales, the excitation stemming from the two processes can partially coincide providing supra-threshold excitation and leading to activation of new nodes in the proximity of the active site. As this process continues away from the originating site it forms large scale propagating waves within the network. The formation of local patterns that propagate through the network depends on the interplay between the magnitude of the diffusion constant, D, and the signal decay constant α in Equation 2.1. The transition to global activation patterns as a function of the magnitude of network coupling is depicted in Fig. 2.3(d), where we show co-activation patterns between network nodes giving global and local changes of mean phase coherence and cross-correlation in network activation sites. For weak network coupling (Fig. 2.3, location i), diffusion itself can not sustain large enough areas of local activation for the signal to spread globally through the network. Instead, random local domains are being formed and then dissipate quickly. This leads to relatively low correlation between the activation of network nodes (Fig. 2.3(b). The typical size of the formed domains can be inferred from the distance dependence of cross correlations between the nodal activation patterns (Fig 2.3(c).

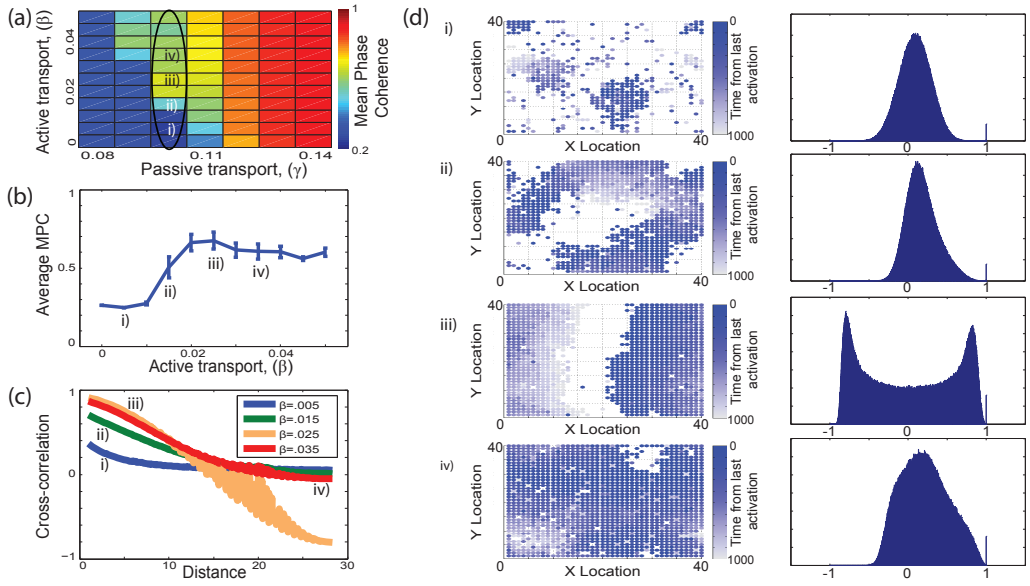

Figure 2.3: Formation of global activity patterns in networks with local connectivity - (a) Changes of the mean phase coherence as a function of active and passive transport amplitudes. (b) Mean phase coherence as function of active transport amplitude for $\gamma = 0.10$. (c) Mean cross-correlation between pairs of nodes as a function of distance within the network. (d) Examples of network activation at a time t (the difference between the current time and the time of the last nodal activation), and histograms of pairwise cross-correlation values for different active transport amplitudes (as denoted in a).

Characteristic network activity plots show the evolving size of synchronous excitations (Fig. 2.3(d), left row). Histograms of pairwise cross-correlation values are Gaussian due to the stochasticity of the activated locations (Fig. 2.3(d), row i right).

For intermediate levels of network coupling (locations ii and iii in Fig. 2.3), the domains spread through the network forming first irregular large scale activation patterns (Fig. 2.3, location ii), and then organizing into propagating waves (Fig. 2.3; location iii). Large irregular areas of activation lead to slower spatial decay of the cross-correlations (Fig. 2.3(b), and a significant skew toward positive cross-correlation values on the pairwise histogram (Fig. 2.3(d), row ii right). Formation of regular propagating waves through the network (Fig. 2.3, location iii), is characterized by strong correlation of nodal activity in the direction normal to the wave propagation, and anti-correlation in the direction of wave propagation (Fig. 2.3(b,

d); location iii). These regular waves result from the front of activation closely following nodes which have recently recovered from the previous cycle of activity. The match between the nodal refractory time and the speed of the wave propagation also explains the observed non-monotonic behavior of the mean nodal frequency (Fig. 2.2(a). Further strengthening of the coupling of either process increases the speed of network activation, which in turn leads the excitation to self-extinguish due to the nodal refractory time. The activation needs then to be randomly restarted which leads to a reduction of the mean nodal frequency. The non-monotonicity resulting from the size of the environment does not change the overall observation that global network activation occurs at lower coupling strengths for local network connectivities as opposed to higher coupling values for random ones.

Finally, when the network coupling is high the whole network activates quickly (Fig. 2.3(d); location iv). The location initiating the burst and the pattern of spread are random. Furthermore, anti-correlated islands may form if a given location was recently activated because of the noise and is in its refractory state.

2.3.3 Random networks compete

For random network topologies (rewiring probability $p = 1$) increases in network connectivity strength have the opposite effect. Even for relatively strong interactions with the environment, the network is unable to support global activation patterns. The high level of connectivity drives the network towards homogeneity. The agent accumulated locally will quickly be transported to other locations, effectively reducing the local activation and preventing the nodes from activating. Only when the external feedback is strong enough to counteract this dissipation can the network support sustained activation (Fig. 2.4), leading to competition of the two processes. The network effectively supports only two modes of activity: random with formation of small domains (Fig. 2.4(a) locations ii and iii) and fully synchronous (Fig. 2.4(a)

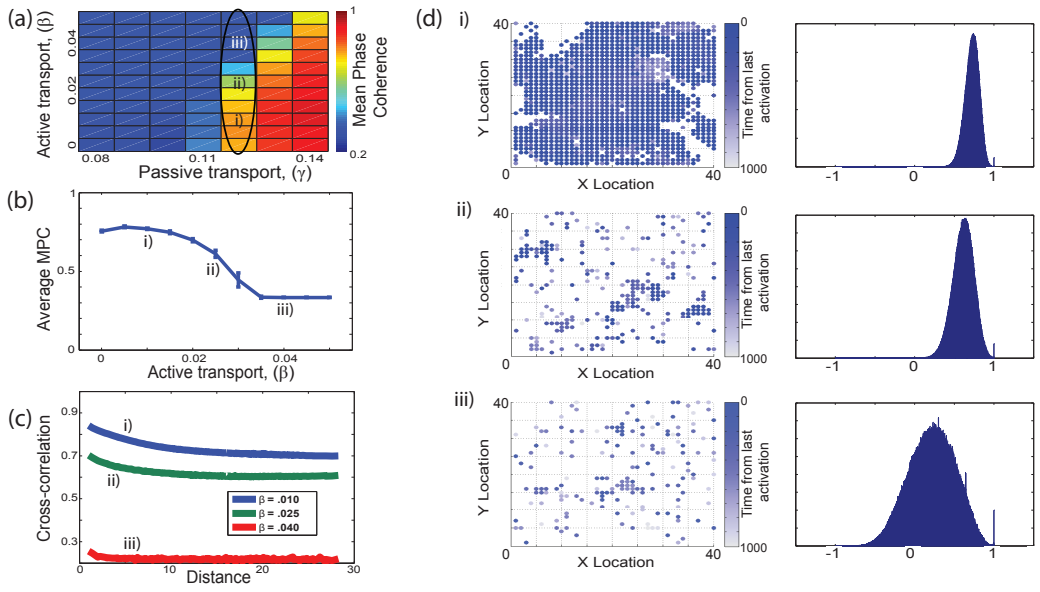

Figure 2.4: Formation of global activity patterns in networks with random connectivity - The individual panels correspond to those in Fig. 2.3.

location i).

2.3.4 The influence of the diffusion constant

We also investigated how the diffusion constant, D, affects the degree of cooperation or competition in the system. To do this we subtracted the mean frequency, or mean phase coherence, for the active process case with no coupling ($\beta = 0.00$) from that with strong coupling ($\beta = 0.05$), Fig. 2.5(a, b). Comparing this baseline change for both metrics allows us to elucidate the extent to which the active process advances or delays changes in the frequency and MPC due to an increase in diffusion speed. We calculated the total area under the curves in Fig. 2.5(a) and (b) for all investigated values of γ, Fig 2.5(c, d).

The competition and cooperation patterns vary for both quantities and for both local and random network topologies. For local network connectivity, lower diffusion speeds lead to overall cooperation, whereas higher ones lead to competition. The general pattern of change in this case is similar for both frequency and MPC. The

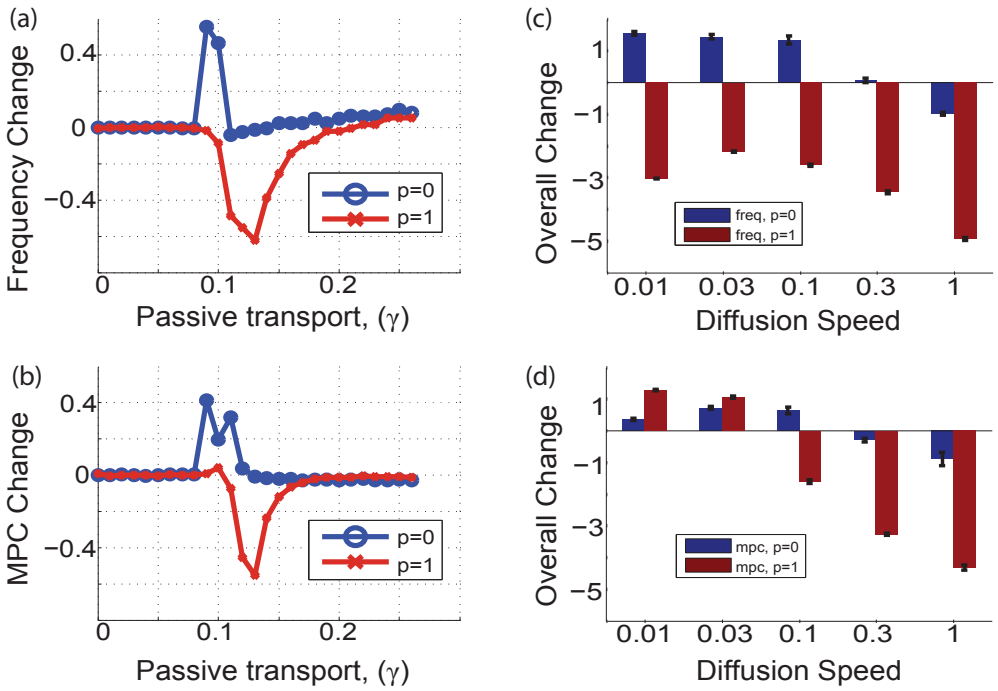

Figure 2.5: Cooperation and competition for varying diffusion speeds - Cooperation and competition of active and passive processes as a function of changes in frequency and mean phase coherence (MPC) as functions of diffusion speed, D^*. (a) Change in frequency between $\beta = 0.05$ and the baseline ($\beta = 0$) as a function of passive transport strength. (b) Change in MPC between $\beta = 0.05$ and the baseline ($\beta = 0$) as a function of the passive transport strength. In panels a and b positive change denotes cooperation, while negative values denote competition. (c) Total increase and/or decrease in the frequency across all values of γ due to the active process (calculated as a area under the curves in (a)). (d) Total increase and/or decrease in the MPC across all values of γ due to the active process (calculated as a area under the curves in (b)).

situation is different for networks with random connectivity. Here, the frequency shows competition for all of the speeds tested but its magnitude is non-monotonic with the diffusion speed (Fig. 2.5(c). At the same time, for random topologies, the degree of cooperation and competition as reported by mean phase coherence changes largely monotonically as a function of the diffusion speed (Fig. 2.5(d).

The complex interaction of the two processes can be attributed to matched, for cooperation, or mismatched, for competition, patterns of agent spread, as supported by the two processes. The local spread of diffusion is defined by its speed, which determines the spatial range and the time scale within which the local agent level is affected. Network connectivity, on the other hand, determines the ratio of the local to global signal spread through the system. While the transmission speed here is largely instantaneous, the effective speed of signal spread depends on actual activation levels of the nodes; a single activation of a node by the active process usually is not enough to trigger activation of a given site and is contingent on further agent increase from other sources. Thus if the spread of passive and active processes match in their spatial scope and the timescale, then the two processes cooperatively may lead to activation of subsequent network sites far from the original one. This however, due to the intrinsic properties of diffusive signal spread, may only happen for local network topologies.

At the same time, competition arises when the activation of the nodes by one process is impeded by their earlier activation by the other process. This is predominantly (but not only) observed for random topologies. In this case the spatially random activation of nodes can be driven by two processes - noise and active spread from other sites through random connectivity. While both processes are independent of each other, activation of a given site (due to noise or active spread) and subsequent local activation of its neighbors due to passive agent spread through diffusion precludes instantaneous activation of that site due to the nodal refractory time since a node will

not fire within a predefined time window after its activation. Thus the two processes compete for access to available nodes limiting the overall activation frequency.

2.4 Discussion

We have shown that network topology together with feedback from the external environment in which the network is embedded, may constitute a determining factor for the creation of sustained large-scale spatio-temporal patterns in a excitable system. We showed that local network topologies may cooperate with passive environmental transport to create globally propagating excitation through the system, whereas for random network topologies the two processes compete, increasing significantly the threshold in magnitude of the environmental transport needed for global patterns to occur. These results should be of importance in any system where the interaction of the network with its embedding environment can not be neglected.

CHAPTER III

Modeling cultured astrocyte networks

In this chapter I show that the number, spatial characteristic, and temporal characteristic of astrocyte transients are reproducible with the two-process model introduced in the prior chapter. Liz Shtrahman performed all of the culture experiments and the analysis of the fluorescence data. I performed the simulations and analysis of the simulations. This chapter has been submitted for publication to Journal of Physical Biology.

3.1 Introduction

Networks of interacting components are known to self organize and form complex macroscopic structures, which emerge from local coupling between individual network components[77;78]. The brain is an example of a system with self-organizing dynamics; it contains an astronomical number of neurons and glia that interact over multiple spatial and temporal scales. Patterns of brain activity within these interacting networks underlie our thoughts and memories, and drive behavior. These interactions are mediated through different cell populations and through various mechanisms such as synaptic coupling, gap junctions, and neuromodulation. The most researched types of interactions in the brain are those mediated by neurons. Traditionally, glial cells were thought to provide primarily structural and metabolic support for neurons[40]. How-

ever, recent work suggests that glia may be active participants in brain information processing. Within the last decade it became clear that astrocytes, a sub-population of glial cells, play an important role as modulators of neural activity.

Astrocytes have been shown to display dynamic calcium transients in both *in vitro* and *in vivo* preparations[79;80;81;82;49]. Astrocyte calcium signaling is involved in many processes including biochemical pathways that activate the extracellular release of a variety of transmitter molecules, which can interact with other astrocytes and also with neurons. For example, the release of ATP or glutamate from a single astrocyte has been shown to activate calcium transients in other astrocytes[83;52;84]. Moreover, it has been shown that a single astrocyte can envelop up to 140,000 neuronal synapses, putting them in a unique position to control neuronal domains[45]. These astrocytic processes are endowed with various G-protein coupled receptors that, among others, evoke the cell's calcium responses[39]. Thus there is a bidirectional communication between neurons and astrocytes, and this notion led to the formulation of a tripartite synapse concept, in which astrocytes play a prominent role in regulating neuronal signaling at a synaptic level[85]. Therefore, patterns of calcium signaling in astrocytes can be important for shaping neuronal network formation and development. Even though the functional effect of astrocytes on neurons is complex and poorly understood, it is clear that astrocytes have a role in brain function that needs further study.

The research done on the involvement of astrocytes in modulating neuronal processes has mainly focused on the single astrocyte level. However, the local interactions are embedded in complex network interactions. Astrocytes couple to each other through direct connections called gap junctions, and form a cellular network of interacting cells[86]. Small molecules can diffuse passively through gap junctions, and it has been shown that calcium activated release of the molecule inositol trisphosphate (IP_3) is involved in the communication between gap junction coupled astrocytes[87]. At the same time astrocytes secrete and uptake signaling molecules from the extracel-

lular space. These molecules can diffuse, forming another class of signaling pathways. The interaction of these two coupling mechanisms, diffusion of extracellular chemical signaling and direct gap junction coupling, can lead to complex spatiotemporal patterning of the network activity, which has been demonstrated in recent work[58]. Here, we examine the network dynamics of spontaneous calcium signaling formed in dissociated cultured astrocyte networks to investigate the interaction of extracellular diffusion and network transport mechanisms. We show that key behaviors of unaltered astrocyte networks and astrocyte networks with weakened gap junction coupling are reproduced in the computational model.

3.2 Methods

3.2.1 Cell cultures

Dissociated cell cultures: We prepared hippocampal cell cultures from Wistar rats on postnatal day 1 using a protocol modified from *Hales 2010*[88]. Tissue was digested with %0.5 Trypsin-EDTA(Invitrogen) diluted in Hanks Balanced Salt Solution (Invitrogen) and then dissociated by titration with a pasteur pipette. Cells were centrifuged and re-suspended in Neurobasal-A medium (Gibco) supplemented with 2% B-27 (Gibco), 5% heat-inactivated horse serum (Gibco), $0.5mM$ L-glutamine (Sigma-Aldrich), $0.5mM$ pen-strep (Sigma-Aldrich) and $10mM$ HEPES (Sigma-Aldrich). The cell density was adjusted to a final plating density of $1500\frac{cells}{mm^2}$. Bi-weekly, half the culture medium was replaced with fresh medium.

Calcium imaging: Cultures were imaged at 5 days in vitro using calcium indicator Fluo 4-AM (Invitrogen) and astrocyte marker[89] sulforhodamine 101 (Invitrogen). Fluo 4-AM and sulforhodamine 101 were diluted to final concentrations in HEPES-buffered saline containing the following: $119mM$ NaCl, $5mM$ KCl, $2mM$ CaCl2, $2mM$ MgCl2, $30mM$ Glucose, $10mM$ HEPES, and pH adjusted to 7.4. For imaging,

the culture medium was replaced by $5\mu_g/mL$ fluo4-am and incubated for 40 minutes at room temperature, following a second incubation with $5\mu M$ sulforhodamine 101 for 20 minutes at room temperature. Cultures were gently washed with HEPES-buffered saline 3 times following incubations. Cultures were maintained at 35 degrees Celsius during imaging. Olympus microscope IX71 was used for wide-field fluorescence imaging, and recorded with Hamamatsu Digital CCD camera C10600 at (6.4 Hz frame rate). MetaMorph software was used for data collection; all further analysis was done with Matlab.

Micro-electrode Arrays: Dissociated cells were plated on 60-electrode glass microelectrode arrays (Multi Channel Systems, Reutlingen, Germany), with $30\mu m$ diameter electrodes and $200\mu m$ spacing between electrodes. Contact pads and tracks were transparent to allow for optical imaging. Microelectrode arrays were cleaned and treated with 0.05% poly-ethylene-imine (Sigma-Aldrich) in borate buffer followed by the $20\mu g/mL$ 1 laminin (Roche Applied Science) solution in media following the protocol of *Hales 2010*.

Pharmacological Treatment: 18-β glycyrrhetinic acid (BGA) (Sigma-Aldrich) was dissolved in dimethyl sulfoxide (DMSO) into 1000x stocks and stored at -20°C. BGA stock was diluted in HEPES buffered saline to a final concentration of 25 μM. To disrupt gap junctions, cultures medium was replaced by 25 μM BGA solution and incubated for 15 minutes at 35 degrees[90]. An equivalent volume of vehicle replaced the medium in control cultures. Following incubation, cultures were gently washed with HEPES-buffered saline three times and imaged five minutes later.

Cell detection and event detection: Fluorescent imaging was acquired with commercially available MetaMorph Microscopy Software for Olympus Basic and imported into MATLAB for semi-automatic cell contour detection using custom software[91] modified from the Rosa Cossart lab. All subsequent analysis was performed with custom programs in MATLAB. Astrocyte somas were detected in the sulforho-

damine 101 image, and the fluo4-am fluorescence signals were processed by wavelet filtering of the raw signal and event detection was determined by thresholding the signal above baseline. Each fluorescence signal was examined and any false positives and negatives in the event detection were corrected.

3.2.2 Pattern recognition

Fractional Change Measures: Fractional change was calculated for various quantities as the value after condition (A) minus the value before condition (B), and normalized by their sum ($A + B$).

$$\Delta = \frac{A - B}{A + B} \tag{3.1}$$

Spatial clustering: We defined the spatial clustering distance, D_{exp}, as the average distance between all closest pairs of astrocytes with calcium events during an imaging experiment. To compare between experimental conditions with varying numbers of active astrocytes, we compared D_{exp} to the value of the spatial clustering distance for randomized networks (D_{rand}). Namely we randomized locations of active astrocytes distributing them randomly among experimentally identified locations (as measured with sulforhodamine 101) of all astrocytes. The average randomized distance between active cells, D_{rand}, was computed for over 50 sets of randomizations and compared to that observed experimentally. To quantify the spatial clustering we define a spatial clustering measure given by,

$$C = \frac{D_{rand} - D_{exp}}{D_{rand} + D_{exp}} \tag{3.2}$$

where C is the relative change of the spatial clustering distance for experimental data (D_{exp}) with the spatial clustering distance for randomized networks (D_{rand}).

Autocorrelation Widths: The autocorrelation function was calculated for each

astrocyte calcium fluorescence signal. To determine a measure of the autocorrelation signal width, we calculated the time lag at a half maximum of the autocorrelation, where the total height is determined by the peak of the autocorrelation at the location the first derivative of the autocorrelation crosses zero. Using the time lag at the autocorrelation half maximum as an indicator for the timescale of astrocyte calcium signal duration, we computed the average time lag for all signals in an imaging experiment and the relative change in time lag for pharmacological treatments.

Cross Correlations: The cross correlation function was calculated between all pairs of astrocytes in a network for time lag shifts between -90 seconds and 90 seconds. Cross correlations were binned according to astrocyte distance and then averaged. The temporal ordering is not relevant for obtaining a measure of total average correlation at a distance. Therefore, to avoid averaging out positive and negative time lags, all cross correlations with negative maximum time lags were reflected across the y-axis. This way, only the magnitude of the time lag is averaged across pairs.

3.2.3 Modeling and simulations

Model Astrocyte Network: The astrocyte network model is a two process modified integrate-and-fire model, and follows the description in *Maruyama 2014*. The key feature of the model is that it contains a direct coupling interaction, gap junctions, and an indirect coupling term, representing diffusive extracellular coupling. Astrocytes are depicted as the nodes of the network and nodal activity, which models the internal Ca^{2+} concentration, is driven by random noise, internal release, and extra-cellular excitation from other active astrocytes. An integrate-and-fire model was chosen as the basis for the nodal dynamics for its simplicity and its ability to grossly encapsulate the desired pathways. The release of Ca^{2+} from the endoplasmic reticulum (ER) is represented by an internal flush of nodal agent upon exceeding a charging threshold. At all times the internal concentration is allowed to interact

with other connected astrocytes through gap junctions via an equilibrating term (see equation below). In addition to the internal release, breaching the charging threshold is accompanied by a diffusive flush of signaling into the extracellular space, which allows astrocytes to passively influence neighboring astrocytes. While it is clear that these two pathways are mediated by (many) other signaling molecules, here we assumed for simplicity that the extracellular signaling will affect the calcium levels in an astrocyte by activating G protein coupled receptors.

Thus, the full equation describing the dynamics is as follows:

$$\tau_E \frac{dX_i}{dt} = -\alpha X_i + I_{noise,i}(t) + \beta \sum_j A_{ij}(X_j - X_i) + \gamma \sum_j D_{ij}(r, t - \tau_j) \tag{3.3}$$

Variables are the same as in the published model paper *Maruyama 2014*, with the following exceptions, leak constant ($\alpha = 0.5$), speed of diffusion($D^* = .001$), and amplitude of diffusion release(N=1000).

Here X_i denotes the concentration of Ca^{2+} present in the i^{th} astrocyte. α is the leak constant controlling the auto-decay of calcium levels in the cell ($\alpha = 0.5$). I_{noise} describes random excitation experienced separately by each astrocyte. The random excitation occurs with a probability p=.01 and is represented by a short stimulation pulse. I_{flush}, on the other hand, represents the release of Ca^{2+}+ from the ER into the interior of the cell. The form of the release is modeled as an exponential decay in order to capture experimental timescales, with I_{amp} controlling the overall amplitude of the release:

$$I_{flush,i}(t) = I_{amp}(e^{\frac{-(t-\tau_i)}{C_1}} - e^{\frac{-(t-\tau_i)}{C_2}}) \tag{3.4}$$

Astrocytes form a 2D lattice to parallel the experimental observations. The next term on the RHS of Equation 3.3 describes the gap junction coupling term. Here the parameter β denotes the efficacy of coupling. The range of gap-junction strengths is limited by the overall amount of agent (Ca^{2+}) an astrocyte can send out. Higher

values indicate a greater sharing of agent amongst astrocytes and less retention of their individual concentration level. Network connections are represented by the astrocyte adjacency matrix A_{ij}, where $A_{ij} = 1$ if cells i and j are directly coupled and $A_{ij} = 0$ otherwise. The gap junction coupling, $X_j - X_i$, is a standard term describing gap junctions that allows for rapid equilibration of Ca^{2+} concentrations at different nodes. Astrocytes are initially coupled via gap-junctions to all neighbors within a radius, $R = 2$. Results are shown for local connectivity, and similar results were obtained for networks with a small portion of the connections (10-20%) randomly rewired.

The last term on the RHS of Equation 3.3 represents the extracellular diffusive coupling of astrocytic transmitters. The function:

$$D_{ij}(r, t - \tau_j) = \frac{N}{4\pi D^*(t - \tau_j)} e^{\frac{-r^2}{4D^*(t-\tau_j)}} e^{-\xi(t-\tau_j)} \tag{3.5}$$

reflects the distance and time based effect a cell j will have on cell i given the distance between cells is r, and the time since j had a Ca^{2+} event, $t - \tau_j$. D_{ij} is the solution of the 2D diffusion equation in open space. The strength of this extracellular diffusion is controlled by the coupling parameter γ. The gap junction and diffusive coupling parameters are both set to the range of values so that the network activity ranges from quiescence to bursting behavior.

Simulation Details: Simulations were run on a 40x40 grid of astrocytes. The cells were evolved, via Euler's method for 40,000 time-steps, with step size one, after randomizing the initial conditions by evolving the network for 10,000 time-steps. The figures displayed represent the averages over four simulations.

3.3 Results

We have grown mixed hippocampal cell networks in primary cultures and measured astrocytic activity utilizing optical imaging with the calcium sensor Fluo-4AM, while neuronal electrical activity was monitored using microelectrode arrays (see Methods Section 3.2.1 for a detailed description). Here we are interested in early development of the networks during the first week *in vitro*. During early development, astrocytes form networks and display spontaneous calcium signaling while there is no electrical neuronal activity. However this is an active period for synapto-genesis and it is known that neurons release various signaling molecules at that time[92]. We observed robust patterns of calcium activity during the first week in culture before spontaneous action potentials in neurons were observed on the microelectrode arrays. The neurons became subsequently electrically active after 7 DIV (days *in vitro*). We imaged the spontaneous astrocyte calcium transients of hundreds of astrocytes over several minutes during the first week in vitro (Fig. 3.1). To identify individual astrocyte somas, we used concurrent staining with sulforhodamine 101 which selectively labels astrocytes[89]. The astrocytes were identified as the cells that were co-labeled with both markers.

In parallel we have constructed a computational model of astrocyte-astrocyte interactions. Based on the known experimental results[45] we simulated two major means of signal transduction: network transport through astrocytic gap junctions, and chemical transport through diffusion in extracellular space. The reduced cellular activity is modeled through integrate-and-release dynamics. In short, incoming excitation can cause Ca^{2+} to be released from the internal stores to propagate throughout the cell, and then continue on to spread to the associated network. While it is clear that astrocyte signaling is multimodal and extremely complex, we implicitly assumed that the extracellular agents act directly on calcium concentration within a cell and we modeled it as one species. The properties of this model were extensively stud-

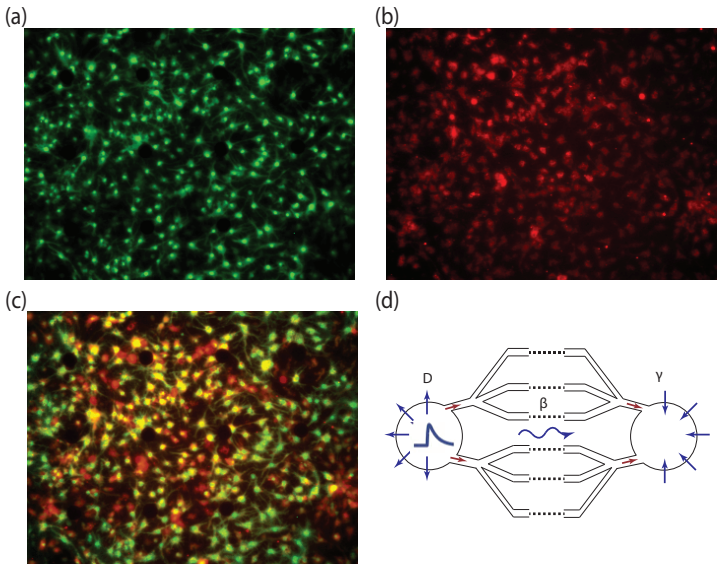

Figure 3.1: Fluorescence imaging of spontaneous astrocyte calcium transients in dissociated hippocampal cultures - (a) Example fluorescence image of calcium indicator fluo-4am. (b) Example fluorescence image of astrocyte marker sulforhodamine 101. (c) Overlay of fluo-4am and sulforhodamine 101 images, yellow marks astrocytes co-labeled with both dyes. (d) Schematic of model shows the gap junction and diffusion pathways of astrocyte coupling.

ied in recent work[58]. We have shown that depending on connectivity properties of gap junctions the two processes (network transport and extracellular diffusion) can cooperate, strengthening the network activity, or they can compete, inhibiting each other and subsequently lowering the network response[58]. Here we assumed that astrocytic connectivity is primarily local as there are no long-distance connections between astrocytic processes[93].

3.3.1 Gap junctions control the number of spontaneous calcium transients

Figure 3.2a shows an example raster plot of the fluorescence intensity over time for an astrocyte network during four minutes of imaging. Each row displays the changes in calcium fluorescence over time for individual astrocytes rescaled between the fluorescence intensity signal's minimum(black) and maximum(white). To better understand the effects of calcium signaling on an astrocytic network, we perturbed these spontaneous Ca^{2+} patterns by pharmacological disruption of the gap junction coupling strength between astrocytes. To disrupt gap junction coupling, we incubated cultures in $25\mu M$18-β glycyrrhetinic acid (BGA) for 15 minutes (see Methods 3.2.1). We found that the number of astrocytes with spontaneous calcium transients is dependent on gap junction coupling strength between cells (Fig. 3.2b). Following incubation with gap junction blocker BGA (n=2 cultures), the number of astrocytes with spontaneous calcium events during imaging decreases relative to the vehicle control (n=3 cultures). We quantified this effect by calculating the relative difference in number of astrocytes with spontaneous calcium transients between before and after BGA treatment. We measured a negative value in the fractional change in number of astrocytes with spontaneous calcium transients for BGA treatment, and no significant relative difference for vehicle control (Fig. 3.2b). This indicates that astrocytic gap junctions play an important role in network signaling.

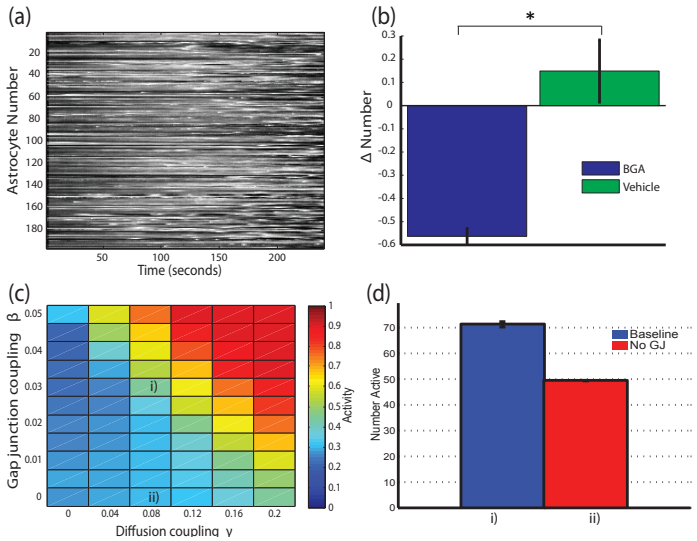

Figure 3.2: Cultured astrocyte networks display spontaneous calcium transients mediated through gap junction (GJ) coupling - (a) Example raster plot of spontaneous astrocyte network activity. Florescence intensity is rescaled between 0 and 1, where maximum intensity(1) is white and minimum intensity(0) is black. (b) The number of astrocytes with spontaneous calcium transients is dependent upon gap junction coupling in the network. Gap junction blocker BGA decreases the number of astrocytes with spontaneous calcium transients relative to the vehicle control (p-value=0.027). $\Delta Number$ is the relative difference, $(N_{after} - N_{before})/(N_{after} + N_{before})$, in the number of transients for BGA (n=2) or vehicle treatments (n=3). (c) Simulated astrocyte network shows similar dependence on gap junction coupling strength. For decreasing gap junction coupling, activity decreases across various diffusion coupling strengths. Color bar defines activity as the (avg.# of activations * refractory period) / (total simulation length). (refractory period=1000). (d) Example simulation for parameters in regions i) and ii) of (c) shows decreased activity for weaker gap junction coupling. The number of active cells is given for within 100 timesteps at point i) and ii) in (c).

Similarly, we lowered the conductance of gap junction coupling, β, in our model. The simulated astrocyte network shows a decrease in activity for weaker gap junction coupling parameter values (Fig. 3.2c). Figure 3.2c depicts the activity of astrocytic calcium events as a function of both gap junction coupling and the interaction strength between the extracellular signaling in astrocytes. In the presence of local gap junction coupling the astrocytic activity scales monotonically with strength of β. Thus, in this case, weakening gap junctions always results in decrease of astrocytic activity independent of extracellular signaling strength, except for the γ=0 case. For more discussion on parameter regimes see citation *Maruyama 2014* [58]. Figure 3.2d shows an example of the number of active cells within 100 time-steps for parameters in regions (i) and (ii) of Figure 3.2c. These parameter regions (i) and (ii) will be used for all examples in the following figures.

3.3.2 Spatial properties of astrocyte transients

After weakening gap junction coupling in the astrocyte network, in addition to fewer astrocytes with spontaneous calcium transients, we also observed significant changes in the distribution of active cells in cultures. The spatial distribution of the remaining active astrocytes stopped being uniform, and instead formed locally clustered domains (Figs. 3.3a and 3.3b). To quantify this effect we defined the clustering measure C, eqn. 3.2, as a fractional change of Euclidian distance between locations of observed active astrocytes and the randomized ones. Higher values of spatial clustering, C, indicate that more clustered groups of astrocytes were active. We observed that for control conditions the spatial distribution of active astrocytes is only minimally different from randomized locations, indicating only a small propensity for clustering. However, the spatial clustering increased significantly when cultures were treated with BGA. This effect is again not present for the vehicle control (Fig. 3.3e). This indicates that blocking gap junction greatly diminishes one mode of cou-

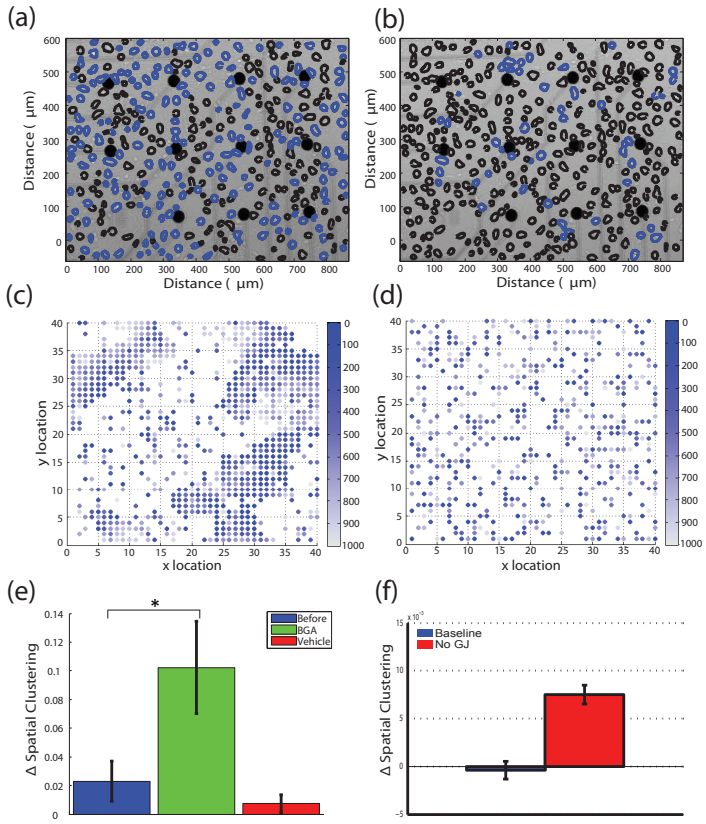

Figure 3.3: Decoupling gap junctions reveals underlying spatial clustering within astrocyte networks - (a,b) Example bright-field image of a cultured network before (a) and after (b) BGA treatment. Spatial locations of astrocytes are outlined, where blue regions displayed calcium transients during the experiment and black regions had no spontaneous activity. (c,d) Simulated astrocyte networks have similar spatial clustering before (c) and after (d) gap junction coupling. Color indicates the number of timesteps from the most recent activation. (e) Disruption of gap junction coupling with BGA enhances spatially clustering of astrocyte network activity (p-value=0.05). $\Delta\, Spatial\, Clustering$ is the relative difference in spatial clustering between experimental and random networks of the same spatial locations (3.2). (f) Simulated astrocyte network producing similar spatial clustering. Relative difference in nearest neighbor distance is measured as $(D_{random} - D_{real})/(D_{random} + D_{real})$.

pling, leaving the other still intact. The higher clustering value in the absence of gap junctions indicates that communication is still occurring, and that the remaining coupling is effectively highly clustered (short range). We hypothesize that the remaining coupling mechanism is linked to extracellular signaling and diffusion transport. To support this hypothesis we conducted similar in silico experiments using the developed model. Analogous to the experimental results, we observe that in networks with strong gap junction coupling large numbers of cells activate, forming randomly distributed activity domains (Fig. 3.3c). Spatial randomization of active sites yields no measurable effect in this case. However, when the network coupling is lowered, the large domains do not form and we observe formation of small clusters of active cells (Fig. 3.3d) with high spatial clustering. These observations are summarized on Fig. 3.3f.

3.3.3 Temporal properties of astrocyte transients

We also wanted to investigate what effect network coupling can have on the shape of calcium signaling in an individual astrocyte. Gap junction coupling being a bi-directional coupling rapidly equilibrates the Ca^{2+} levels among the coupled cells. Assuming that a given amount of calcium is released from the ER into the cytosol during the calcium event, the duration of event and the time evolution of the event may be strongly depend on the gap junction strength.

We measured the time course of calcium responses of individual astrocytes in the absence and in the presence of gap junctions coupling in both experiments and simulations(Fig. 3.4). Our simulations indicated that the duration of elevated calcium (the width of the calcium event) is strongly dependent on both the strength of gap junctions and the efficacy of extracellular signaling (Fig. 3.4F). For low β and low γ (strength of effect of extracellular signal on an individual astrocyte) the width of the calcium event initially decreases as gap junction coupling grows because of the

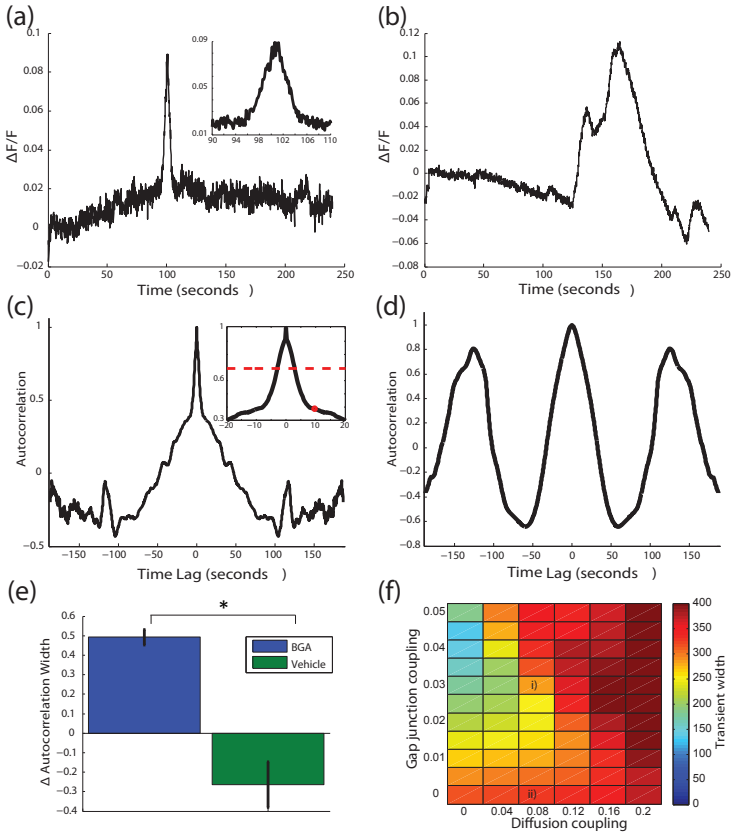

Figure 3.4: Weakening network wide gap junction coupling affects the timescale of calcium transients in individual astrocytes - (a,b) Example calcium transients of an astrocyte shown as the change in calcium fluorescence intensity over baseline fluorescence (ΔF/F) before (a) and after (b) treatment with BGA. (c,d) Corresponding autocorrelation of the fluorescence trace. Insets are zoomed in to show timescale. Red dot marks the first local minimum of the slope of the autocorrelation (see methods 3.2.2) and the dashed red line marks the half maximum. (e) An increase in the width of the autocorrelation at half maximum shows an increased duration of calcium transient after BGA (p-value=0.02). $\Delta Autocorrelation\,width$ is the relative difference, $(W_{after} - W_{before})/(W_{after} + W_{before})$, in transient width for BGA or vehicle treatments. (f) Simulated astrocyte network shows similar timescale of calcium transients. Weaker gap junction coupling (ii) has increased transient width than stronger gap junction coupling (i). Color bar represents the width of the transient in number of time steps.

equilibration effect discussed above. For strong β and even lower γ, however, we observe broadening of the event width. This is due to the fact that the extracellular signaling lowers the calcium gradient, allowing the intracellular Ca^{2+} level to remain elevated. For high values of γ, on the other hand, the change of event width is largely independent of β. This is due to the fact that extracellular transport dominates network dynamics raising the resting calcium concentrations away from the original value.

Similarly, we investigated the time course of single astrocytic calcium events experimentally. Figure 3.4a and 3.4b shows an example of astrocyte calcium fluorescence transients before and after weakening gap junction coupling in the astrocyte network. We find that the duration of astrocyte calcium transients increases after BGA treatment. To quantify the change in timescale of calcium events, we computed the width of the autocorrelation of fluorescence signal of every astrocyte Ca^{2+} event (see Methods) as a measure for the time duration of calcium fluctuations in astrocytes (Fig. 3.4c,d). We find a significant increase in the width of the autocorrelation after decoupling gap junctions with BGA, seen as an increase in the fractional change compared to control (Figure 3.4e). We also plot the change of the calcium event time course for the vehicle, but here we do not observe significant change. These results are consistent with our simulations for relatively weak gap junction and extracellular coupling, possibly providing constraints on the biological values of the coupling parameters.

3.3.4 Propagation of activity in astrocyte networks

Finally, we wanted to disambiguate the role of both coupling mechanisms in mediating the formation of temporal correlations between the astrocytes. To study the network level spatio-temporal patterning of spontaneous calcium activity in cultured astrocyte networks, we measured the correlation of calcium events as a function of spatial distance between the cells, when gap junctions are left intact and when they

are disrupted by BGA (Fig. 3.5). We plot an example of evolution of the cross correlation (CC) as a function of time lag for all astrocyte pairs falling into given distance ranges. Fig. 3.5a depicts an example control condition, while Fig. 3.5b shows an example BGA treated culture. We observe a significant change in the shape of the CC at all distances. For the controls there tends to be a peak in CC at relatively small lag. The lag increases significantly for cells that are located at a greater distance from each other. For the BGA treated astrocytes the peak of cross correlations is significantly shifted at all distances. However, notably there is not a big difference in the magnitude of cross correlation. These results are summarized over all cultures in Fig. 3.5e. We see that the lag values at which maximal CC is observed are significantly larger for the BGA treated cultures as compared to controls and vehicle treatment. It is interesting to note that the changes in the lag within the treatment group are only observed at shortest distances ($r < 50$ and $50 < r < 150$). The lags at which maximum CC occurs are not significantly changing for longer distances between astrocytes. This is probably due to intrinsic timescales connected with calcium events of individual astrocytes.

We observe very similar effects in our simulations. When gap junctions are present we observe much smaller lags at which maximal CC occurs (Fig. 3.5c). Lowering β, on the other hand, leads to much larger lags (Fig. 3.5d and Fig. 3.5f) that stabilize at larger cell distances (cell distances are calculated here in terms of lattice length). At the same time however we also observe significant decreases in the cross correlation amplitudes. This is a considerable departure from our experimental findings. This might indicate that the extracellular coupling is stronger than we assumed in the model.

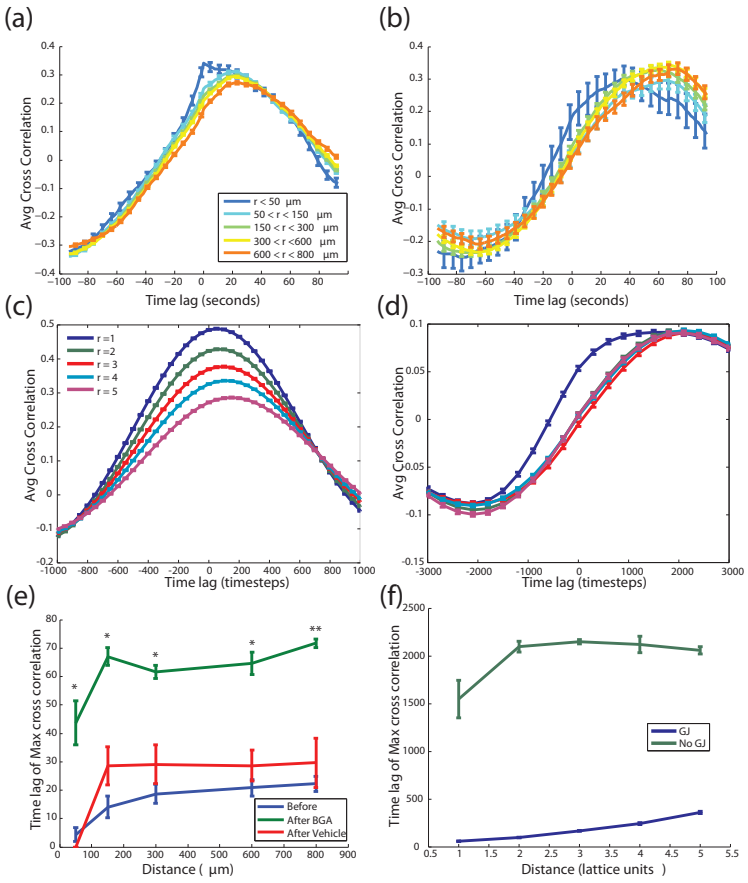

Figure 3.5: Spatio-temporal correlations between pairs of astrocyte calcium transients are mediated by gap junction communication - (a,b) Example cross correlations of calcium transients between all pairs of astrocytes within the network before (a) and after (b) BGA treatment across distances between all pairs of astrocytes. (c,d) Simulation results for cross correlations of calcium transients before(c) and after blocking gap junctions. Time lags are in number of time steps. (e,f) Maximum cross correlation between pairs of astrocytes occurs at longer time lags as a function of distance between pairs of astrocytes for both experiments (e) and simulations (f). Weakening gap junction coupling with BGA increased the time lag for maximum cross correlation across distances (r = 50, 150, 300, 600, and 800 μm) between all pairs of astrocytes (p-values=0.03, 0.03, 0.04, 0.02, 0.01, respectively).

3.4 Discussion

To gain insight into the mechanisms mediating pattern formation in astrocyte networks, we experimentally monitored astrocytic Ca^{2+} activity in mixed culture settings. We have also created a computational model that takes into account two major types of signaling pathways in astrocytes: transport through astrocytic gap junction coupling and diffusion in extracellular space. In terms of experiments, we perturbed the first pathway by blocking gap junctions using BGA. The extracellular pathway, on the other hand, is mediated by a host of signaling molecules, and therefore we were not able to successfully regulate it. We quantified the number of spontaneously active astrocyte cells, spatial clustering, temporal duration of calcium transients, and the dependence of temporal signal correlations on the spatial distance between cells. We show that the experimentally observed changes after the BGA treatment agree with our modeling results, lending credence to the hypothesis that both of these types of signaling pathways play an important role in network signaling. Furthermore, changes in the spatio-temporal patterning observed in our model when we were changing the relative coupling strength of both mechanisms provide general constraints on the biological values of these parameters.

Several experimental studies have addressed the properties of calcium signaling in astrocytes and have controversial findings. Wave propagation has been observed in both cultured cell preparations[79;80;83] and in slices[81;82], while localized synchronous calcium transients have been reported in vivo[49]. To reconcile these conflicting observations, we suggest that the spatio-temporal propagation patterns could arise out of the network properties in different dynamic regimes. Therefore, we chose to study simplified networks and investigate the modes of astrocyte coupling and resulting pattern formation in network activity. Moreover, astrocyte network communication and its interactions with neuronal network activity is poorly understood. Recent work has begun to investigate astrocyte network responses to neuronal activity[94], and how

astrocyte calcium signaling can affect neuronal synchrony[95]. However, further studies need to test whether, and to what extent, changes in astrocytic spatio-temporal activity patterns affect activity patterns of neurons, and subsequently the involvement of astrocytes in cognitive functions of the brain. Additionally, there is experimental evidence linking astrocytic activity to several brain wide pathologies[96;97;98;99].

The work in this chapter is one of the first to model astrocyte networks. In doing this we identify the relative importance of known biological pathways in contributing to interactions in astrocyte dynamics.

CHAPTER IV

Functional connectivity from time series data

In this chapter I extend Sarah Feldt and Michal Zochowski's 2010 article which first introduced average minimal distance (AMD) in the context of the functional clustering algorithm. The approach I created greatly sped up the AMD metric by replacing the bootstrapping with a faster analytic approach. Additionally, using the observed spike trains and analytically calculating the expected values doesn't rely on any outside parameters like jitter size. Most importantly, the fast-calculation of functional connectivity matrices is used as the starting point to measure functional network similarity as a function of time. In this chapter I include original derivations for several analytic approaches of expected AMD values. I also derive and interpret the performance of the AMD in the presence of noise. Finally, I examine the robustness of stability with respect to the statistics of spike trains, and discuss briefly its applications.

4.1 From theoretical neuroscience to time series

The dynamics regulating individual neurons has been understood reasonably well since the work of Hodgkin-Huxley[4]. Understanding the basic unit of the brain was correctly heralded as a major accomplishment. Yet, even after this discovery many mysteries of the brain remain unsolved. Over time it has become clear that brain function largely results from emergent dynamics in structured collections of neurons.

Neurons themselves are well described by two states, quiescent and firing, meaning that information is likely stored by specific patterns of neuronal firing[100]. One can imagine neuronal circuits which, under precise actions or thoughts, activate a fairly explicit subset of neurons. The notion of input being selectively filtered through circuits in a massively connected cortex to reach a desired output is a concept that has long been proposed[16] and has seen success recently[101;102]. This prominent theory suggests that the connections between cells account for the adaptability of neurons to stimulus. Adaptability is closely related to learning and memory, which comprise two of the core concepts in neuroscience[103;104].

Although this theory is well founded and potentially answers many questions within the field, it has been difficult to test directly. Since it is known that there are $\sim 10^{11}$ neurons each with $\sim 10^3$ connections one of the major roadblocks to this theory is the daunting task of trying to map the connections between neurons. Even if every connection could be identified, it is not clear that many individual circuits could be mapped. A circuit branching 10^3 times per unit is quite different from the circuits we usually encounter.

Another problem with testing this theory is that modern experimental measures are largely unable to directly identify the strength of connections between neurons. State of the art measurements resolve spiking behavior and are limited to electrical or optical readouts from 10-1000 cells. Measuring individual neuron spiking behavior provides raw activity data at the level of multiple cells. Electrical readouts from multi-wire set-ups, stereotrodes, or Multi-electrode Arrays (MEAs) offer a potential means of scaling up data acquisition in the future[105].

The physical basis of detecting electrical activity in neurons comes from measuring voltage changes due to action potentials. As electrodes pick up the signature of action potentials in a cell, they are mostly unable to resolve sub-threshold voltages within the cell. Collectively, these limitations on data acquisition mean that the current form

of data, which provide both high cell counts and accurate descriptions of dynamics, comes in the form of time series of neuron spiking behavior for neurons situated close to electrode readouts.

A best-effort attempt to unravel the relationship between cells can begin with trying to understand the correlations in neuron spiking data. Once you can accurately identify the relationships between cells based upon their firing behavior, attention can be shifted back to the specifics of how information is stored in the brain.

Although information is passed via anatomical connections, namely through synapses from neuron to neuron, limited experimental data streams currently make functional relationships more tractable. A functional connection describes two neurons which fire at similar times; these neurons can be thought of as both responding to the same functional stimulus. Just like anatomical connectivity, two neurons can have functional connections of varying strengths[106]. A positive functional connectivity denotes that they tend to fire together, while a negative connectivity indicates that they tend to fire at different times. As we begin to analyzing the correlation between time series it is important to remember that correlations may occasionally represent anatomical connections, and they always represent functional connections between the cells. So while memories are believed to be stored physically in the synapses[100], they manifest the observed voltage patterns of neurons which are captured by the firing behavior of the cells. Functional connectivity should therefore be able to capture, at some level, the changes occurring at the synaptic scale.

4.1.1 How do you measure the correlation between time series?

What makes two time series similar? What makes two time series different? The first question is conceptually simpler than the second as similar spike trains look alike, Fig.4.1(a), so when one train spikes the other should spike nearby as well[107]. The second question is more difficult because spike trains can be non-similar in several

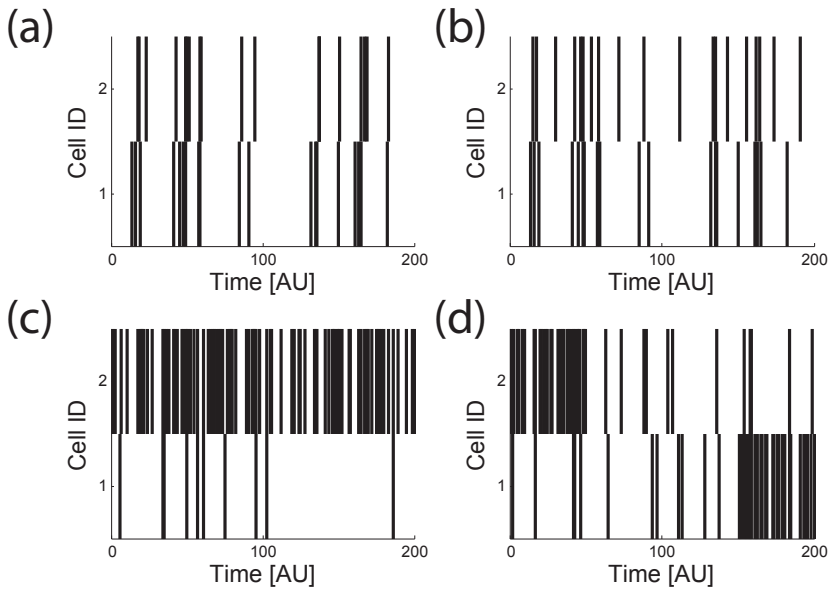

Figure 4.1: Comparing time series - (a) Similar time series, (b) Non-similar phase locked time series, (c) Time series with distinct rates, (d) Nonsimilar bursting time series.

ways, Fig. 4.1(b-d). Time series which lock out of phase are quite different. A time series with many events is quite different from one with few events. They can also be different if bursts of spikes occur in distinct locations. While all three of these examples are distinct, the degree to which these time series differ is not always clear. Occasionally it is okay to eyeball time series to see how related they are, but in order to assess the similarity between each pair of neurons a measure is needed to do the job quickly. Time series are important aspects of many lines of work so measures already exist which can help us determine correlation. Although widely used measures all detect some aspect of correlation, they have varying shortcomings as well[108]. Two of the most glaring shortcomings involve accounting for frequency and having a threshold at which correlation can be deemed significant.

4.1.2 Ways of comparing time series

Let us take a quick look at some common measures of correlation between time series. Cross correlation provides a measure of how well two signals vary about their means together. It can be applied to neuronal time series after convolving the event times with a Gaussian. When calculating cross correlation, the variable width of the convolving curve controls the range over which events are considered to be co-varying or distinct. Mean phase coherence (MPC)[109;71] quantifies the extent of phase locking[110] between time series. The relative phases of events, $e^{i\phi}$, are averaged in the complex plane to indicate locking behavior. Granger causality[111] uses the event history of one time series to try to explain the events of the other time series.

All of the methods mentioned fail to natively define thresholds for significance[112]. Often the way in which significance is found is by comparing against generated or shuffled data to empirically generate distributions of non-correlated data.

4.2 Temporal distance between spike trains

One concept that is lacking in the above methods is explicitly using the temporal difference between events to define similarity. We can define a similarity by averaging the temporal closeness of spikes from one spike train to another. The average temporal closeness of spikes between spike trains also effectively quantifies the non-similar spike trains in Fig. 4.1. By building upon this notion of average temporal distance between spikes we can define a measure called Average Minimum Distance (AMD)[113] from spike train i to spike train j as

$$AMD_{ij} = \frac{1}{N_i} \sum_{k=1}^{n} \Delta t_{ij}^{k} \tag{4.1}$$

Where Δt_{ij}^{k} refers to the absolute value of the minimum distance between spike k in train i and the nearest spike in train j. Note that AMD_{ij} is not a symmetric measure,

which is desirable when evaluating neurons which form directional connections. Using equation 4.1, we see that AMD tells us that the spike trains in Fig.4.1, which burst in distant locations, are the most different since this configuration provides the greatest average distance between the spikes.

Average Minimum Distance needs further modification to be a sufficient spike train measure, as it fails to account for the expected distance between the spike trains. Without this modification frequency is not considered and the temporal distances are difficult to interpret.

4.2.1 Comparing to generated distributions: Jitter and exponential distributions

One way to control for frequency is to use Monte Carlo methods[114;115] to sample the distribution of potential spike trains and compare how the observed distance stacks up to the distribution of sampled distances. This is the idea behind the original iteration of AMD used in detecting functional connections with the Functional Clustering Algorithm (FCA)[41]. The FCA jitters the time of events in all spike trains, S_i, and recalculates the AMD between spike trains. After jittering a large number of times ($\sim 1000 - 10000$) an expected distribution of AMDs emerges for each pair of spike trains. The significance of each observed, unjittered, AMD_{ij} can be found by comparing to the jittered distribution. This can be accomplished by normalizing the AMD values with a t-test.

$$\widehat{FC}_{ij} = \frac{\mu_j - AMD_{ij}}{\sigma_j/\sqrt{N_i}} \tag{4.2}$$

Here $\widehat{FC}_{ij}$ refers to the estimate of the functional connectivity between neuron i and neuron j. μ_j, σ_j correspond to the jittered AMD mean, and jittered AMD standard deviation respectively. The size of the jitter used to shake spikes is a free parameter of the FCA, which provides the flexibility to destroy correlation on specified temporal scales.

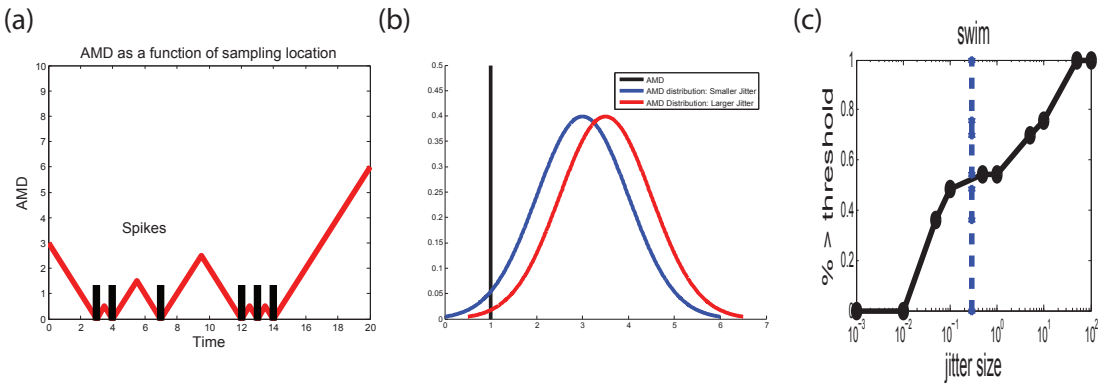

Figure 4.2: Comparing AMD against jittered distributions - (a) Black lines denote events in S_j, while the red line denotes the minimum distance as a function of sampling location. Average Minimum Distance (AMD_{ij}) is obtained by sampling the red line at spiking locations S_i and averaging. FC_{ij} is obtained by plugging into 4.2. (b) To demonstrate this, if the black line is the measured AMD_{ij}, then for different sizes of jitter, red or blue, you get a distribution whose mean and standard deviation are $\mu_j, \frac{\sigma_j}{\sqrt{N_i}}$ respectively. (c) Shows the number of clustering steps above the cutoff threshold as a function of jitter size. Jitter controls the extent of the correlations you destroy, as it grows correlations are disrupted on larger scales.

One downside of repeatedly jittering spikes to generate a distribution of non-correlated AMD values is how long it takes. Each AMD calculation for jittered spike trains takes just as long as the initial AMD calculation. This leads to long computation times to compute functional connectivities for relatively small data sets ($\sim 1Mb$). Calculating the jittered AMD values can be avoided by making various assumptions. If you want to compare the measured AMDs to the distance you would expect if train j was completely uncorrelated you could compare to the expected AMD of a randomly generated spike train with an equal number of events. Unfortnuately, any single instance of a randomly generated spike train may have a large or small Average Minimal Distance. Instead, you want to compare the measured AMD against the expected value of all possible realizations from that distribution.

One of the simplest ways to do this is to multiply the expected AMD values on intervals of given sizes by the probability of sampling an interval of that size, and then integrate over all interval sizes, $< AMD_j >= \int_l < AMD >_l * P_S(l)$. This equation

depends on j only through $P_S(l)$ which accounts for the rate of spikes, $\lambda = \frac{N}{T}$, in S_j. In order to perform this calculation it is helpful to remember that interspike interval lengths of Poisson process spike trains are equal to the waiting times between successive events, and therefore follow an exponential distributions, $P(l) = \lambda e^{-\lambda l}$. Additionally, if the total data period is T, the probability of sampling on a given interval of length l is $p(l) = \frac{l}{T}$. For Δt_{ij}^k, defined in eqn 4.1 as the minimum distance between event k in S_i and S_j, an interval of length l has an expected AMD of $\frac{l}{4}$.

$$< AMD_j >= \mu_j = \int_l < AMD >_l * P_S(l) = \int_l \frac{l}{4} * P_S(l) \tag{4.3}$$

To find $P_S(l)$ we use the probability of sampling an interval of length l, and the distribution of intervals of length l. Enforcing the normalization constraint on the distribution we have,

$$1 = \int_l P_S(l) \tag{4.4}$$

$$1 = \int_l C * \frac{l}{T} * \lambda e^{-\lambda l}\, dl \tag{4.5}$$

$$1 = \frac{C}{T}\lambda \left(\int_0^\infty l\, e^{-\lambda l}\, dl \right) \tag{4.6}$$

$$1 = \frac{C}{T}\lambda \left(\frac{1}{\lambda^2} \right) \tag{4.7}$$

$$C = \lambda T \tag{4.8}$$

$$P_S(l) = \lambda^2 l\, e^{-\lambda l} \tag{4.9}$$

Plugging into eqn 4.3 gives,

$$< AMD_j > = \int_l \frac{l}{4} \lambda^2 \, l \, e^{-\lambda l} \tag{4.10}$$

$$= \frac{\lambda^2}{4} \int_l l^2 e^{-\lambda l} \, dl \tag{4.11}$$

$$= \frac{\lambda^2}{4} (2\lambda^2) \tag{4.12}$$

$$< AMD_j > = \frac{1}{2\lambda} = \frac{T}{2N} \tag{4.13}$$

This tells us that the expected AMD of a random spike train with rate λ is two times the expected distance of a uniform distribution.

Similarly, we can calculate $< AMD_j^2 >$ following the methods above $< AMD_j^2 >= \int_l < AMD^2 >_l * P_S(l)$. We will skip showing the work here and list the value instead $< AMD_j^2 >= \frac{3}{8\lambda^2}$. Knowing that $\sigma^2 =< x^2 > - < x >^2$, we can find the variance of $< AMD_j >$ to be $\sigma_j^2 = \frac{1}{2\lambda^2} = \frac{\mu_j^2}{2}$. Plugging (μ_j, σ_j) into equation 4.2 estimates the functional connectivity as the significance of the actual distance compared to a fully randomized distribution. This value reflects the information stored between S_i and S_j.

For spike trains which are approximately random, this normalization works well. Unfortunately, most spike trains have ISI distributions which are not random, and in this case the approximation can fail quite badly. To demonstrate this failure we will imagine three spike distributions which all contain the same number of spikes: S_1 will have uniformly spaced spikes, S_2 will be randomly generated with rate λ, and S_3 will be a burst of spikes. If we take the number of spikes to be N, and the duration of the data to be T, then the distance from S_3 to S_1 in the worst case is $\frac{T}{2(N+1)}$. Comparing this to the expected distance on a randomly generated spike train we have $\mu_j = \frac{T}{2N}$, from 4.13 . This shows us that using the expected distance from a random distribution as the reference to compare against the real distance from a

uniformly distributed spike train will always yield a positive functional connectivity. This happens because a uniform distribution minimizes the variation in ISI size, and is therefore the distribution that minimizes the expected value of AMD. Similarly, if we find the distance from S_1 to S_3, we should expect the value to lie around the interval $[\frac{T}{4}, \frac{T}{2}]$, which is larger than the expected value $\mu_j = \frac{T}{2N}$. Given the inability of assumed ISI distributions to reflect the observed spike train ISIs a more accurate estimate of expected AMD distance can made by using the observed ISI distribution

4.2.2 Comparing to the expected AMD distributions

The problem with comparing the actual AMD to the expected AMD of any *a-priori* distribution is that each distance AMD_{ij} reflects the average minimum distance from spikes in S_i to spikes in S_j. Therefore, it makes the most sense to compare against the expected AMD_j distribution of S_j. Fig. 4.3(a) shows how you can calculate the expected value of the red line over the spike distribution. The first step is to break down the desired integrals into values on interspike intervals. For spike train data coming from the interval [0, L], consider breaking it into segments around the n events at locations l_i, where $l_0 = 0$ and $l_n = L$.

$$< f > = \frac{1}{L} \int_0^L f(x)\, dx \tag{4.14}$$

$$= \frac{1}{L} \sum_{i=1}^{n} \left(\int_{l_{i-1}}^{l_i} f(x)\, dx \right) \tag{4.15}$$

$$= \frac{1}{L} \sum_{i=1}^{n} (l_i - l_{i-1})\, \bar{f}_i \tag{4.16}$$

$$= \sum_{i=1}^{n} P_i\, \bar{f}_i \tag{4.17}$$

In equation 4.16, $\bar{f}_i$ is defined as the average of f on the interval $[l_{i-1}, l_i]$, so $\bar{f} = \frac{1}{l_i - l_{i-1}} \int_{l_{i-1}}^{l_i} f(x)\, dx$. In 4.17, $P_i = \frac{l_i - l_{i-1}}{L}$ is the probability of that interval being

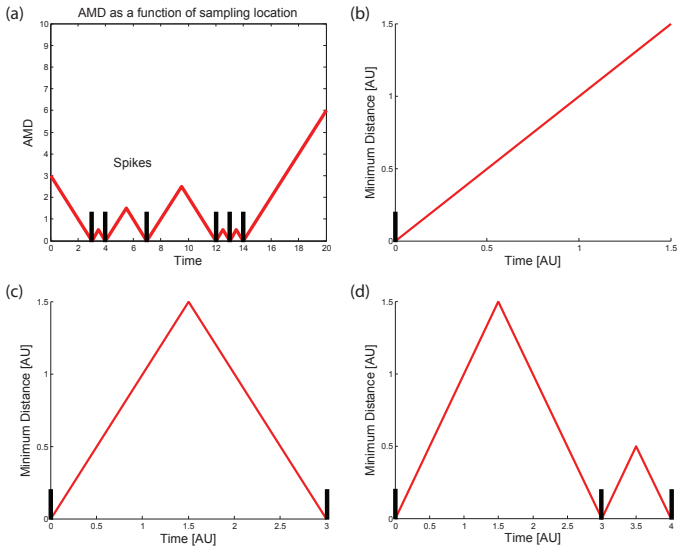

Figure 4.3: How to calculate AMD - (a) The expected minimum distance, average of the red line, can be found by evaluating it on smaller components before reconstructing it, b-d. (b) Start by evaluating the expected value of AMD on half an interval. (c) Then use symmetry to reconstruct the average on a full interval. (d) Lastly, combine intervals to create the distribution in (a).

randomly chosen. Following the process outlined in equation 4.3 we are simplifying equation 4.17, by breaking it into the average value on each ISI and multiplying by the probability of sampling that ISI.

Next, we can use symmetry to break down the expected AMD into identical components on each half ISI interval. This is depicted in Fig. 4.3 panels (b-d). The last step is to integrate the first and second AMD moments, then combine them by noting that the probability of sampling a specific interval is directly proportional to the length of that interval as depicted in equation 4.17.

As we see in panel (b), for an interval of length x, the average distance from the

left side of the interval is

$$< AMD(x) > = \frac{1}{x} \int_0^x y \, dy \tag{4.18}$$

$$= \frac{1}{x} \frac{x^2}{2} \tag{4.19}$$

$$= \frac{x}{2} \tag{4.20}$$

From symmetry we see the average is same on both halves, shown in panel (c). Substituting $x = \frac{l_i - l_{i-1}}{2}$, the expeced value on an interval of length L is

$$\overline{AMD}_i = \frac{l_i - l_{i-1}}{4} \tag{4.21}$$

Using 4.17, we can calculate the expected value of AMD on spike train j as

$$< AMD_j > = \sum_{i=1}^{n} P_i \, \overline{AMD}_i \tag{4.22}$$

$$= \sum_{i=1}^{n} \frac{l_i - l_{i-1}}{L} \frac{l_i - l_{i-1}}{4} \tag{4.23}$$

$$= \sum_{i=1}^{n} \frac{(l_i - l_{i-1})^2}{4L} \tag{4.24}$$

$$= \sum_{i=1}^{n} \frac{{\Delta l_i}^2}{4L} \qquad where \; \Delta l_i = l_i - l_{i-1} \tag{4.25}$$

Repeating this process we can find $< {AMD^2}_j >$,

$$< AMD^2(x) > = \frac{1}{x} \int_0^x y^2 \, dy \tag{4.26}$$

$$= \frac{1}{x} \frac{x^3}{3} \tag{4.27}$$

$$= \frac{x^2}{3} \tag{4.28}$$

for $x = \frac{\Delta l_i = l_{i-1}}{2}$ this gives

$$\overline{AMD^2}_i = \frac{{\Delta l_i}^2}{12} \tag{4.29}$$

which gives

$$< {AMD^2}_j > = \sum_{i=1}^{n} P_i \, \overline{AMD^2}_i \tag{4.30}$$

$$= \sum_{i=1}^{n} \frac{{\Delta l_i}^3}{12L} \tag{4.31}$$

From equations 4.25 and 4.31, we have $< AMD_j >= \mu_j = \sum_{i=1}^{n} \frac{{\Delta l_i}^2}{4L}$ and $< {AMD^2}_j >= \sum_{i=1}^{n} \frac{{\Delta l_i}^3}{12L}$. This allows us to quickly calculate the of each AMD_ij by plugging into the equation 4.2, reprinted below.

$$\widehat{FC}_{ij} = \frac{\mu_j - AMD_{ij}}{\sigma_j / \sqrt{N_i}}$$

This equation meets most of the initially stated demands in that it is normalized to account frequency, and that it can measure how different each of those sample cases are. Not too surprisingly it selects the bursting spike train as the times series that is the least correlated to a random spike train.

4.2.3 What is AMD measuring?

It is important to consider what equation 4.2 is measuring as well as what it is biased to detect. Consider a spike train consisting of four spikes making up two interspike intervals as depicted in Fig. 4.4. If you want to sample this minimum distance distribution at one location in order to get the largest value then you can sample it in the middle of the longest interval, at 1.5. Similarly, if you want the largest average while sampling each interval once, then you can sample each interval

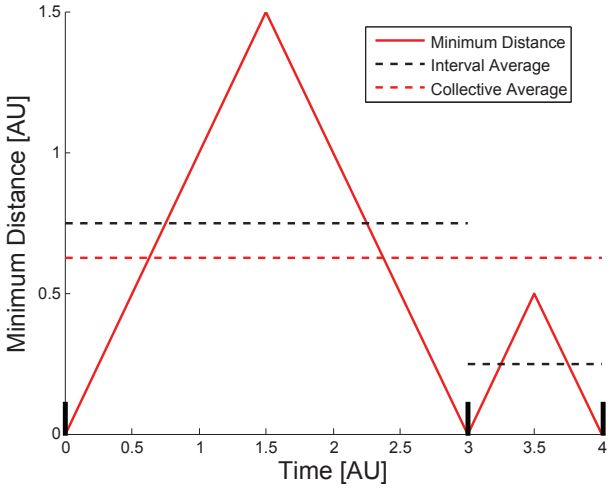

Figure 4.4: What AMD measures - Consider S_j to be the spike train in black, the red line denotes the minimum temporal distance as a function of sampling location. On a given ISI, the expected MD is denoted by the dashed black line. The overall average is represented by the dashed red line. Sampling any location on the smaller ISI, [3,4], will yield a less than average minimum distance.

directly in the middle. In this case, does the sampling location of the shorter interval matter much? We see that provided the smaller interval is a good amount shorter, the sampling location on the short interval doesn't matter as much as the longer interval because the minimum temporal differences are averaged arithmetically. To demonstrate this more clearly, if the short interval is sampled directly on one of the two interval edges and the longer interval is still sampled at the midpoint, then the combined AMD from those two samplings will be larger than the expected value making it negatively correlated.

An extension of AMD will be shown in section 4.2.5 which emphasizes the location where each interval is sampled, but as AMD is currently described, it is similar to rate coding in that it rewards sampling regions of high density. Small AMD values can be achieved either by sampling any part of a small interval or by sampling close to spikes on large intervals. This shows that AMD is similar to cross correlation, which also emphasizes that high density regions overlap.

By selecting AMD as the measure of spike train distance in equation 4.2, our approach to functional connectivity is explicitly looking for small average temporal distances. As mentioned above, sampling short intervals and sampling large intervals close to the spike both produce a positive correlation. This search for correlation is not a sign of statistical independence. Statistical dependencies do not need to be defined by short average time differences, for instance phase locking can result in large temporal distances and chaotic relationships may have non-trivial relationships between spike trains. AMD attempts to identify repetitive functional structure because spiking statistics make it unlikely to identify single spike relationships. For a strong functional relationship to be measured a consistent signal is generally need to move the mean temporal distance from the expected distance. Highly coincident spikes can also contribute to large z-scores, but fail to make much difference after averaging across many spikes. Signals that encode given functional tasks must cohere on the time scale of that functional task, often on the order of milliseconds. Given the short time constraint for highlighting a specific task and the noisy environment of the brain, we believe that correlation on the level of individual spikes should be prioritized over slower and more complex neuron relationships. Therefore, we are looking for repetitive correlations of individual spikes instead of correlations between entire spike trains. However, if one wanted to search for more complex statistical dependencies than average temporal closeness then a different functional connectivity could be identified for specified relationships.

Another limitation of AMD is related to the speed of signal transmission in neurons. The expected value of AMD on an interval of temporal length l, $\frac{l}{4}$, doesn't account for the time of signal transmission. Lets assume the slowest signal between neurons in a functional group is S, then temporal distance will fail to register functionally related events if S is on the order of $\frac{l}{4}$. Biologically, if slow signals could be on the order .1 seconds, then cells spiking consistently every .4s, or 2.5hz would

fail to be identified as positively correlated spike trains. This isn't generally a concern because AMD prioritizes rate coding and cells rarely fire uniformly over entire recording periods. Furthermore, AMPA signaling happens on a significantly faster time scale, around $\sim 0.001\text{s}$[116].

4.2.4 Extracting the signal from the noise

There is one important AMD functional connectivity concept that remains to be investigated. Synaptic input to neurons comes from many sources, and there is no reason to believe that neurons only respond to one input. Even when neurons are strongly coupled, they will fire stochastically in the presence of quiescent periods. This raises a question, does the AMD functional connectivity continue to work when cells fire in response to multiple input sources?

To answer this, let's consider the Average Minimum Distance, AMD_{ij}, between spike trains S_i and S_j. Assume that $\alpha\,\%$, $\frac{N_\alpha}{N_i}$, of the events in S_i coincide with events in S_j to functionally encode for something. The $(1-\alpha)\,\%$ of the rest of the spikes correspond to stochastic firings or to interactions with other spike trains. This is depicted in Fig. 4.5, where the functional events from S_1 to S_2, colored red, are being masked by the presence of the other spikes strains. We can represent the Minimum Distance, Δt_{ij}^k, as a combination of correlation with S_j and of independent firings. We will assume that the functional firings have a set form, where the same pathway is traced out for a repeated functional representation, so that the minimum distance will be constant, $\Delta t_{ij}^k = \bar{d_{ij}}$. Non-correlated firings will be assumed to randomly sample S_j, and can be represented as a normal random variable, $\boldsymbol{N}(\mu_j, \sigma_j)$. The following derivation can be modified to allow for encoding of multiple relationships, but the scaling should not be too impacted. Using our assigned notations and the relevance

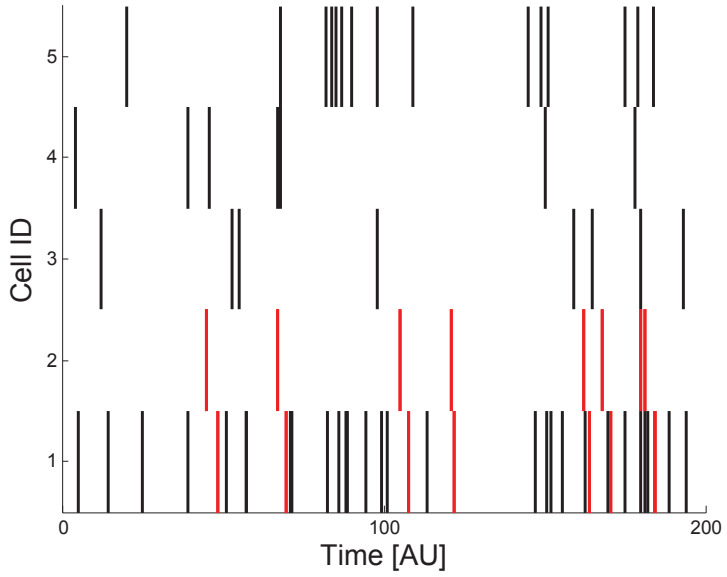

Figure 4.5: AMD signal to noise scaling - Neuron 1's raster includes responses to Neuron 2, in red, and responses to Neurons 3-5, in black.

of correlated and random spikes we represent the mean Minimum Distance as,

$$\Delta t_{ij}^{k} = \alpha\, \bar{d_{ij}} + (1-\alpha)\boldsymbol{N} \tag{4.32}$$

plugging this into equation 4.2, we estimate the functional connectivity to be

$$\widehat{FC}_{ij} = \frac{\mu_j - AMD_{ij}}{\sigma_j/\sqrt{N_i}} \tag{4.33}$$

$$= \frac{\mu_j - \frac{1}{N_i}\sum \Delta t_{ij}^{k}}{\sigma_j/\sqrt{N_i}} \tag{4.34}$$

$$= \frac{\mu_j - \frac{1}{N_i}\sum (\alpha\, \bar{d_{ij}} + (1-\alpha)\boldsymbol{N})}{\sigma_j/\sqrt{N_i}} \tag{4.35}$$

Averaging over a randomly sampled normal variable should return the mean with

variations on the order of the standard error, $\frac{1}{N}\sum \boldsymbol{N} \approx \mu_j \pm \frac{1}{\sqrt{N}}\sigma_j$.

$$\widehat{FC}_{ij} = \frac{(\alpha + (1-\alpha))\mu_j - \frac{1}{N_i}\sum(\alpha\, \bar{d_{ij}} + (1-\alpha)\boldsymbol{N})}{\sigma_j/\sqrt{N_i}} \tag{4.36}$$

$$= \frac{\alpha(\mu_j - \frac{1}{N_i}\sum \bar{d_{ij}}) + (1-\alpha)(\mu_j - \frac{1}{N_i}\sum \boldsymbol{N})}{\sigma_j/\sqrt{N_i}} \tag{4.37}$$

$$\approx \frac{\alpha(\mu_j - \bar{d_{ij}}) + (1-\alpha)(\mu_j - \mu_j \pm \frac{1}{\sqrt{N_i}}\sigma_j)}{\sigma_j/\sqrt{N_i}} \tag{4.38}$$

$$\approx \frac{\alpha(\mu_j - \bar{d_{ij}}) \pm (1-\alpha)\frac{1}{\sqrt{N_i}}\sigma_j}{\sigma_j/\sqrt{N_i}} \tag{4.39}$$

$$\approx \alpha\sqrt{N_i}\frac{(\mu_j - \bar{d_{ij}})}{\sigma_j} \pm (1-\alpha) \tag{4.40}$$

$$\approx \frac{N_\alpha}{N_i}\sqrt{N_i}\,\overline{FC}_{ij} \pm \frac{(N_i - N_\alpha)}{N_i} \tag{4.41}$$

The results of equation 4.41 are important! It tells us that the functional response between S_i, S_j is scaled by the probability of correlated events and that there is a noise term. While $(1-\alpha)$ may be greater than α, the dependence on the number of spikes is an important distinction between the two terms. The first term increases with the number of spikes, while the non-correlated term doesn't. This is consistent with the understanding that additional data should improve the signal to noise ratio. Provided a sufficient number of events are present in the spike trains, the functional signal, $\bar{d_{ij}}$ will dominate the noise.

4.2.5 Extensions of average minimal distance

Average Minimum Distance is fast, simple to interpret, and has proven robust in application. Even so, the way it rewards sampling regions of high density is sometimes unideal. As mentioned in section 4.2.3, high density regions may require a more selective measure. This can be achieved using either phase methods or variations of temporal distance with stronger emphasis on shorter distances.

Variations of AMD could use relative phase instead of the temporal distance. On

an interval of size L, the expected phase to nearest event when randomly sampled is $\frac{\pi}{2}$. Unlike AMD, where all of the distances are added and compared to the expected distance and standard deviation, each phase would be converted into a measure of significance and then combined. The end result is similar to Mean Phase Coherence, with the added benefit of knowing the context of the value returned without needing to repeatedly create randomized distributions.

This work has not yet been pursued, but I have some recommendations for the process. Computing a significance on each interval using a t-test, $phase_{ij} =< \frac{\mu_j - d_i j}{\sigma_j} >$ is not needed, and in fact if computed on each interval will return values on $[-\sqrt{3}, \sqrt{3}]$. This is problematic because it implies that no spike on a single interval can be significant according to a t-test. Instead, acknowledging that randomly distributed spikes should evenly sample an interval, we can take each phase value and compare to the phase cdf of expected values. This would suggest that the cut-off for significance of the averaged phase values,$\sqrt{N_i} * (\frac{1}{N_i} \sum_k Phase_{ij}^k - \frac{\pi}{2})$, is any value less than $\frac{1}{20}\pi$.

Instead of taking the temporal distance, an adapted measure could be pursued. For instance, a temporal distance cutoff could be added in order to apply a maximal penalty on large intervals. It is unlikely that events further apart than a certain distance reflect the relationship between the neurons. As an added benefit, this would emphasize the relationship amongst spikes over a smaller time scale. Another approach would be to use a different functional form of Δt_{ij}^k for instance, $f(\Delta t_{ij}^k) = (\Delta t_{ij}^k)^{\frac{1}{2}}$ would also place more emphasis on shorter distance by effectively scaling down the impact of larger temporal distances. An interesting way to measure functional connectivity would be mimicking expected Hebbian learning rules[28]. Given the wide variety of learning rules there are many options here, but if you adopted a $\frac{1}{x}$ rule then you would have something similar to $HL_{ij} = \sum_k \frac{1}{\Delta t_{ij}^k}$. You would still need to calculate the first and second moment of the adopted measure in order to calculate the significance. All of the suggested measures have the convenient property where

comparing to randomized distributions is unnecessary.

4.3 Returning to neuroscience: Measuring the rate of change of functional connectivity

Having built up the necessary machinery to quantify neuronal synapses, we are now ready to look at changes in neuronal functional relationships. Studying the interactions at a network level will ideally allow us to glimpse how the brain records information. Theory suggests that changes in the synapses store memories and allow learning to occur. In order to investigate this, we want to look at structure in the Functional Connectivity matrices, $\{\widehat{FC}_{ij}\}$.

4.3.1 Measuring change in connectivity matrices

One of the first ways we investigated functional connectivity was by looking at leading structure present in the functional connectivity matrices, and merging the spike trains with the strongest correlation. Recalculating the functional connectivity amongst new spike train pairs and repeating the merging process results in a recursive algorithm, called the Functional Clustering Algorithm, which highlights the most dominant structure. The result of the FCA, when combining n spike trains, is n-1 merging steps tracking which cells are being merged and the particular strength of each merging step.

This can be plotted in a nice visual form as a dendrogram, see Fig. 4.6. Dendrograms can be useful for picking up hidden structure within neuronal data as in Fig. 4.6(a). The binary nature of clustering relationships can make comparing dendrograms difficult. Two neurons may be strongly related, but interactions with other neurons may cause them to belong to distinct functional clusters.

Full matrix methods utilize all pairs of relationships and can provide more thor-

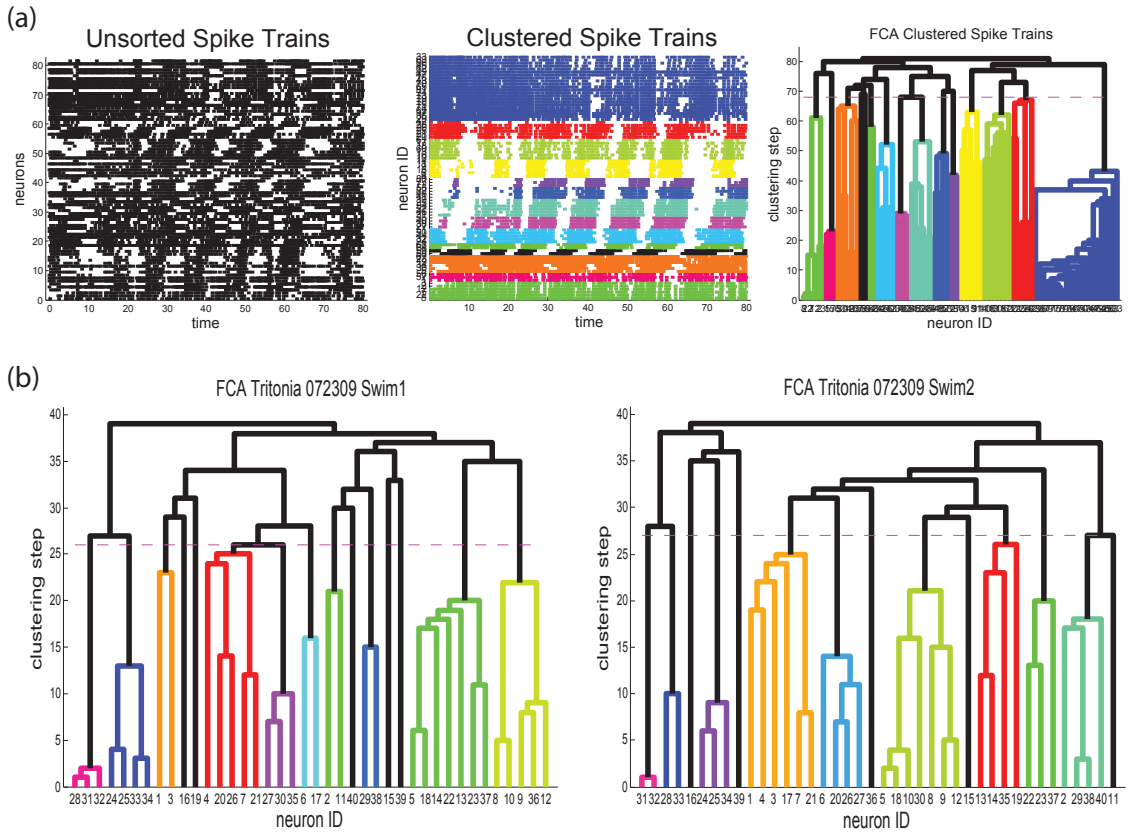

Figure 4.6: Dendrograms examples - (a) Applying FCA to the unsorted raster plots on the left gives a raster plot which visually performs well. The clustering structure is shown on the far right. (b) Comparing dendrograms can be difficult due both to the high dimensionality and the inclusion/exclusion classification of the FCA.

ough descriptions of changes in functional structure. The high dimensionality of pairwise correlation matrices, n^2 pairs, makes it difficult to visually process information about the change in each element. It is simpler to look at methods which return a single value describing the overall change. One such method is the root mean square difference (RMSD) in functional connectivity matrices. RMSD gives the sqrt of the average power in the difference matrix. It signifies the average difference in two matrices, where zero denotes no change.

4.3.2 Stability of functional connectivity

Another way to measure overall difference between functional connectivities is to think of them as vectors, and compare them with cosine similarity[117]. Cosine similarity between two vectors, depicted in Fig. 4.7(a), is the length of the projection of one normalized vector onto the other. As the name suggests it is closely related to the cosine function, $CS(\vec{x},\vec{y}) = \frac{<\vec{x},\vec{y}>}{||\vec{x}||\,||\vec{y}||}$, and it is consistent with the standard interpretation on the unit circle where the cosine of an angle is the projection of that location, specified by the angle, onto the x-axis. Cosine similarity computes a weighted combination of the overlap between all n^2 functional connections and gives a value between 1, parallel vectors, and -1, anti-parallel vectors.

Cosine similarity can be calculated for data from consecutive periods of time. We call this stability, as you expect less change in functional connectivity for more stable functional structure. Stability picks up the rate of change in the functional structure, and this can be seen in Fig. 4.7(b), where a simple four unit model is set to oscillate over time. The oscillations shift to a higher rate at time 50, which shows up as a drop in the stability. Rate of change is sensitive to both the overlap and duration of data, so care should be taken when comparing similarity between distinct data sets. The bottom of Fig. 4.7(b) shows the matrix of similarity values the results from comparing all pairs of time windows.

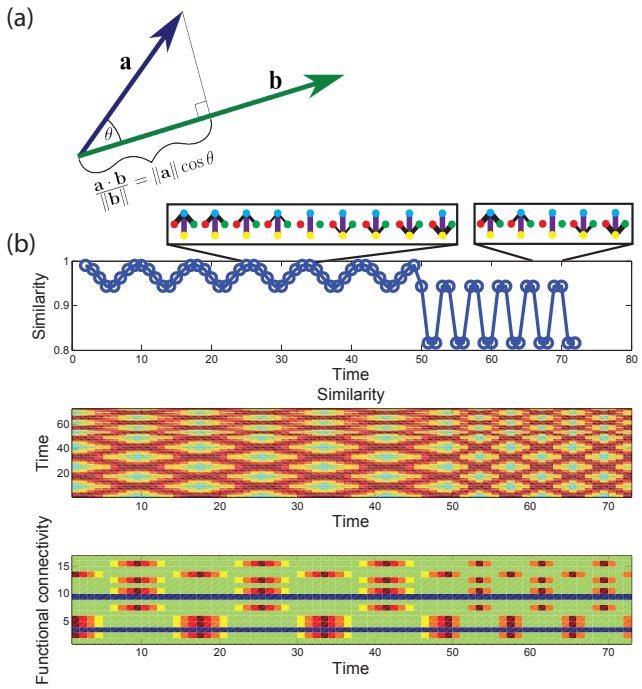

Figure 4.7: Examples of cosine similarity - (a) Shows the definition of cosine similarity, (b) Shows similarity for a simple oscillating structure.

The robustness of stability in the presence of noise merits discussion. Stability returns a measure of the rate of change of the measured functional connectivity. Ideally this structure isn't too sensitive to the exact timings of each spike, otherwise variances makes interpretation of stability difficult. Fig. 4.8 investigates stability in two situations. In panels (a,b) stability is calculated for jittered generated spike trains, and in panel (c) the spike train properties are investigated under jitter.

The simulations investigated in panel (a) consist of a randomly generated master spike train and duplicated spike trains which have a probability of copying each event in the master spike train. When events are copied, they are jittered around the time of the copied spike. In order to roughly equalize the number of spikes in the duplicated and master spike trains, random spikes are added to the duplicated trains. Panel (a) shows stability versus small jitter for several copying rates, and panel (b) shows the same for large jitter. As shown in Fig. 4.2(c), jitter size is inversely related to stability, but here we see that stability is quite robust to jitter. For all copying rates,

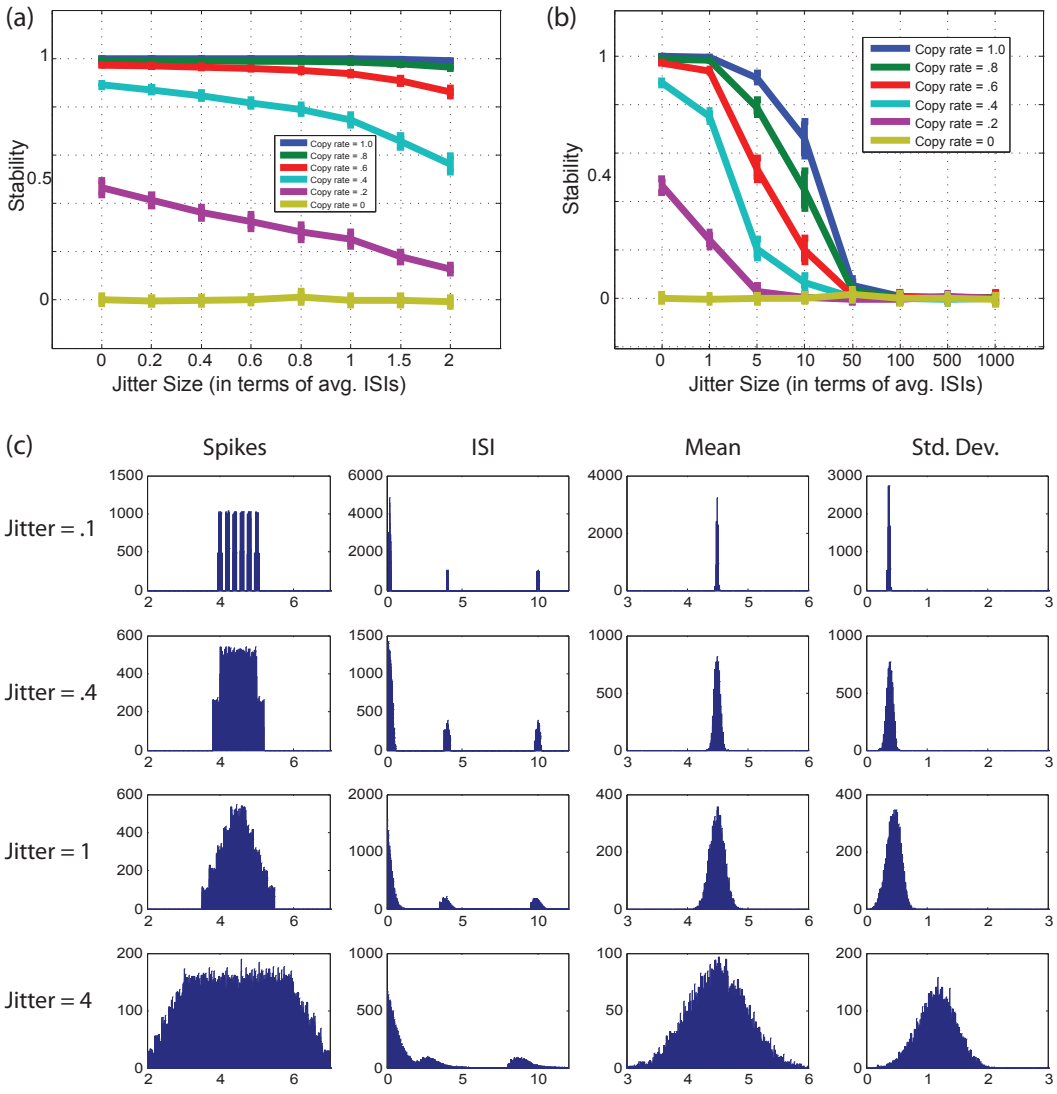

Figure 4.8: Robustness of stability to noise - (a) Shows the stability of copied spike trains to small jitter values, averaged over 6 runs. The network consisted of 1 master train and 39 copied trains. (b) Stability of copied spike trains to large jitter values. (c) Influence of jitter on Location, ISI distribution, Mean and Std Dev for a specified spike set up. The initial distribution consists of spikes at [4,4.2,4.4,4.6,4.8,5.0].

stability is easily distinguished from randomized spike trains when jitter is the size of the average ISI. Stability of highly copied spike trains is distinct even with jitter as large as 10x the average ISI.

This robustness to jitter is in part due to the rate sampling nature of AMD. The first column in panel (c) shows the impact of jitter size on a set distributions spikes, $[4, 4.2, 4.4, 4.6, 4.8, 5]$. Later columns show histograms of ISIs, variance, means, and range of the initial distribution under 10,000 jitterings. The jitter size of the rows are [.1,.4,1,4]. Notice that the average ISI size, .2, is much smaller than the jitter size in the last row, yet the mean, variance, and distribution are still similar to earlier cases. Jitter represents a mean 0 transformation; on average the spikes don't move, which means that typically over dense regions will still be over dense after jittering. Jitter must be large enough to mix over and under-dense regions, which are often larger than the scale of single ISIs. While jittering shakes each spike, the functional connectivity is strongly dependent upon region density and therefore is quite stable to perturbations.

Cosine similarity has been introduced in the context of comparing adjacent time periods in order to see how they change, but it doesn't need to be limited to neighboring periods. In fact, comparing all the partitioned data against each other is one way to look for reoccurring patterns within the data.

Fig. 4.9 shows an example of the application to data. Panel (a) depicts the functional structure of readouts from a mouse hippocampus over 24 hrs. Even at this level it is clear that there are two distinct structures present in the data because of the bands of vertical structure. Here each cell's relationships for a given data segment are stretched into a column. Neurons 1-6 appear to be largely uncorrelated to anything at the beginning, whereas neurons[7-9, 11-13] appear to be highly correlated. In the bands of vertical structure, everything seems to become more correlated as denoted by these columns having more red. Interestingly in these locations, only neuron 10

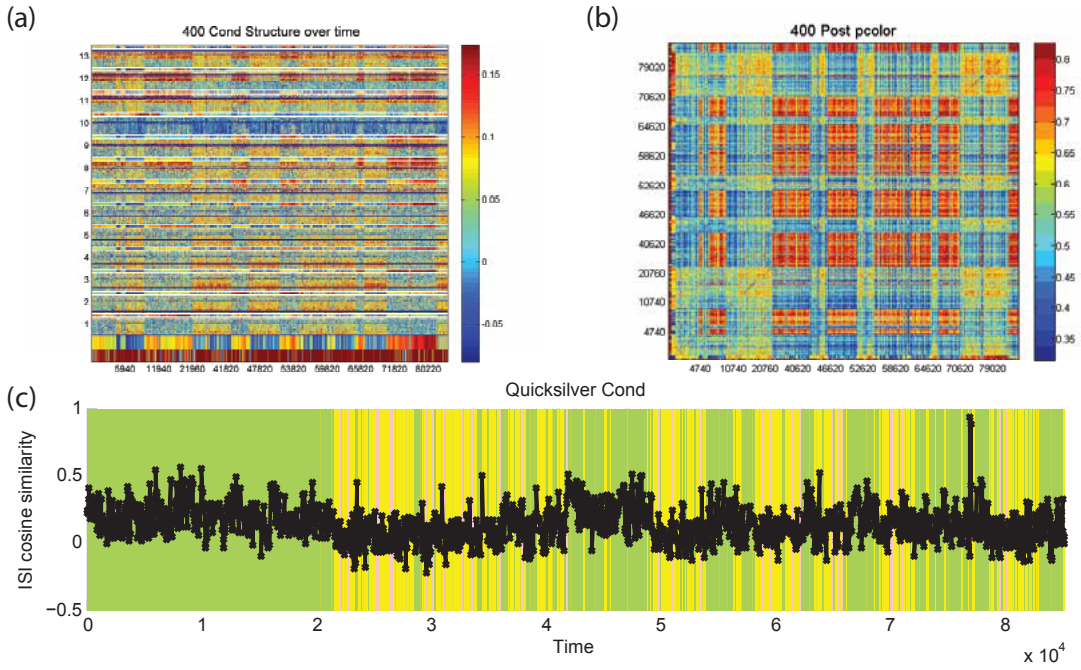

Figure 4.9: Example of identified structure over time - (a) Functional connectivity of a given moment of time is displayed as a vertical column. Color denotes the normalized strength of coupling, $\frac{\widehat{FC}_{ij}}{|\widehat{FC}|}$. A colored strip indicating cell frequency is placed inside the white border at the top of each cells functional relationships. The bottom two rows are the sleep phase and population frequency. (b) Similarity calculations for all the periods of data. (c) The similarity between adjacent data segments. The background color reflects the sleep state(green=wake, yellow=SWS, red=REM).

appears to have primarily low connectivities to the other neurons. This might suggest its connections are mostly inhibitory, possibly identifying the cell as an inhibitory fast spiking interneuron. This is potentially corroborated by noting that neuron 10 appears to have reduced connectivity to all the other cells during the bands of vertical structure. Panel (c) shows the stability when you compare data from adjacent time windows. The coloring in the background of the plot denotes the sleep phase of the animal: green denotes wake, yellow denotes slow wave sleep, and red denotes REM sleep. Panel (b) shows the similarity values which result from comparing all windows with all other windows. The two bars on the bottom and left side are the sleep phase, and the population frequency, respectively. The structure here matches the vertical bands of structure, and confirms that the periods of vertical structure represent very similar functional connectivities.

CHAPTER V

Learning-induced functional network stability as a mechanism for system memory consolidation

In this chapter I apply stability to quantify the changes in network dynamics due to rapid learning during contextual fear conditioning. In addition I show that the insertion of a network heterogeneity into a simulated network of neurons produces a measurable change in network stability. I also find that the change in network stability of sleeping mice shows good correlation with the classical measure. All experiments in this chapter were performed in Sara Aton's lab by Nicolette Ognjanovski. This chapter has been submitted for publication.

5.1 Introduction

Structural network changes, such as changes in synaptic strength between individual neurons, are thought to form the physical basis of memory traces (engrams) in the brain[118]. Such structural changes could promote memory formation and retrieval through the creation of network heterogeneities acting as dynamical attractors[119;18]. The exact nature of these attractors is unknown, and precisely localizing engrams in the brain has proven difficult. At the same time, detection of such network heterogeneities, comprising changes to a small fraction of synapses[120], presents a computa-

tional problem for the brain. In this chapter we demonstrate that introducing local structural network heterogeneities changes the global temporal dynamics of neuronal networks. In network computational models, we observe stabilization of global network dynamics upon introduction of a local heterogeneity. Such stabilization could promote "system consolidation", creating a globally-distributed representation of the new memory. Critically, we find that optimal capacity for network-wide functional stability happens near excitatory/inhibitory (E/I) balance and at dynamical criticality, two features which characterize in vivo brain function[121]. Finally, we show that functional network stabilization is induced in the mouse hippocampus in vivo during formation of a fear memory engram. We conclude that certain features of brain function may have evolved to promote network-wide dynamic changes in response to novel learning, which in turn drives long-term memory consolidation.

It is widely hypothesized that new information is encoded in brain circuits through activity dependent, long-term structural changes. These structural changes modify the synaptic efficacy and functional connectivity between neuronal populations, a putative mechanism for storing a representation of information in memory (the engram)[122;123]. However, localizing engrams to specific neural circuits has been a historical conundrum. Attempts at physical disruption of established memories (e.g., through brain lesions[124] or, more recently, through optogenetic silencing[125;126]) have shown that engrams are robust to changes in communication between individual neurons, or even between brain areas. Thus, despite more than a century of study, it is not well understood how representations are formed and stored on larger scales, across neural circuits or the brain as a whole.

It is also unclear what impact these changes have on overall network dynamics. The generally long-accepted assumption is that the creation of additional connections (i.e., a network heterogeneity) leads to the formation of a dynamical attractor. Current work points to functional network reorganization upon memory formation[127].

However, the number of neurons participating in any computation (e.g., memory recall) is thought to constitute a small fraction of the total neuronal population. This raises a question: how is the brain able to detect structurally small attractors in order to recall their information?

Here, we show that formation of a discreet, local heterogeneity in neural network architecture (such as that associated with strengthening a subset of synapses in, or adding new synapses within, a neuronal network) has a significant impact on network dynamics, far beyond the heterogeneity itself. Namely, we find that formation of a local network heterogeneity stabilizes network dynamics far away from it.

5.2 Methods

5.2.1 Estimating stability

Determining the stability of functional connectivity: Functional connectivity metrics using Average Minimum Distance (AMD): Given a list of spike trains $S_1, S_2, , S_n$ for n neurons, where S_i contains all the firing times for neuron i, the functional relationship, FC_{ij}, of the i-th and j-th neurons is evaluated by comparing the average temporal closeness of spike trains S_i and S_j to the expected sampling distance of train S_j, μ_j. Values are normalized by dividing this difference by the expected variation in sampling distance of train S_j, σ_j.

The average distance from spike train S_i to S_j is given by the AMD_{ij}, where we define $AMD_{ij} = \frac{1}{N_i}\sum_k \Delta t_{ij}^k$, here N_i is the number of events in S_i and Δt_{ij}^k is the temporal distance between event k in S_i to the nearest event in S_j. The expected values, μ_j and σ_j, are calculated by integrating over the sampling minimum distance distribution of S_j. The expected mean sampling distance and standard deviation can be simply expressed by noting that over an individual interspike interval (ISI) of length L, the first two moments of minimal distance are given by $\mu^L =< MD^L >= \frac{L}{4}$

and $< (MD^L)^2 >= \frac{L^2}{12}$. Taking into account the probability of sampling an interval of length L for a spike train of length T is $\frac{L}{T}$, we can combine the values from intervals to give $\mu_j =< MD_j >= \sum_{\{L\}} p_L \mu^L = \frac{1}{T} \sum_{\{L\}} \frac{L^2}{4}$, and $< (MD_j)^2 >= \frac{1}{T} \sum_{\{L\}} \frac{L^3}{12}$. The expected standard deviation is given by $\sigma_j^2 =< (MD_j)^2 > - < MD_j >^2$. Knowing now how to evaluate all the components, we estimate the functional connectivity between neurons i and j as: $\widehat{FC}_{ij} = \sqrt{N_i} \frac{\mu_j - AMD_{ij}}{\sigma_j}$. The functional connectivity values represent the significance of the average temporal closeness of S_i to S_j after taking into account the spiking distributions of S_j. The calculations of μ_j and σ_j allow for rapid estimation of functional connectivity and are accurate approximations so long as the spike timings are well determined. Furthermore, the methods used here can be readily generalized to more complex measures, for instances a quadratic or exponential distance.

Functional stability as a measure of network dynamics: Functional connectivity networks can be calculated for multiple time segments and then compared using cosine similarity to get a measure of how functional relationships change over time. Cosine similarity, $C_{AB} = \cos\theta_{AB} = \frac{<A,B>}{\sqrt{<A,A><B,B>}}$, is a measure of the overlap between two values, with 1 denoting no change in the network and 0 indicating the two networks are not related. (See Fig. 5.3) When the similarity is found for a series of adjacent time windows, the average of these values denotes the average value of change which we refer to as functional stability. The length of the time bins is constrained at the low end by the spike counts of the analyzed neurons. We used the shortest time bins possible where each neuron contains at least 10 spikes, so that the functional connectivity values are based upon the full set of neurons. Longer time-windows will average out functional dynamics in favor of long term permanent structure.

Functional stability matrix as means to analyze evolving network representations: In section 5.3 we compare consecutive functional representations to

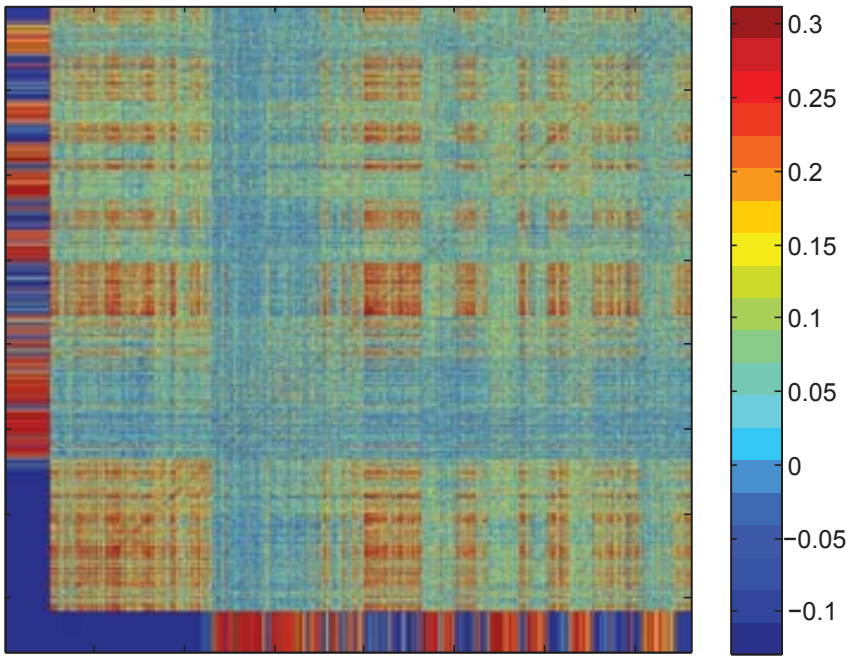

Figure 5.1: Example of AllxAll Stability - Example of a functional stability matrix. The stability is calculated for every pair of time-points in the 24 hr recording. The color in the body denotes stability magnitude (as indicated by the color bar on the side), while the color along the X and Y axes represents the behavioral state of the animal (blue wake, red SWS, yellow REM sleep, state mixtures are represented by color blends).

assess mean network stability. However, interesting information can be extracted through analysis of functional stability matrix (Fig. 5.1), where stability is not limited to adjacent time windows. Fig. 5.1 shows an example of the functional stability calculated across the 24hr recording. Formation of state (sleep vs. wake) dependent domains is clearly visible. In this particular example the similarity is significantly higher overall for waking behavior.

5.2.2 Simulations

Excitatory integrate-and-fire (LIF) network: A leaky IAF model was used to investigate stability in simulated data. Neuron voltages evolve according to the a

LIF model described by $\frac{dV_i}{dt} = -\alpha V_i + \sum_j A_{ij} C_{ij} S(t - t_j^k) + I_i(t) + N\delta(t_{m,i})$. Here the terms of the RHS denote leak current, summed synaptic input, constant external drive, and a noise term, respectively. The equations were integrated using Euler's method. V_i is the voltage of neuron i, and when it exceeds 1, the neuron fires and the voltage is reset to 0 after R_p=10 time steps refractory period. The leak constant is α= 0.5. C_{ij} is the adjacency matrix, where $C_{ij} = 1$ when there is a connection between neurons ij and C_{ij}=0 otherwise. The parameter A_{ij} denotes the strength of the connection between i-th and j-th neuron; A_{ij} is a random variable drawn from uniform distribution $A_{ij} \in [0, .1]$. $S(t - t_j^k)$ denotes the synaptic current sent from neuron j following it spiking at time t_j^k. The synaptic wave form we used was defined as the difference in two exponentials given by $S(t) = e^{\frac{-t}{\tau_s}} - e^{\frac{-t}{\tau_f}}$, where the τ_s= 3 and τ_f=0.3. Ii is the external drive delivered to cell i; each cells external drive was assigned prior to the simulation to allow for a range of natural firing rates. The last term on RHS represents noisy input to the neuron modeled by a variable amplitude (0.35-0.7) single time step of current pulse. The probability of a cell experiencing noise at any given time step was p_n=0.1.

The networks consisted of 1000 cells connected locally with a varying connectivity radius and then rewired with various rewiring probabilities. A heterogeneity was constructed by strengthening or adding more connections between connected cells within the heterogeneity. Each simulation was run for $T = 2 * 10^4$ time steps.

LIF networks with inhibition: The inhibitory simulations uses the same general form as the excitatory only networks, but additionally include 250 inhibitory cells. These cells form a sub-network that is positioned to be evenly distributed across the 1000 excitatory cells. Their radius of connectivity is the same as that of the excitatory cells, but their strength is 2.5 times the excitatory strengths. This value was computationally determined to be about the value at which excitation and inhibition balance for the homogeneous network. To change excitation/inhibition

balance (Fig. 5.5(a,b) in the network we applied additional external current IA received by inhibitory cells,$I_A \in [-0.1, 0.1]$. For these simulations we set the following parameters: R_p=20, p_n=0.025, and T=105.

Modified Bak-Tang-Wiesenfield model: A modified version of the Bak-Tang-Wiesenfield (BTW) model[128] was used as a simplified IAF model corresponding to a 3D network with N = 12x12x12 = 1728 cells. Each cell had a connectivity radius of r = 1 with non-periodic boundary conditions; connections were rewired with a probability of 0.1 to a small world network. The energy of each cell i is given by $E_i(t+1) = E_i(t) + \sum_{j=1}^{n} AC_{ij}E_j^*(t) + \delta(x-i)$ where the terms in the RHS correspond to the summation of the present value of the cells energy and all of its inputs. The summation term represents the total inputs from connected, spiking cells (E_j^*) multiplied by the corresponding connectivity strength A. The connectivity strength was uniform over the entire network except for a 5x5x5 cell sub-network placed starting at position (6,6,6) where A = 2.0, representing a region of heterogeneity.

Following the BTW model,a cell x is randomly chosen with probability $\frac{1}{N}$ to receive a unit of external input of energy using the delta function. Here, A is strictly positive thus causing E_i to increase in time until a threshold is met whereby it topples, sending information to its connected cells before resetting in the following time step, i.e.$E_i(t+1) = 0$,if $E_i(t) \geq 6$. Once a cell is reset by this mechanism, it enters a refractory time of 20 time steps during which it cannot send or receive information. Similarly, if at least one cell fired in the previous time step, then no external input is provided to the system, i.e. x = 0 and thus $\delta(x-i) = 0$.

Calculation of Avalanches and Power Law Distributions: Spike times from the modified BTW model were sorted in time in order to calculate neuronal avalanche sizes[129]. In this case, the avalanche size corresponds to the total number of consecutive spike times with time separations less than or equal to one time step (thus, multiple topplings occurring simultaneously are counted). Discrete probability

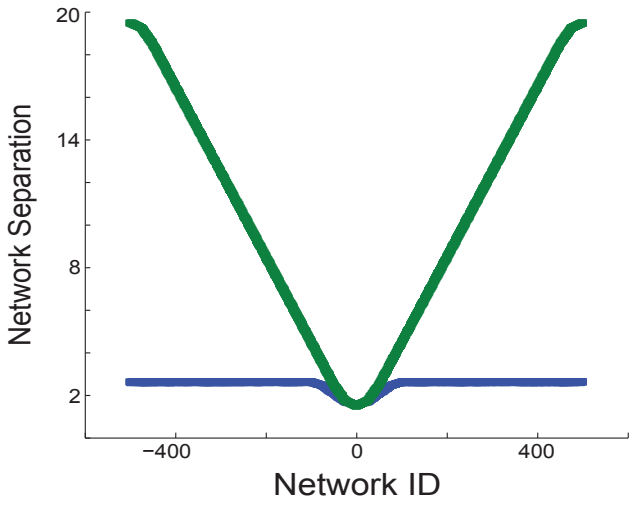

Figure 5.2: Euclidean distance versus neural separation - Example of the relationship between Euclidean distance and Network separation (i.e. average number of connections needed to cross to get from one point in the network to another) for two network connectivities. - The heterogeneity is centered at 0. Green line denotes local connectivity (p=0) in one dimensional network. Blue line denotes connectivity for rewiring probability p=0.1. Calculations were averaged over 16 network instances.

distributions were calculated from the histogram of avalanche sizes.

Neural separation versus Euclidean distance: definition of far distance: In our simulations the distance between the heterogeneity and any cell in the network is measured as an Euclidean distance assuming that the lattice constant is set to one. On Figures 5.4-5.6 cells far from heterogeneity are defined as the ones having maximal Euclidean distance from it. In the complex networks the distance or separation between two regions is more naturally defined as the separation in terms of number of connections needed to cross between them. Neural separation depends on network structure (Fig. 5.2). For local connectivity (a rewiring probability of p=0) the network distance increases linearly with Euclidean distance from the center of the heterogeneity, with slope dependent on the number of connections per neuron. For $p > 0$ the separation becomes essentially independent of Euclidean distance and scales approximately as ln(N), where N is network size[69].

5.2.3 Experimental procedure and data acquisition

Chronic in vivo recording and contextual fear conditioning: Male C57BL6 /J mice (Jackson, aged 2-5 months) were implanted with driveable headstages containing two bundles of 7 stereotrodes each (spaced 1 mm apart) for single-unit and local field potential (LFP), and silver-plated wires for nuchal electromyographic (EMG) recording. LFP and EMG signals were used to assign behavioral states (wake, SWS, REM sleep) in $5s$ epochs throughout the recording period. Mice were individually housed (in standard caging with beneficial environmental enrichment including nesting material, manipulanda, and treats) during post-operative recovery and subsequent behavioral experiments. Lights were maintained on a $12hr:12hr$ light:dark cycle, and food and water were available ad lib, throughout all procedures. All housing and experimental procedures were approved by the University Committee on Use and Care of Animals at the University of Michigan.

Following a 1-week recovery period, mice were habituated to daily handling (5-10 min/day) for 3 days. During this habituation period, stereotrodes were gradually lowered into CA1 until stable neuronal recordings (with characteristic spike waveforms continuously present on individual recording channels for more than $24hr$) were obtained. After this, no changes to electrode position were made throughout subsequent experimental procedures. All mice underwent a $24hr$ baseline recording starting at lights on. At lights on the following day, mice underwent single-trial contextual fear conditioning (CFC) or sham conditioning (Sham, $n = 4$)[57]. Mice were placed into a standard conditioning chamber (Med Associates) with patterned Plexiglass walls and a metal grid floor. All mice were allowed to freely explore the novel chamber over the $3min$ training session; CFC mice (but not sham mice) received a $2s$ footshock (0.75 mA) after the first $2.5min$. At the end of $3min$ in the conditioning chamber, mice were returned to their home cage for a $24hr$ post-conditioning recording period. CFC mice were subdivided into two groups - one which was allowed ad lib sleep (CFC,

$n = 5$), and a second which was sleep deprived by gentle handling for the first six hours following training[130] (a manipulation which is sufficient to disrupt contextual fear memory consolidation[131;132]; Sleep Dep, $n = 5$). $24hr$ following training, at lights on, mice were returned to the conditioning chamber for a $5min$ assessment of contextual fear memory. This was calculated as the change in context-specific freezing between testing and training trials (i.e., (% time spent freezing at test) − (% time spent freezing at baseline)[pre-shock]).

Spike data analysis: Electrophysiological signals were digitized and differentially filtered as spike and LFP data as described previously[57] using Omniplex hardware and software; single-unit spike data was discriminated using Offline Sorter software (Plexon). The firing of individual neurons was tracked throughout each experiment on the basis of spike waveform, relative spike amplitude on the two stereotrode recording channels, positioning of spike wave-form clusters in three-dimensional principal component space, and neuronal subclass (e.g., FS interneurons vs. principal neurons). Only those neurons that were reliably discriminated and continuously recorded across 24-hr baseline and 24-hr post-conditioning recording periods were included in analyses of network stability. A separate analysis of a subset of the spike data used in this study was published previously[57].

5.3 Results

We first quantified network stability to measure temporal dynamics in the functional network; the workings of our network stability metric are shown in Fig. 5.3. Briefly, neuronal spike times are divided into temporal bins (Fig. 5.3(a), of the shortest possible length to provide a robust estimate of functional connectivity. We used average mean distance (AMD)[133] to evaluate functional network connectivity in each bin. Functional stability is quantified as the cosine similarity, given by $S = \frac{\sum_{i,j} A_{ij} B_{ij}}{|A||B|}$, between functional networks at two different time points. This provides a normalized

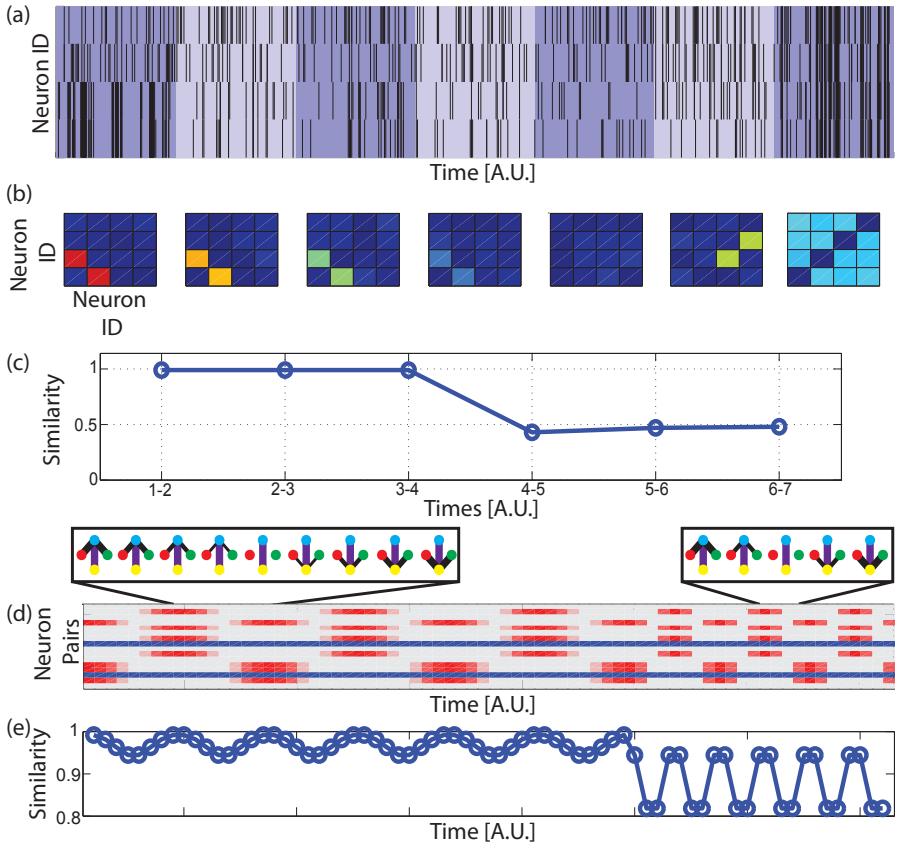

Figure 5.3: Visual example of functional network similarity - (a) An example firing raster for four neurons partitioned into seven time bins; (b) functional connectivity matrices, based on spike trains in each segment, estimated using the AMD metric. Color denotes connection strength; blue and red represent weak and strong connections, respectively; (c) cosine similarity of adjacent representations. (d and e) An example of functional stability for an oscillating network structure with varying periods. (d) Evolving functional connectivity of every cell pair in a simple 4-neuron network (insets individual neurons are represented by red, yellow, green and blue; excitatory connection is black, inhibitory connection is purple; line thickness represents connection strength). Blue and red denote low and high correlations, respectively, white represents correlation near zero. (e) Similarity values for the functional representations of (d) similarity captures the rate of change of the functional network.

measure of their overlap (Fig. 5.3(b). Functional network stability thus provides a measure of functional network changes over time (Fig. 5.3(c), with values closer to one representing stable (unchanging) networks. As an example, Fig. 5.3(c) depicts an artificially-generated functional network, which changes at a rate 2x slower at the beginning vs. end of the trace. Functional similarity drops precipitously as the rate of change increases.

5.3.1 Nonlocal detection of heterogeneities

We next applied the network stability metric to a simple integrate-and-fire network model composed of 1000 neurons described by $\frac{dV_i}{dt} = -\alpha V_i + \sum_j A_{ij} C_{ij} S(t - t_j^k) + I_i(t) + N\delta(t_{m,i})$; these terms denote leak current, summed synaptic input, constant external drive, and noise, respectively. The neurons are thus driven by internal and/or external input, and also receive random excitation at time $t_{m,i}$ (see supplemental material for details). Initially, we compared functional network stability between sparsely-connected excitatory-only networks having identical connectivity structure except for the inclusion of a localized heterogeneity (in which the coupling between 100 adjacent neurons increased; Fig. 5.4(a). Fig. 5.4(a,b) depicts changes in stability measured within the heterogeneity and away from it. Changes in functional stability were detected not only within the heterogeneity itself, but also far away from it (see definition of network distance in supplemental material). The strength of the heterogeneity modulated the resulting stability change, especially far from its location (Fig. 5.4(b) and Fig. 5.4(c), but significant changes were observed even for small heterogeneity sizes (relative to the whole network) and for moderate strengthening of connections.

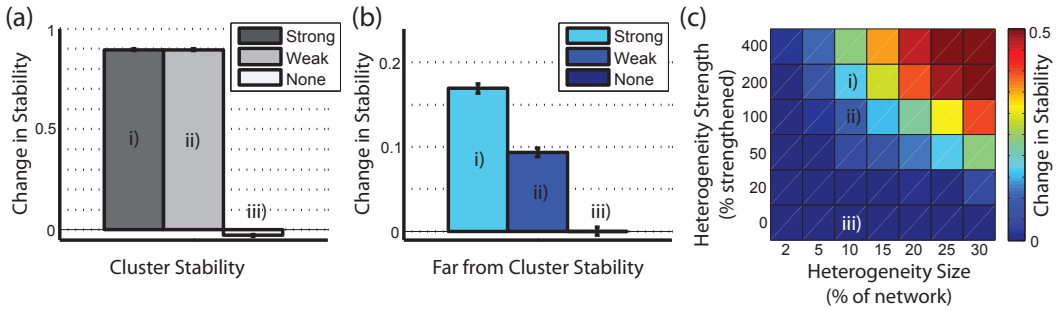

Figure 5.4: Comparison of functional stability within identical networks in the presence and absence of a localized heterogeneity - (a) The change in functional stability due introduction of heterogeneity, calculated for neurons positioned within that heterogeneity. Bars denote (from the left) strong, weak and no structural heterogeneity, respectively. (b) Same as panel (a), calculated for 100 neurons positioned far outside the heterogeneity. Roman numbering of the bars corresponds parametric positions in panel (c). (c) Change of functional stability as a function of heterogeneity size and strength calculated for representations of 100 neurons positioned at maximal distances from the heterogeneity. Here the network is composed of N=1000 excitatory integrate-and-fire neurons. The network is a 1D structure having local connectivity density of 5%. The neurons for which stability is calculated are an average Euclidean distance of $\sim$ 500 lattice units apart, which corresponds to an average network separation of a $\sim$2.7 number of connections (please see discussion in supplemental material and Fig S1).

5.3.2 Excitation balance and criticality

Since functional stability may depend on network properties, we investigated which dynamical network regimes promote global stabilization in response to localized heterogeneities. Excitatory/inhibitory (E/I) balance, calculated as the ratio of total network-wide inhibitory and excitatory effective inputs, is thought to emerge naturally in sparsely connected networks with strong synapses[134]. Neurons within networks working in this regime exhibit faster linear response to stimulation, and greater dynamic range[135]. To investigate how (E/I) balance affects network stability changes, we modified the integrate-and-fire network to a mix of inhibitory (N_i=250) and excitatory (N_e=1000) neurons, and varied the external drive to inhibitory neurons while keeping excitatory drive constant. Fig. 5.5 depicts stability (Fig. 5.5(a)) and change in stability (Fig. 5.5(b) as a function of inhibitory drive. The sensitivity of the latter measure to the presence of a heterogeneity peaks near the (E/I) balance (additional inhibitory drive = 0); large deviations in both directions reduce its sensitivity to zero.

We also assessed how self-organized criticality affects network stability. This feature of network dynamics is hypothesized to provide the brain with maximal computational agility, with emergence of long-range correlations at the critical point[136] allowing for rapid spread of information throughout the network. We found that this precise feature mediates maximal functional network stabilization far from a localized heterogeneity. Here, we used Bak's model[128] and measured the distribution of spike-time avalanche lengths in the system. As before, we compared changes in network stability in the presence and absence of a structural heterogeneity (125 adjacent neurons with increased connection strengths between them). To generate subcritical, critical, and supercritical networks, we altered the strength of the connections, homogeneously, in the rest of the network. Distributions of avalanche lengths, and sensitivity of functional stability, as a function of the connectivity strength are shown

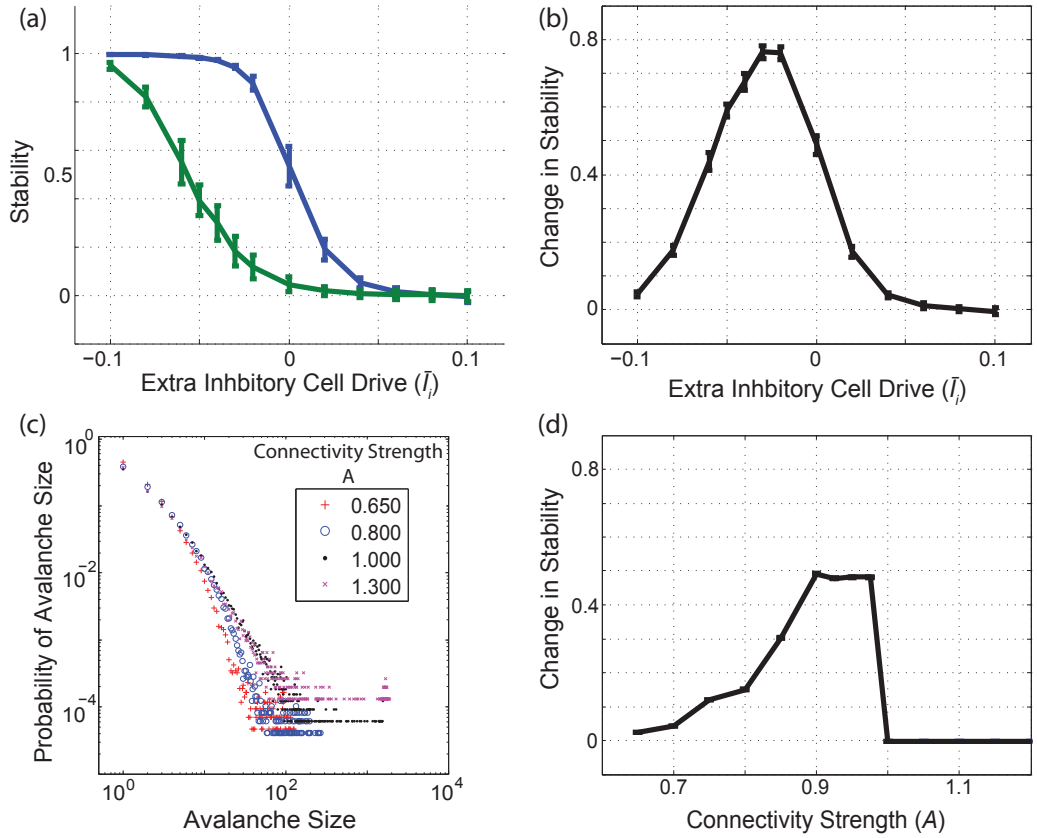

Figure 5.5: Identification of dynamical network regimes for optimal sensitivity of functional stability - (a , b) Inhibition/excitation balance. (c , d) Criticality. (a) Average stability of excitatory + inhibitory networks as a function of additional inhibitory drive. Two lines represent stability of the networks with and without structural heterogeneity blue and green line, respectively. 0 on the x-axis denotes the approximate region where excitation and inhibition balance. (b) Average change in stability (difference between blue and green line from panel (a) due to the presence of a structural heterogeneity, as a function of inhibitory drive. As above, zero denotes the point where excitation/inhibition 1. The optimal sensitivity of functional stability coincides with the excitation/inhibition balance. Simulations are averaged over 16 independent network realizations. (c) Distribution of avalanche sizes for the BTW criticality model for various coupling strengths in the presence of heterogeneity. The critical point (and power law distribution of avalanche sizes) is at A=1. (d) Average change in stability due to the presence of a structural heterogeneity, as a function of coupling strength. The maximal sensitivity of functional stability is just below the critical point. For critical and supercritical values the change in stability rapidly vanishes. Simulations are averaged over 16 independent network realizations. For detailed description of these simulations please consult supplementary material.

in Fig. 5.5(c,d). The highest sensitivity of functional network stability occurs just below the critical connectivity of 1.0. This identifies the optimal dynamical regime to be near, but just below, criticality, coincident with number of recent findings that in vivo brain dynamics operate in that regime[129].

5.3.3 Sensitivity of stability to structural network properties

We further investigated how the sensitivity of network stability depends on structural network properties. We varied drive, connectivity density, and rewiring probability[69] (where p=0 constitutes local, while p=1 random connectivity) in excitatory-only networks (Fig. 5.6). For all these parameters we observe rapid transition from low to high functional stability, with highest sensitivity to structural heterogeneity invariably occurring at the transition region of similarity.

5.3.4 *In Vivo* network signatures of learning

Finally, we applied the notion of functional stability to detect structural network reorganization associated with *de novo* memory formation following contextual fear conditioning (CFC). In this paradigm, a memory trace is rapidly and reliably generated after a single training trial. We used stereotrodes to stably record hippocampal CA1 activity from 10-30 neurons/mouse prior to, during, and following CFC training[57]. Following a 24-hr baseline recording period, mice were briefly moved to a novel cage in which they are either exposed to a foot shock (CFC) or not (sham). We measured changes to network stability during various behavioral states (i.e. waking and slow wave sleep (SWS) by analyzing the similarity of functional network representations minute-by-minute over the entire pre- and post-training intervals (Fig. 5.7). We observed an overall increase in SWS stability in CFC animals following training (Fig. 5.7(a), which was not seen following sham conditioning. This increase in stability was also blocked if mice were sleep deprived in the hours immediately following training

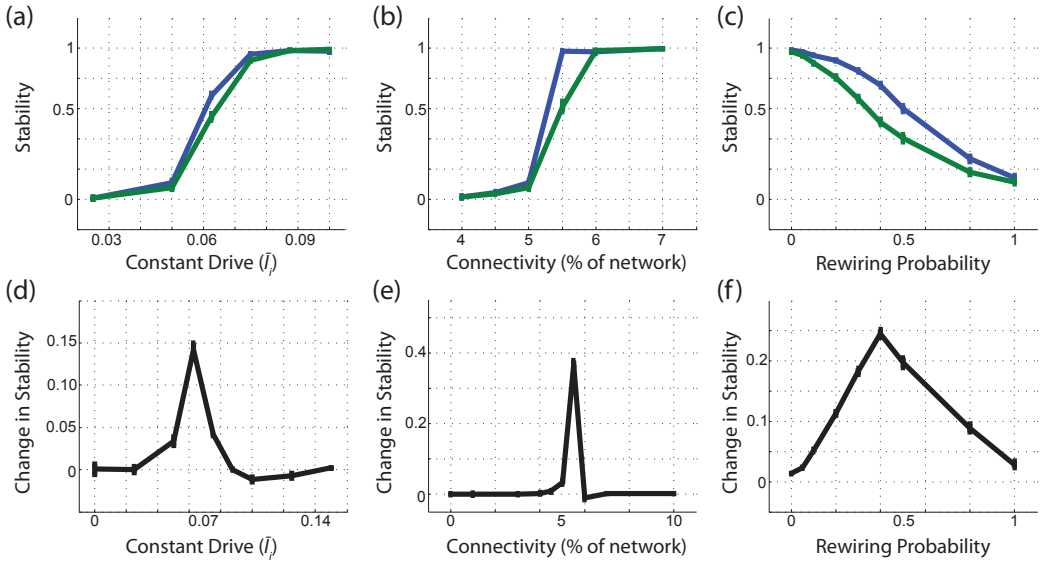

Figure 5.6: Changes in functional stability far from heterogeneity as a function of the networks' structural properties - Excitatory external drive (I), strength (a,d), excitatory connectivity radius (b,e), and rewiring probability, p, of excitatory connections (c,f). (a-c) Stability response to changes in the networks' structural properties; (green functional stability in absence of heterogeneity; blue in presence of heterogeneity) (d-f) Average change in functional stability (difference between blue and green line from panels (a-c), respectively) due to the presence of a structural heterogeneity as a function of network structural parameters. Simulations were performed for excitatory only networks of integrate-and-fire neurons (N=1000). For details please consult supplemental material.

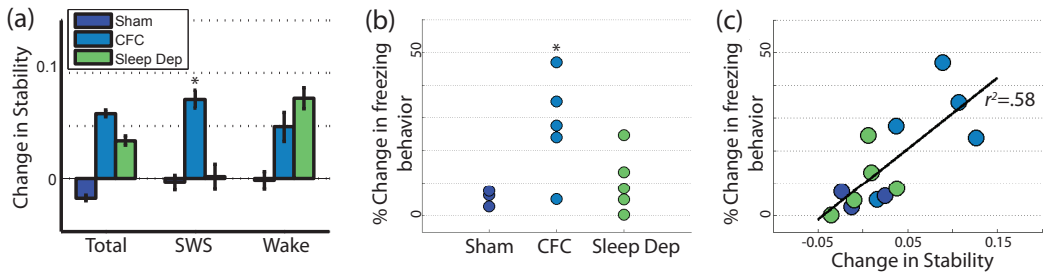

Figure 5.7: Experimentally observed changes in functional stability in mouse hippocampus during consolidation of contextual fear memory - (a) Average change in CA1 hippocampus stability (from 24-hr baseline) following Sham conditioning (novel environment context, no foot shock), CFC (contextual fear conditioning; novel environmental context + footshock), and Sleep Dep (novel environmental context + footshock, followed by 6-hr sleep deprivation). Values are averaged over the entire 24-hr post-training period, over SWS alone, and over wake alone. * indicates $p < 0.05$, Holm-Sidak post hoc test vs. Sham and Sleep Dep mice. (b) Behavioral measures of memory consolidation for mice in the three experimental groups. Observed % change in freezing behavior when mice are returned to the training environment. * indicates $p < 0.05$, Holm-Sidak post hoc test vs. Sham and Sleep Dep mice. (c) Post-training change in SWS functional stability vs. observed change in freezing behavior for each mouse. $p < 0.005$, Pearson correlation.

- a condition that impairs contextual fear memory consolidation[131;132]; Fig. 5.7(b). Remarkably, each mouse's memory consolidation index (i.e., contextual freezing behavior) was strongly proportional the change in functional network stability in CA1 after training (r^2=0.58, $p < 0.005$; Fig. 5.7(c)). Thus memory consolidation in vivo is accompanied by increased functional network stability in CA1, especially during SWS.

5.4 Discussion

Through network modeling and experimentation we show that functional network stability provides a global measure for identifying local network reorganization associated with the engram. Our modeling work shows that the highest sensitivity of functional stability changes to localized structural network changes happens for nearly

balanced excitation and inhibition and near criticality (Fig 5.5). We hypothesize that (E/I) balance provides the greatest sensitivity of network stability to heterogeneities by increasing neuronal dynamical range, and in turn expanding the network-wide transition region from near-zero to saturated stability (Fig 5.6). At the same time, network operation in a critical regime provides a means to both momentarily stabilize the network and create a globally-distributed engram. We thus propose a novel link between these dynamical regimes and memory consolidation. Our results hint at network mechanisms that neural networks may have evolved to promote systems consolidation - i.e., the formation of widely distributed engrams.

CHAPTER VI

Summary and conclusions

The neuron doctrine states that neurons are the building blocks of the brain, and modern theory suggests that synapses are responsible for storing information. Unfortunately, a high level understanding of the interactions dictated by synaptic connections remains a stumbling point in neuroscience. Both the scale and the structure of brain networks present challenges to advancement within the field. Given the rich complexity of the brain, it is not even clear what should be meant by understanding interactions in the brain. A theory encompassing all types of interactions may be possible some day, but smaller steps in that direction can help to define the landscape of such comprehensive theory. This dissertation uses two distinct approaches to address the problem of interactions in brain networks. First, astrocyte networks are classified by introducing a model that defines the structure of network interactions. The second approach defines a framework to handle the high dimensionality of interactions in neuron networks, and later probes the encoding of information in functional network structures.

Before investigating biological astrocyte networks, a basic two-process network is studied in Chapter II to learn how distinct excitation pathways interact under varying network topologies. Connections between cell bodies allows for direct signaling between selected cells, while extracellular diffusion influences all cells in close proximity.

Individually, each process aims to excite the network, but failure to work together limits the influence of activations. We show that local topologies overlap the range of interactions resulting in cooperative excitation of the network. Conversely, randomized topologies isolate the signaling pathways producing a competition between modes of excitation. Further, we found that the relative speed of the processes is essential to the interactions. In local networks the degree of cooperation monotonically decreases as diffusion speeds increase. However, nonlinear dependencies are also observed. For instance, mean phase coherence has a quadratic dependence on diffusion speed.

Chapter III applies this two process model to astrocyte networks to reproduce cultured astrocyte transients. Individual parameter regions can be selected where good agreement is shown for the influence of gap junction connectivity on the number of astrocyte transients, the strength of gap junction couplings, the average duration of transients, and the speed of signal propagation. Additionally, all of these regions overlap, offering a parameter range which biologically captures the key properties of gap junctions. Diffusion is also a necessary signal component in these regions, suggesting that gap junctions are dominant but not exclusive signal carriers of astrocytic information.

Moving away from astrocyte simulations, Chapter IV introduces a measure that can extract neuron functional connectivities from modern data recordings. Wide scale measurement of synapses remains difficult, which steers optimal large scale techniques away from tracking anatomical connectivity. Functional connectivity represents the activity patterns of neurons, which is precisely what synapses are able to control. This makes functional connectivity a strong alternative to anatomical connectivity to use as the basic unit in deciphering network interactions. We introduce average minimum distance and expected minimum distance on these distributions as components that together can be used to quickly assess functional connectivity from time series data. We also demonstrate the ability of AMD based functional connectivity

to identify functional relationships from noisy multichannel neurons. Functional connectivity is then used introduce the concept of network stability which compares high dimensional network representations. Stability simplifies quantification of network dynamics and makes it possible to study how information is functionally encoded in neuron networks.

Finally, in Chapter V the sensitivity of network stability is tested by measuring the formation of structural heterogeneities. This is done by comparing identified relationships before and after the addition of the heterogeneity. Conceptually, strengthening structural relationships between cells reduces the variability in firing behavior, making the network firing patterns less variable and hopefully therefore more stable. A stability increase is observed in simulations for measurements made from neurons located within the heterogeneity, and more surprisingly it is also measured from neurons located outside the heterogeneity. Measuring a heterogeneity from outside its physical location is a problem addressed via criticality. Criticality, defined in brain networks as the point where a spiking neuron is likely to cause one other neuron to spike, is believed to closely approximate the biological state of neurons in the brain. From a dynamical systems perspective, correlation lengths become infinitely large at a critical point, suggesting that locally stored information is globally accessible in brain networks. We found that stability most clearly identifies changes in network structure in parameter regimes located close to critical transitions. Lastly, this is tested in live mice to see if stability from spike times from a network of neurons reflects the extent of their learning. Amazingly, network stability agrees well with traditional measures of animal learning.

Collectively, this work suggests two vastly different approaches understanding interactions in brain networks. Astrocytes represent a layer of detail in most brain networks that is currently unaccounted for, and all attempts to include them necessarily increase the complexity of interactions. Quantifying network dynamics offers

a method to simplify views of network interactions down to single values. These approaches are not contradictory; rather they reflect the need for tailored approaches in modern neuroscience research. Excitingly, network dynamics makes it possible to probe the storage of information at the cellular and synaptic level, which offers hope that someday neuroscience will move beyond the neuron doctrine to understand the role of network interactions in the brain.

BIBLIOGRAPHY

BIBLIOGRAPHY

[1] F. López-Muñoz, J. Boya, and C. Alamo. Neuron theory, the cornerstone of neuroscience, on the centenary of the Nobel Prize award to Santiago Ramón y Cajal. *Brain Res. Bull.*, 70(4-6):391–405, Oct 2006.

[2] S. Finger. *Origins of neuroscience: A history of exploration into brain function.* Oxford University Press, 2001.

[3] E. Kandel, J. Schwartz, and M. Jessel. *Principles of neural science.* McGraw-Hill: New York, 200.

[4] A. Hodgkin and A. Huxley. A quantitative description of membrane current and its application to conduction and excitation in nerve. *J. Physiol. (Lond.)*, 117(4):500–44, Aug 1952.

[5] S. Bressler. Large-scale cortical networks and cognition. *Brain Res Rev*, 20(3):288–304, 1995.

[6] E. Kandel. *In search of memory: The emergence of a new science of mind.* Norton & Company, 2006.

[7] G. Buzsaki. *Rythms of the brain.* Oxford University Press, 2006.

[8] A. McIntosh. Towards a network theory of cognittion. *Neural Netw*, 13(8-9):861–70, 2000.

[9] R. Williams and K. Herrup. The control of neuron number. *Annu. Rev. Neurosci.*, 11:423–53, 1988.

[10] L. Elias. *Neuropsychology: Clinical and experimental foundations.* Boston: Pearson/Allyn & Bacon, 2006.

[11] B. Hefti. How many brain cells does the average person lose per day from the age of 30. http://www.madsci.org/posts/archives/2002-03/1016223301.Cb.r.html, 3 2002. Accessed: 2015-07-06.

[12] V. Mountcastle. Modality and topographic properties of single neurons of cat's somatic sensory cortex. *J. Neurophysiol.*, 20(4):408–34, Jul 1957.

[13] V. Mountcastle. *An organizing prinicple for cerebral funciton: The unit model and the distributed system.* MIT Press, 1978.

[14] J. Elman. *Rethinking innateness: A connectionist perspective on development (neural netowrk modeling and connectionism).* A Bradford Book, 1996.

[15] K. Hornik, M. Stinchcombe, and H. White. Multilayer feedforward networks are universal approximators. *Neural networks*, 2(5):359, 1989.

[16] J. McClelland. The organization of memory. A parallel distributed processing perspective. *Rev. Neurol. (Paris)*, 150(8-9):570–9, 1994.

[17] P. Smolensky. Chapter 6: Information processing in dynamical systems: Foundations of harmony theory. In D. Rumelhart and J. McLelland, editors, *Parralel distributed processing: Explorations in the microstructure of cognition, volume 1: Foundations*, pages 194–281. MIT Press, 1986.

[18] J. Hopfield. Neural networks and physical systems with emergent collective computational abilities. *Proc. Natl. Acad. Sci. U.S.A.*, 79(8):2554–8, Apr 1982.

[19] G. Hinton. Learning multiple layers of representation. *Trends in Cognitive Sciences*, 11:428–434, 2007.

[20] Y. Bengio. Learning deep architectures for ai. *Foundations and Trends in Machine learning*, 2(1):1–127, 2009.

[21] L. Deng and D. Yu. *Deep learning: Methods and applications.* Microsoft Research, 2014.

[22] S. Zhong, Y. Liu, and Y. Liu. Bilinear deep learning for image classification. In *Proceedings of the 19th AMC International Conference on Multimedia*, pages 343–352, 2011.

[23] J. Gao, X. He, W. Yih, and L. Deng. Learning continuous phrase representations for translation modeling. In *Proc. ACL*, 2014.

[24] A. Burkitt. A review of the integrate-and-fire neuron model: I. Homogeneous synaptic input. *Biol Cybern*, 95(1):1–19, Jul 2006.

[25] G. Gershenson. A general methodology for designing self-organizing systems. *ArXiv*, 2005.

[26] F. Heylighen. Self-organization, emergence, and the architecture of complexity. In *Proceedings of the 1st European Conference on System Science, AFCET*, pages 23–32, 1989.

[27] F. Heylighen and D. Campbell. Selection of organization at the social level: Obstacles and facilitators of metasystem transitions. *World Futur. J. Gen. Evol.*, 45:181–212, 1995.

[28] D. Hebb. *The organization of behavior.* New York: Wiley and Song, 1949.

[29] G. Bi and M. Poo. Synaptic modifications in cultured hippocampal neurons: dependence on spike timing, synaptic strength, and postsynaptic cell type. *J. Neurosci.*, 18(24):10464–72, Dec 1998.

[30] T. Bliss and T. Lomo. Long-lasting potentiation of synaptic transmission in dentate area of anesthetized rabbit following the stimulation of perforant path. *Journal of Physiology-London*, 232:331–356, 1973.

[31] B Lendvai, E A Stern, B Chen, and K Svoboda. Experience-dependent plasticity of dendritic spines in the developing rat barrel cortex in vivo. *Nature*, 404(6780):876–81, Apr 2000.

[32] G. Lui. Local structural balance and functional interaction of excitatory and inhibitory synapses in hippocampal dendrities. *Nat Neurosci*, 7(4):373–379, 2004.

[33] E. Marder and V. Thirumalai. Cellular, synaptic, and network effects of neuromodulation. *Neural Netw*, 15(4-6):479–493, 2002.

[34] N. Masuda and K. Aihara. Global and local synchrony of coupled neurons in small-world networks. *Biol Cybern*, 90(4):302–9, Apr 2004.

[35] B. Pecora. Synchronization in small world systems. *Phys Rev lett*, 89(5):054101, 2002.

[36] A. Roxin, H. Riecke, and S. Solla. Self-sustained activity in a small-world network of excitable neurons. *Phys Rev Lett*, 92(19):198101, 2004.

[37] F. Azevedo *et al.* Equal numbers of neuronal and nonneuronal cells make the human brain an isometrically scaled-up primate brain. *J. Comp. Neurol.*, 513(5):532–41, Apr 2009.

[38] N. Swaminathan. Glia - the other brain cells. *Discover*, Jan-Feb 2011.

[39] T. Fellin. Communication between neurons and astrocytes: relevance to the modulation of synaptic and network activity. *J. Neurochem.*, 108(3):533–44, Feb 2009.

[40] B. Stevens. Glia: much more than the neuron's side-kick. *Curr. Biol.*, 13(12):R469–72, Jun 2003.

[41] S. Feldt *et al.* Functional clustering in hippocampal cultures: relating network structure and dynamics. *Phys Biol*, 7(4):046004, 2010.

[42] A. Araque, V. Parpura, R. Sanzgiri, and P. Haydon. Tripartite synapses: glia, the unacknowledged partner. *Trends Neurosci.*, 22(5):208–15, May 1999.

[43] M. Halassa, T. Fellin, and P. Haydon. The tripartite synapse: roles for gliotransmission in health and disease. *Trends Mol Med*, 13(2):54–63, Feb 2007.

[44] P. Bezzi and A. Volterra. A neuron-glia signalling network in the active brain. *Curr. Opin. Neurobiol.*, 11(3):387–94, Jun 2001.

[45] C. Agulhon *et al.* What is the role of astrocyte calcium in neurophysiology? *Neuron*, 59(6):932–46, Sep 2008.

[46] R. Basheer, R. Strecker, M. Thakkar, and R. McCarley. Adenosine and sleep-wake regulation. *Prog. Neurobiol.*, 73:379–396, 2004.

[47] Z. Huang, Z. Zhang, and W. Qu. Roles of adenosine and its receptors in sleep-wake regulation. *Int. Rev. Neurobiol.*, 119:349–71, 2014.

[48] P. Jourdain *et al.* Glutamate exocytosis from astrocytes controls synaptic strength. *Nat. Neurosci.*, 10(3):331–9, Mar 2007.

[49] T. Sasaki, N. Kuga, S. Namiki, N. Matsuki, and Y. Ikegaya. Locally synchronized astrocytes. *Cereb. Cortex*, 21(8):1889–900, Aug 2011.

[50] T. Porkka-Heiskanen *et al.* Adenosine: A mediator of the sleep-inducing effects of prolonged wakefulness. *Science*, 276:1265–1268, 1997.

[51] D. Postnov, R. Koreshkov, N. Brazhe, A. Brazhe, and O. Sosnovtseva. Dynamical patterns of calcium signaling in a functional model of neuron-astrocyte networks. *J Biol Phys*, 35(4):425–45, Oct 2009.

[52] S.i Koizumi. Synchronization of Ca2+ oscillations: involvement of ATP release in astrocytes. *FEBS J.*, 277(2):286–92, Jan 2010.

[53] D Wagenaar, J. Pine, and M. Potter. An extremely rich repetoire of bursting patterns during the development of cortical cultures. *BMC Neurosci*, 7(1):1–11, 2006.

[54] E. Bullmore and O. Sporns. Complex brain networks: Graph theoretical analysis of stuctural and functional systems. *Nat Rev Neuroscience*, 10(3):186–198, 2009.

[55] D. Marr. A theory for cerebral neocortex. *Proceedings of the Royal Society of London B*, 176:161–234, 1970.

[56] D. Marr. Simple memory: A theory for archicortex. *Philisophical Transactions of the Royal Society of London B*, 262:23–81, 1971.

[57] N. Ognjanovski, D. Maruyama, N. Lashner, M. Zochowski, and S. Aton. CA1 hippocampal network activity changes during sleep-dependent memory consolidation. *Front Syst Neurosci*, 8:61, 2014.

[58] D. Maruyama and M. Zochowski. Competition and cooperation between active intra-network and passive extra-network transport processes. *Sci Rep*, 4:5269, 2014.

[59] E. Shtrahman, D. Maruyama, E. Olariu, C. Fink, and M. Zochowski. Spatial and temporal patterning of astrocyte calcium transients explained by network transport and extracellular diffusion in a simple network model. *Submitted for publication*, 2015.

[60] D. Maruyama, N. Ognjanovski, Q. Skilling, S. Aton, and M. Zochowski. Learning-induced functional network stability as a mechanism for systems memory consolidation. *Submitted for publication*, 2015.

[61] M. Newman. The structure and function of complex networks. *SIAM Review*, 45(2):167–256, 2003.

[62] M. Newman. Communities, modules, and large-scale structure in networks. *Nature Physics*, 8(1):25–31, 2011.

[63] R. Albert and A. Barabási. Statistical mechanics of complex networks. *Reviews of Modern Physics*, 74(47), 2002.

[64] M. Bartholemy. Spatial networks. *Phys. Rep.*, 499:1–101, 2011.

[65] G. Zipf. *Human behaviour and the principle of least effort.* Addison-Wesley, Cambridge, MA, 1949.

[66] G. Li *et al.* Towards design principles for optimal transport networks. *Phys. Rev. Lett.*, 104(1):018701, Jan 2010.

[67] G. Ghoshal, L. Sander, and I. Sokolov. SIS epidemics with household structure: the self-consistent field method. *Math Biosci*, 190(1):71–85, Jul 2004.

[68] A. Burkitt. A review of the integrate-and-fire neuron model: II. Inhomogeneous synaptic input and network properties. *Biol Cybern*, 95(2):97–112, Aug 2006.

[69] D. Watts and S. Strogatz. Collective dynamics of 'small-world' networks. *Nature*, 393(6684):440–2, Jun 1998.

[70] M. Guye, G. Bettus, F. Bartolomei, and P. Cozzone. Graph theoretical analysis of structural and functional connectivity MRI in normal and pathological brain networks. *MAGMA*, 23(5-6):409–21, Dec 2010.

[71] F. Mormann, K. Lehnertz, P. David, and C. Elger. Mean phase coherence as a masure for phase synchronization and its application to the eeg of epilepsy patients. *Physica D*, 144:358–369, 2000.

[72] G. Dupont and A. Goldbeter. One-pool model for Ca2+ oscillations involving Ca2+ and inositol 1,4,5-trisphosphate as co-agonists for Ca2+ release. *Cell Calcium*, 14(4):311–22, Apr 1993.

[73] W. Gibson, L. Farnell, and M. Bennett. A quantitative model of atp-mediated calcium wave propagation in astrocyte networks. In A. Deutsch *et al.*, editor, *Mathematical Modeling of Biological Systems, Volume II*, Modeling and Simulation in Science, Engineering and Technology, pages 193–204. Birkhuser Boston, 2008.

[74] V. Torre. Synchronization of non-linear biochemical oscillators coupled by diffusion. *Biol Cybern*, 17(3):137–44, 1975.

[75] D. Bin, W. Jiang, and F. Xiangyang. Chaotic synchronization with gap junction of multi-neurons in external electrical stimulation. *Chaos Soliton. Fract.*, 25:1185–1192, 2005.

[76] W. Jiang, F. Dengbin, and D. Xiangyang. Chaotic synchronization of multineurons in external electrical stimulation. *Conf Proc IEEE Eng Med Biol Soc*, 2:2103–6, 2005.

[77] Y.i Sasai. Cytosystems dynamics in self-organization of tissue architecture. *Nature*, 493(7432):318–26, Jan 2013.

[78] H. Westerhoff *et al.* Macromolecular networks and intelligence in microorganisms. *Front Microbiol*, 5:379, 2014.

[79] E. Newman and K. Zahs. Calcium waves in retinal glial cells. *Science*, 275(5301):844–847, 1997.

[80] Y. Takayama, H. Moriguchi, K. Kotani, and Y. Jimbo. Spontaneous calcium transients in cultured cortical networks during development. *IEEE Trans Biomed Eng*, 56(12):2949–56, Dec 2009.

[81] S. Duffy and B. MacVicar. Adrenergic calcium signaling in astrocyte networks within the hippocampal slice. *J. Neurosci.*, 15(8):5535–50, Aug 1995.

[82] B. Haas *et al.* Activity-dependent ATP-waves in the mouse neocortex are independent from astrocytic calcium waves. *Cereb. Cortex*, 16(2):237–46, Feb 2006.

[83] B. Innocenti, V. Parpura, and P. Haydon. Imaging extracellular waves of glutamate during calcium signaling in cultured astrocytes. *J. Neurosci.*, 20(5):1800–8, Mar 2000.

[84] A. Cornell-Bell, S. Finkbeiner, M. Cooper, and S. Smith. Glutamate induces calcium waves in cultured astrocytes: Long-range glial signaling. *Science*, 247(4941):470–3, Jan 1990.

[85] C. Henneberger, T. Papouin, S. Oliet, and D. Rusakov. Long-term potentiation depends on release of D-serine from astrocytes. *Nature*, 463(7278):232–6, Jan 2010.

[86] C. Giaume. Astroglial wiring is adding complexity to neuroglial networking. *Front Neuroenergetics*, 2, 2010.

[87] P. Haydon. GLIA: listening and talking to the synapse. *Nat. Rev. Neurosci.*, 2(3):185–93, Mar 2001.

[88] C. Hales, J. Rolston, and S. Potter. How to culture, record and stimulate neuronal networks on micro-electrode arrays (MEAs). *J Vis Exp*, (39), 2010.

[89] A. Nimmerjahn, F. Kirchhoff, J. Kerr, and F. Helmchen. Sulforhodamine 101 as a specific marker of astroglia in the neocortex in vivo. *Nat. Methods*, 1(1):31–7, Oct 2004.

[90] E. Blanc, A. Bruce-Keller, and M. Mattson. Astrocytic gap junctional communication decreases neuronal vulnerability to oxidative stress-induced disruption of Ca2+ homeostasis and cell death. *J. Neurochem.*, 70(3):958–70, Mar 1998.

[91] S. Feldt Muldoon, I. Soltesz, and R. Cossart. Spatially clustered neuronal assemblies comprise the microstructure of synchrony in chronically epileptic networks. *Proc. Natl. Acad. Sci. U.S.A.*, 110(9):3567–72, Feb 2013.

[92] H. Köller, M. Siebler, C. Schmalenbach, and H. Müller. GABA and glutamate receptor development of cultured neurons from rat hippocampus, septal region, and neocortex. *Synapse*, 5(1):59–64, 1990.

[93] S. Del Cerro, J. Garcia-Estrada, and L. Garcia-Segura. Neuroactive steroids regulate astroglia morphology in hippocampal cultures from adult rats. *Glia*, 14(1):65–71, May 1995.

[94] G. Wallach *et al.* Glutamate mediated astrocytic filtering of neuronal activity. *PLoS Comput. Biol.*, 10(12):e1003964, Dec 2014.

[95] T. Sasaki *et al.* Astrocyte calcium signalling orchestrates neuronal synchronization in organotypic hippocampal slices. *J. Physiol. (Lond.)*, 592(Pt 13):2771–83, Jul 2014.

[96] G. Tian *et al.* An astrocytic basis of epilepsy. *Nat. Med.*, 11(9):973–81, Sep 2005.

[97] A. Tashiro, J. Goldberg, and R. Yuste. Calcium oscillations in neocortical astrocytes under epileptiform conditions. *J. Neurobiol.*, 50(1):45–55, Jan 2002.

[98] J. Rodríguez-Arellano, V. Parpura, R. Zorec, and A. Verkhratsky. Astrocytes in physiological aging and Alzheimer's disease. *Neuroscience*, Jan 2015.

[99] M. Xia, S. Abazyan, Y. Jouroukhin, and M. Pletnikov. Behavioral sequelae of astrocyte dysfunction: focus on animal models of schizophrenia. *Schizophr. Res.*, Nov 2014.

[100] T. Bliss, G. Collingridgem, and R. Morris. *LTP: Long-Term Potentiation.* Oxford University Press, 2003.

[101] A. Krizhevsky, I. Sutskever, and G. Hinton. Imagenet classification with deep convolutional neural networks. *Advances in neural information processing systems*, pages 1097–1105, 2012.

[102] P. Sermanet *et al.* Overfeat: Integrated recognition, localization, and detection using convolutional networks. In *International COnference on Learning Representations*, 2014.

[103] S. Grant *et al.* Impaired long-term potentiation, spatial learning, and hippocampal development in fyn mutant mice. *Science*, 258(5090):1903–10, Dec 1992.

[104] J. Hawkins and S. Blaksee. *On intelligence.* Henry Holt and Company, 2004.

[105] J. Whitson, D. Kubota, K. Shimono, Y. Jia, and M. Taketani. Mulitelectrode arrays: Enhancing traditional methods and enabling network physiology. In M. Baudry and M. Taketani, editors, *Advances in network electrophysiology using multi-electrode arrays.*, Modeling and Simulation in Science, Engineering and Technology, pages 38–68. New York: Springer Press, 2006.

[106] E. Salinas and T. Sejnowski. Correlated neuronal activity and the flow of neural information. *Nat. Rev. Neurosci.*, 2(8):539–50, Aug 2001.

[107] H. Fujisaka and T. Yamada. Stability theory of synchronized motion in coupled-oscillator systems. *Progr Theoret Phys*, 69:32–47, 1983.

[108] V. Afraimovich, N. Verichev, and M. Rabinovich. Stochastic synchronization of oscillation in dissipative systems. *Radiophys. Quantum Electron*, 29:795–803, 1986.

[109] Y. Kuramoto. *Chemical oscillations, waves, and turbulence.* Berlin: Springer, 1984.

[110] M. Rosenblum, A. Pikovsky, and J. Kurths. Phase synchronization of chaotic oscillators. *Phys Rev Lett*, 76:1804–1807, 1996.

[111] C. Granger. Investigating causal relations by econometric models and crossspectral methods. *Econometrica*, 37:424–438, 1969.

[112] M. Barlet. On the theoretical specification and sampling properties of autocorrelated time series. *J Roy Stat Soc B*, 8:27–41, 1946.

[113] S. Feldt, J. Wang, V. Hetrick, J. Berke, and M. Zochowski. Memory formation: from network structure to neural dynamics. *Philos Trans A Math Phys Eng Sci*, 368(1918):2251–67, May 2010.

[114] N. Metropolis and S. Ulam. The monte carlo method. *Journal of the American Statistical Association*, 44(247):335–341, 1953.

[115] P. Del Moral. Mean field simulation for Monte Carlo integration. In *Monographs on statistics and applied probability.*, page 626. Chapman and Hall/CRC Press, 2013.

[116] T. Trappenberg. *Fundamentals of computational neuroscience*. Oxford University Press, 2010.

[117] A. Singhal. Modern infromation retrieval: A brief overview. *Bulletin of IEEE Computer Society Technical Committee on Data Engineering*, 24(4):35–42, 2001.

[118] D. Feldman. The spike-timing dependence of plasticity. *Neuron*, 75(4):556–71, Aug 2012.

[119] E. Adrian and Y. Zotterman. The impulses produced by sensory nerve-endings: Part II. The response of a Single End-Organ. *J. Physiol. (Lond.)*, 61(2):151–71, Apr 1926.

[120] N. Tronson *et al.* Segregated populations of hippocampal principal CA1 neurons mediating conditioning and extinction of contextual fear. *J. Neurosci.*, 29(11):3387–94, Mar 2009.

[121] D. Chiavlo. Emergent complex neural dynamics. *Nature Physics*, 6:644–750, 2010.

[122] M. Hübener and T. Bonhoeffer. Searching for engrams. *Neuron*, 67(3):363–71, Aug 2010.

[123] E. Baeg *et al.* Learning-induced enduring changes in functional connectivity among prefrontal cortical neurons. *J. Neurosci.*, 27(4):909–18, Jan 2007.

[124] K. Lashley. Physiological mechanisms in animal behavior. In *Society's Symposium IV*, pages 454–482. Academic Press, Socitey for Experiemental Biology, 1950.

[125] K. Cowansage *et al.* Direct reactivation of a coherent neocortical memory of context. *Neuron*, 84(2):432–41, Oct 2014.

[126] I. Goshen *et al.* Dynamics of retrieval strategies for remote memories. *Cell*, 147(3):678–89, Oct 2011.

[127] D. Bassett *et al.* Dynamic reconfiguration of human brain networks during learning. *Proc. Natl. Acad. Sci. U.S.A.*, 108(18):7641–6, May 2011.

[128] P. Bak, C. Tang, and Wiesenfeld K. Self-organized criticality: An explanation of the 1/f noise. *Phys Rev Lett.*, 59(4):381–384, 1987.

[129] V. Priesemann *et al.* Spike avalanches in vivo suggest a driven, slightly subcritical brain state. *Front Syst Neurosci*, 8:108, 2014.

[130] S. Aton, A. Suresh, C. Broussard, and M. Frank. Sleep promotes cortical response potentiation following visual experience. *Sleep*, 37(7):1163–70, Jul 2014.

[131] L. Graves, E. Heller, A. Pack, and T. Abel. Sleep deprivation selectively impairs memory consolidation for contextual fear conditioning. *Learn. Mem.*, 10(3):168–76, 2003.

[132] T. Prince *et al.* Sleep deprivation during a specific 3-hour time window post-training impairs hippocampal synaptic plasticity and memory. *Neurobiol Learn Mem*, 109:122–30, Mar 2014.

[133] S. Feldt, J. Waddell, V. Hetrick, J. Berke, and M. Zochowski. Functional clustering algorithm for the analysis of dynamic network data. *Phys Rev E Stat Nonlin Soft Matter Phys*, 79(5 Pt 2):056104, May 2009.

[134] C. van Vreeswijk and H. Sompolinsky. Chaos in neuronal networks with balanced excitatory and inhibitory activity. *Science*, 274(5293):1724–6, Dec 1996.

[135] B. Liu *et al.* Broad inhibition sharpens orientation selectivity by expanding input dynamic range in mouse simple cells. *Neuron*, 71(3):542–54, Aug 2011.

[136] T. Boonstra, B. He, and A. Daffertshofer. Scale-free dynamics and critical phenomena in cortical activity. *Front Physiol*, 4:79, 2013.